

**Coupled-resonator-based metamaterials
emulating quantum systems**

Toshihiro Nakanishi

2015

Contents

1	Introduction	1
1.1	Background	1
1.1.1	Metamaterials	1
1.1.2	Typical examples and unique characteristics of metamaterials	2
1.1.3	Transmission-line metamaterials	6
1.1.4	Coupled-resonator-based metamaterials	8
1.1.5	Classical model for quantum phenomena	10
1.2	Outline of this thesis	11
2	Simulation of closed quantum systems	15
2.1	Isolated quantum system	15
2.2	Two-level system	17
2.2.1	Inductor-coupled resonator	18
2.2.2	Gyrator-coupled resonator	21
2.3	Circuit model of the Schrödinger equation	23
2.4	Simulation of the Schrödinger equation	27
2.4.1	Procedures	27
2.4.2	Free propagation	28
2.4.3	Tunneling problem	30
2.5	Circuit model of the Schrödinger equation in a vector potential . . .	32
2.5.1	Discretization of the Schrödinger equation in a vector potential	32
2.5.2	Circuit model for the Schrödinger equation in a vector potential	34
2.5.3	Aharonov–Bohm effect	35
2.6	Discussions	37

3	Circuit simulation of superluminal light for baseband signal	39
3.1	Pulse propagation in dispersive media	40
3.2	Realization of anomalous dispersion for superluminal propagation .	42
3.3	Negative group delay	44
3.3.1	Group delay	45
3.3.2	Superluminal propagation and negative delay	47
3.4	Circuits and experiment	47
3.4.1	Negative delay circuit for baseband signals	47
3.4.2	Low-pass filter	49
3.4.3	Experiment	50
3.5	Realization of larger negative delay	52
3.6	Summary and discussion	55
4	Circuit simulation of slowing and storing light for baseband signal	57
4.1	Slowing or storing light in atomic system	57
4.1.1	Control of group velocity with electromagnetically induced transparency	57
4.1.2	EIT condition	60
4.1.3	Change in spectral or spatial profile	61
4.2	Circuit model	62
4.2.1	All-pass filter	62
4.2.2	Spectrum conditions	63
4.3	Experiment	64
4.3.1	Circuit parameters and input signal	64
4.3.2	Constant speed propagation	65
4.3.3	Pulse length compression	65
4.3.4	Pulse storage	68
4.4	Summary	70
5	Artificial atoms interacting with electromagnetic fields	73
5.1	Classical model of two-level system interacting with external fields .	73
5.1.1	Linear response of two-level atoms	73

5.1.2	Circuit analogy of two-level system interacting with external fields	76
5.1.3	Metamaterial analogy of two-level system	78
5.2	Classical model of EIT	79
5.2.1	EIT effect with three-level atoms	79
5.2.2	Circuit analogy of EIT effects	81
5.2.3	Metamaterial analogy of EIT effects	84
6	Storage of electromagnetic waves in metamaterial	87
6.1	Tunable EIT metamaterial	88
6.1.1	Structure and operating principle	88
6.1.2	Circuit model	89
6.2	Simulation of transmission spectra	91
6.3	Experimental demonstration	92
6.3.1	Fabrication of metamaterial and experimental setup	93
6.3.2	Semi-static characteristics	95
6.3.3	Dynamic modulation of EIT property	97
6.3.4	Storage of EM waves	99
6.3.5	Discussions	103
7	Nonlinearity enhancement using doubly resonant metamaterial	105
7.1	Structure and circuit model	106
7.1.1	Singly resonant metamaterial	106
7.1.2	Doubly resonant metamaterial	108
7.2	Quantum-system interpretation	109
7.3	Linear response	113
7.4	Enhancement of second harmonic generation	114
7.5	Summary and discussion	117
8	Summary and discussion	119
8.1	Summary	119
8.2	Discussion and future works	120

A	Spice simulation for circuit models for Schrödinger equation	123
B	Polarization in a linear dispersive medium	127

Chapter 1

Introduction

1.1 Background

In this section, we introduce concept of metamaterial with its definition and review typical examples and unique characteristics of metamaterials.

1.1.1 Metamaterials

Electromagnetic (EM) properties of a medium, such as reflection, refraction, and propagation velocities, are determined by medium parameters, which include permittivity ε and permeability μ . The medium parameters can be defined for the medium composed of homogeneously distributed atoms or molecules, whose dimensions are much smaller than the wavelength of the EM waves as shown in Fig. 1.1(a). The permittivity and permeability are determined by distributions of electric charges and motions of the charges, or electric currents.* Thus, the medium parameters can be also defined for an assembly of sub-wavelength artificial structures, in which the charge and current distributions are formed by the incidence of EM waves as shown in Fig. 1.1(b). The assembly of the artificial structures, usually made of metal or dielectric, is called “*metamaterial*” and the single element

*Strictly speaking, spins, which determine permeability, are not the motions of charges, but they can be regarded as loop currents induced by self-rotating charged particles.

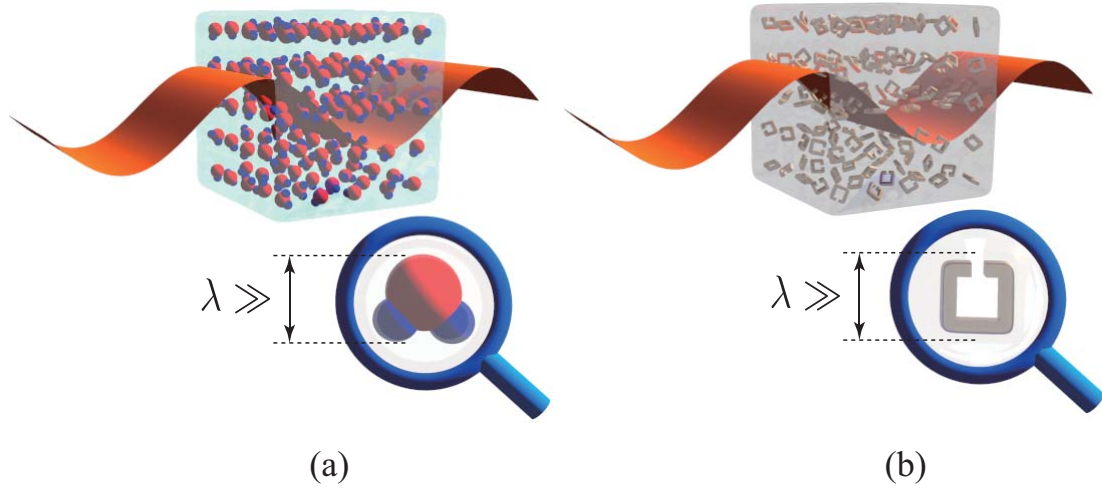


Figure 1.1: (a) Natural medium and (b) metamaterial interacting with EM waves.

of the metamaterial is often referred to as a “*meta-atom*.”[†]

1.1.2 Typical examples and unique characteristics of metamaterials

The metamaterials enable us not only to mimic various EM effects in natural media, but also to realize extraordinary EM phenomena that are not found in naturally occurring media. Here, we introduce some examples and extraordinary characteristics of metamaterials with earlier and recent works.

Control of permittivity, permeability, and chirality

Natural material shows a variety of relative permittivity ϵ_r from negative values to positive values. For example, some ceramics have large positive ϵ_r , and metal shows negative ϵ_r below its plasma frequency. It is also possible to tailor ϵ_r by designing artificial structures. A typical example of the artificial dielectric media is a metamaterial composed of metal wires, whose density controls the permittivity because the plasma frequency depends on the density of conductive carriers [1].

[†]However, metamaterial is often used to represent the constituents, or meta-atoms.

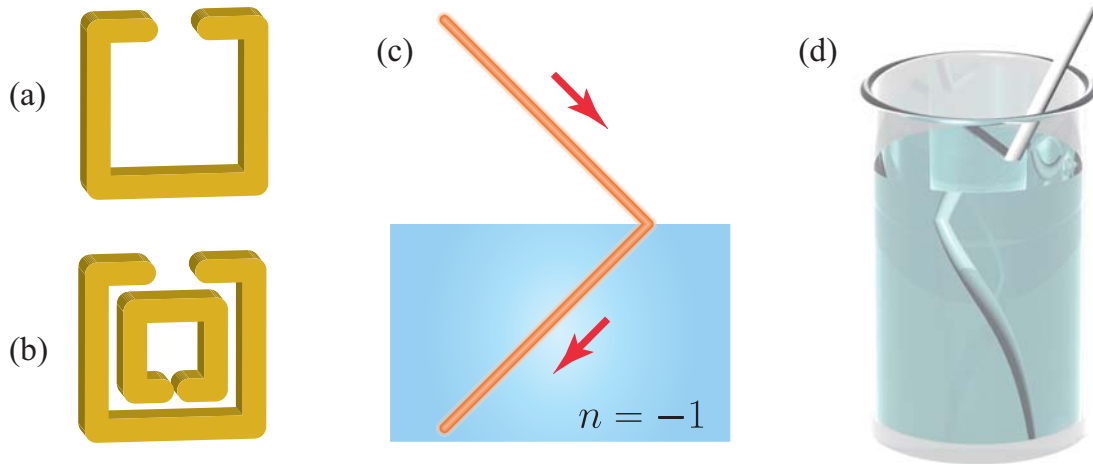


Figure 1.2: (a)(b) Magnetic metamaterials. (c) Negative refractive metamaterial. (d) Ray-tracing image of a straw in a medium with $n = -1$.

Compared to the electric response, magnetic response of natural material is significantly small especially in high frequency regions, and many textbooks on optics assume the relative permeability μ_r to be unity. It is generally known that the permeability of natural material is smaller than the permittivity by the factor of $|\alpha|^2$, where $\alpha \sim 137$ is a fundamental physical constant called fine-structure constant [2]. Some researches have proposed ways to realize high magnetic response with suppressing the effects of stronger electric response using atomic media with extremely high density [2–4], but experimental demonstration is quite difficult. In contrast, magnetic media with $\mu_r \neq 1$ can be easily obtained using metamaterials made of metals [5] or dielectrics [6, 7]. Figure 1.2(a) and (b) show typical metallic structures called split ring resonators (SRRs) with strong magnetic response in wide frequency range.[‡] In this structure, loop current along the ring is induced by the incidence of EM fields with the magnetic field threading the ring, and creates magnetic dipole moment, which is responsible for the magnetic response.

[‡]The SRR shown in Fig. 1.2(a) also have electric response, while the SRR shown in Fig. 1.2(b) does not have electric response [8].

It is also possible to realize metamaterial with chirality, which exhibits circular birefringence and circular dichroism, by employing artificial structure with broken mirror symmetry [9, 10].

After the development of the metamaterials, the freedom of medium parameters we can explore have been further extended. For examples, the magnetic metamaterial with $\mu_r \neq 1$ allows us to observe Brewster's effect for transverse-electric EM waves, which does not exist in natural media with $\mu_r = 1$ [11]. It is also possible to realize a “*chiral vacuum*,” which enables Brewster's effect for any incident angles, by adjusting permittivity, permeability, and chirality parameters [12].

Negative refraction

The refractive index n is defined as

$$n = \sqrt{\varepsilon_r} \sqrt{\mu_r}, \quad (1.1)$$

and it is obvious that the value of n becomes negative for $\varepsilon_r, \mu_r < 0$. In 1968, Victor Veselago theoretically considered the negative refractive index and predicted various extraordinary phenomena occurred in the medium [13]. For instance, Snell's law tells us that light entering negative-refractive-index medium from ordinary medium with $n > 0$ “negatively refracts” as shown in Fig. 1.2(c). If the medium with $n < 0$ could be realized for all the visible spectrum, an object in the medium strangely appears for an observer outside as shown in Fig. 1.2(d).[§] Negative wavenumber or negative phase velocity in the medium with $n < 0$ is also unique characteristics. In the medium, backward propagation, where the direction of phase flow is opposite to that of energy flow, is realized. The medium is often called a “*left-handed medium*,” because the electric field, magnetic field, and wave vector forms a “left-handed” triplet [13].

More than 30 years after Veselago's proposal, the negative refraction was verified by Smith's group using composite structures composed of metal wires and SRRs in microwave region [16]. The negative refraction has been realized in optical region using another type of structure called fishnet structure [17].

[§]The image can be easily calculated with the help of a ray-tracing software like POV-RAY [14]. Other examples have been illustrated in Ref. [15]

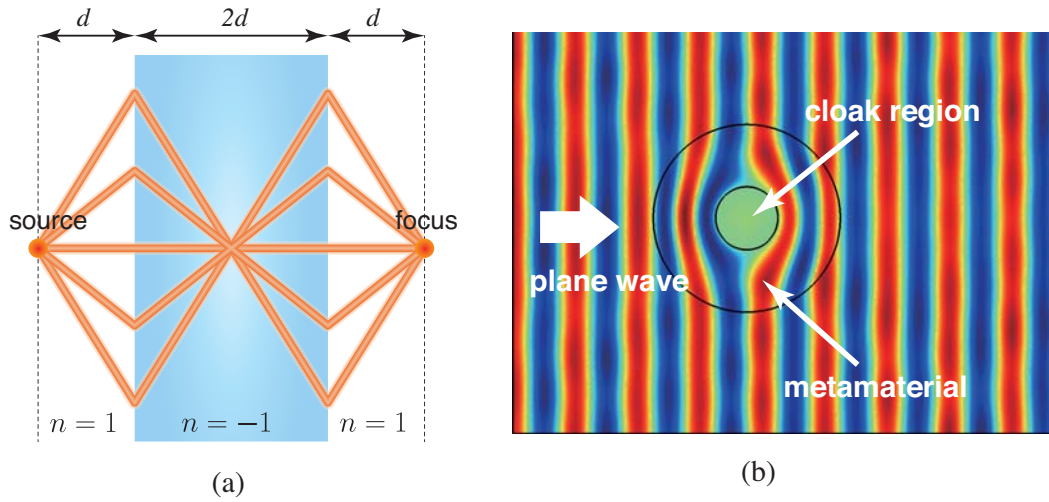


Figure 1.3: Typical applications of metamaterials. (a) Superlens. (b) Cloaking metamaterial. Metamaterial with designed parameter distributions is located between the outer and inner circles. Incident plane waves cannot invade the cloak region inside the inner circle. The computation was performed by a commercial software COMSOL MULTIPHYSICS.

One of the most significant applications of the negative refraction is a “*superlens*” or “*perfect lens*.” Pendry considered a flat slab with $\varepsilon_r = \mu_r = -1$, which works as a lens as shown in Fig. 1.3(a), and showed that the flat lens overcomes a diffraction limit $\sim \lambda/2$, which provides the resolution limit of conventional lenses [18]. In the superlenses, the enhancement of evanescent waves, which would be quickly attenuated during propagation in normal media ($n > 0$), contributes to the sub-wavelength diffraction-free imaging [19]. The concept of the superlens has been confirmed in microwave region with metal wires and SRRs [20], and in optical region with a metal slab under specific conditions [21, 22].

Metamaterial cloaking

It is well known that light passage can be deformed depending on spatial distributions of medium parameters. A typical example is a mirage. If the refractive index of the air is spatially distributed due to temperature inhomogeneity, the light

prefers to travel through lower air-density space with lower refractive index to minimize the optical path length according to Fermat's principle, and, consequently, the optical path is bent. This fact suggests that light propagation could be controlled by designing the distributions of the medium parameters. However, Fermat's principle is only valid in short-wavelength limit, where the light can be regarded as a ray and diffraction is ignored.

Transformation optics independently proposed by Pendry [23] and Leonhardt [24] provides general recipes to control the light propagation in more arbitrary way without the restraints mentioned above. The concept of the transformation optics is based on the fact that the forms of Maxwell equations can be maintained through a coordinate transformation by allocating the specific distributions of permittivity and permeability derived from the transformation. Because the coordinate transformation can be arbitrary, it is possible to render an object invisible for light. This invisible cloaking is realized by controlling the light passages so as to avoid the object as shown in Fig. 1.3(b) [25]. It should be noted that the EM fields outside the cloak are identical to those of the original plane wave.

The cylindrical cloaking shown in Fig. 1.3(b) was experimentally demonstrated in microwave region with composite structures of electric and magnetic metamaterial [26]. If the transformation is a conformal map, the transformation optics can be realized using only dielectric media. This idea enables another type of cloaking device, called carpet cloak [27], which has been implemented in microwave region [28] and optical region [29]. The concept of the transformation optics is quite general, and a lot of applications except the invisible cloaks have been proposed and demonstrated to control propagation of EM waves [30, 31].

1.1.3 Transmission-line metamaterials

We have so far discussed bulk metamaterials, which work as artificial media, while another type of metamaterial called a *transmission-line metamaterial* has also attracted much attentions. A conventional transmission line can be regarded as an infinite capacitor-inductor ladder as shown in Fig. 1.4(a). The propagation of sinusoidal signals with the angular frequency of ω can be described by the following

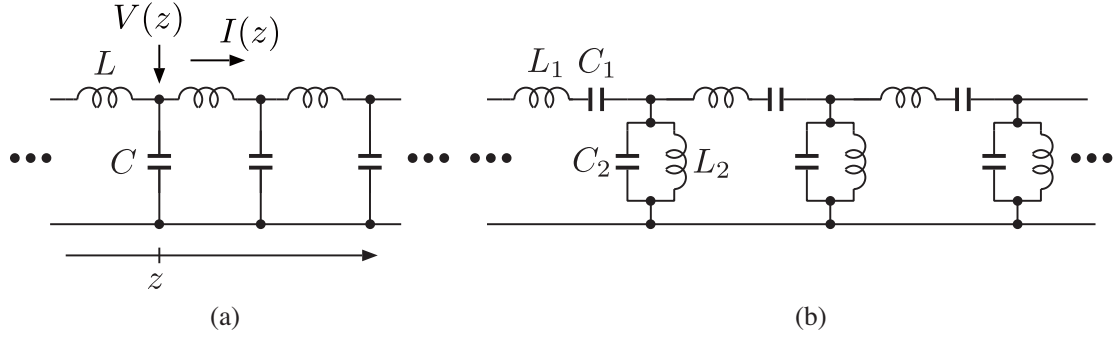


Figure 1.4: (a) Conventional transmission line. (b) CRLH transmission line.

telegrapher's equations:

$$\frac{d\tilde{V}(z)}{dz} = i\omega L\tilde{I}(z), \quad (1.2)$$

$$\frac{d\tilde{I}(z)}{dz} = i\omega C\tilde{V}(z), \quad (1.3)$$

where $V(z) = \tilde{V}(z)e^{-i\omega t} + \text{c.c.}$ and $I(z) = \tilde{I}(z)e^{-i\omega t} + \text{c.c.}$ represent the voltage applied to the capacitor and the current flowing through the inductor at position z , respectively. The telegrapher's equations are written in the same form as the Maxwell equations for sinusoidal plane waves as follows:

$$\frac{d\tilde{E}(z)}{dz} = i\omega\mu\tilde{H}(z), \quad (1.4)$$

$$\frac{d\tilde{H}(z)}{dz} = i\omega\varepsilon\tilde{E}(z). \quad (1.5)$$

Then, the telegrapher's equations can be identified with Maxwell equations by the following replacements:

$$\varepsilon \leftrightarrow C, \quad \mu \leftrightarrow L. \quad (1.6)$$

The propagation of the signals is characterized by the wavenumber $k = \omega\sqrt{L}\sqrt{C}$ and the characteristic impedance $Z = \sqrt{L/C}$.

We next consider a different transmission line as shown in Fig. 1.4(b). The

telegrapher's equations can be easily obtained as

$$\frac{d\tilde{V}(z)}{dz} = i\omega L_1 \left(1 - \frac{\omega_1^2}{\omega^2}\right) \tilde{I}(z), \quad (1.7)$$

$$\frac{d\tilde{I}(z)}{dz} = i\omega C_2 \left(1 - \frac{\omega_2^2}{\omega^2}\right) \tilde{V}(z), \quad (1.8)$$

where $\omega_1 = 1/\sqrt{L_1 C_1}$ and $\omega_2 = 1/\sqrt{L_2 C_2}$. In this case, the relationship given by Eq. (1.6) is modified as

$$\varepsilon \leftrightarrow C_2 \left(1 - \frac{\omega_2^2}{\omega^2}\right), \quad \mu \leftrightarrow L_1 \left(1 - \frac{\omega_1^2}{\omega^2}\right). \quad (1.9)$$

Both terms in Eq. (1.9) is positive for $\omega > \omega_1, \omega_2$, while they are negative for $\omega < \omega_1, \omega_2$. In the latter case, the wavenumber k becomes negative, and backward propagation, or negative phase velocity, can be attained. This transmission line is called a “*composite right/left-handed (CRLH) transmission line*,” because forward and backward propagations coexist depending on the frequency [32–35]. Unlike the negative refraction induced by resonant elements such as SRRs, condition for backward propagation in the CRLH transmission line is satisfied in wide spectral range. The transmission lines can be also considered as metamaterials because the unit cell of the ladder network is assumed to be much smaller than the operating wavelength in the derivation of the telegrapher's equations. By extending the left-handed transmission lines in two dimensions, it is possible to achieve various phenomena of metamaterials, such as negative refraction [32] and focus beyond diffraction limit [36], and so on.

1.1.4 Coupled-resonator-based metamaterials

Metamaterial elements, which are called *meta-atoms*, often include resonant structure such as an SRR shown in Fig. 1.2(a) or (b), in order to enhance specific physical effects like magnetic response. They resonantly respond to EM waves at a specific frequency or resonant frequency, and can be regarded as an artificially-designed two-level atoms as shown in Fig. 1.5(a).

If two resonant structures are placed closely as shown at the top of Fig. 1.5(b), these two resonators are coupled and hybridization effects emerge [37]. A typical

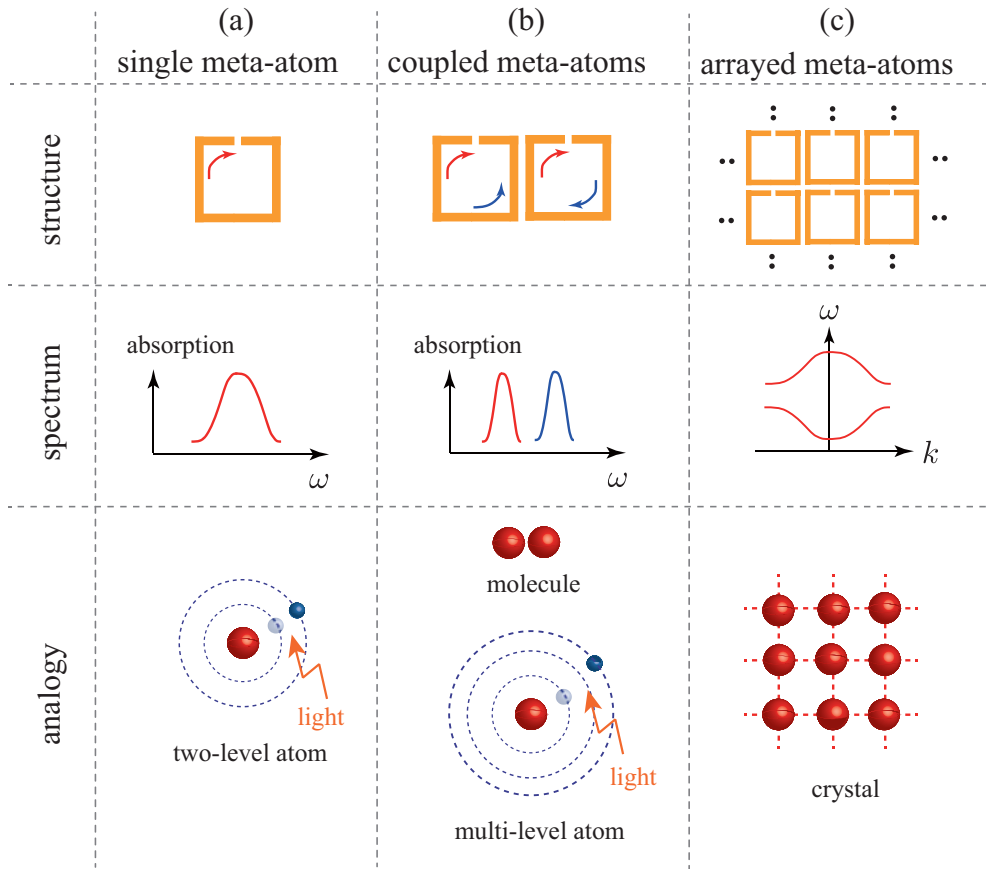


Figure 1.5: Classification of coupled-resonator-based metamaterials. (a) Single meta-atom. (b) Coupled meta-atoms. (c) Arrayed meta-atoms.

example of hybridization effects is resonant frequency splitting as shown at the middle Fig. 1.5(b). In this sense, the element of these metamaterials can be regarded as an artificial molecule or a multi-level atom with multiple absorption spectrum. The hybridizations depend on the structures of each meta-atom, relative alignment of the meta-atoms, and the number of meta-atoms. For example, it has been shown that the relative orientation between two SRRs have influence on the absorption profiles of metamaterials like natural molecules, whose absorption spectra are also sensitive to the arrangement of atoms [38], and that a composite structure of three SRRs can have unnatural level splitting by tailoring the couplings among the SRRs [39]. In addition to the control of absorption spectra, the coupled SRRs can be used

for polarization conversion [40].

If resonant structures are arranged in an array with a specific symmetry as shown in Fig. 1.5(c), the resonant modes among numerous resonators form band structure in dispersion relations. The whole structure can be regarded as an artificial crystal or solid. If the unit structure is composed of a magnetic resonator such as an SRR, collective magnetic oscillation travels through the metamaterial [19, 41–44]. It is possible to design the shape of the band, which is determined by the coupling strength and the symmetry of the networks. For instance, metamaterials with specific symmetries realize a flat band [45, 46] and a dirac cone at Γ point [47].

In summary, these coupled-resonator-based metamaterials introduced above are expected to achieve more complex and versatile functionality than singly resonant metamaterials [48].

1.1.5 Classical model for quantum phenomena

It sounds a little strange that some of quantum phenomena can be *emulated* in classical systems. However, if the quantum phenomena stem from the wave nature of quanta,[¶] it is natural that these phenomena can be realized using classical waves, such as electromagnetic waves, acoustic waves, and so on. Especially, a resonator that oscillates at a specific frequency is often used as a building block for quantum systems, and coupled resonators have been studied in an analogy to quantum phenomena in atomic system, such as level repulsion [49], stimulated Raman effect [50], Bloch oscillation [51], and so on. The classical models extract primary parts from the complex quantum systems, and provide us a deep insight into original quantum phenomena. The classical models, especially circuit models, are useful to design metamaterials that bring out the same phenomena as atomic systems, because electromagnetic response of the structures much smaller than the wavelength of the interacting electromagnetic waves can be well described by lumped circuit elements.

[¶]Quantum effects derived from wave-particle duality are difficult to emulate in classical systems.

1.2 Outline of this thesis

As described in Sec. 1.1.4, coupled-resonator-based metamaterials can show versatile functionality beyond natural materials by designing the structure of each meta-atom and the symmetry of the coupling network. In addition, metamaterials can emulate quantum effects, which originate from the wave nature of quantum systems. In this thesis, we propose coupled-resonator-based metamaterials that simulate quantum systems. All the subjects have been intensively investigated in the field of atomic physics and/or can be well described in analogy with quantum systems. Beyond phenomenological similarities, both of the original quantum system and metamaterial implementation are governed by the same differential equations. The main subjects are classified into four topics: simulation of Schrödinger equation in Chap. 2; simulation of superluminal and slow/stopped light for baseband signal in Chap. 3 and Chap. 4; metamaterial analogy to electromagnetically induced transparency and its application to storage of EM waves in Chap. 5 and Chap. 6; nonlinearity enhancement using doubly resonant metamaterial in Chap. 7. The contents in each chapter are summarized as follows:

- **Chapter 2: Simulation of closed quantum systems**

We introduce two LC (inductor-capacitor) resonators coupled with each other as a classical model of a two-level atom isolated from an environment. By coupling infinite numbers of resonators in a chain, Schrödinger equation in one dimension can be emulated. The wavefunction expressed by a complex function in a quantum system is represented by the combination of two real functions in the coupled-resonator model. We also propose a method to simulate Schrödinger equation in a vector potential by introducing a nonreciprocal element. We demonstrate quantum effects such as tunneling effect and Aharonov-Bohm effect, using a circuit simulator.

- **Chapter 3: Circuit simulation of superluminal light for baseband signal**

This chapter and the next chapter deals with circuit models, which emulate the control of group velocity in atomic systems. We focus on superluminal

propagation in Chap. 3 and slow or stopped light in Chap. 4. As introduction, the propagation speed of light pulse in dispersive media is described, and the group velocity is defined in the dispersive relation. We show that superluminal or negative group velocity can be realized in negative-dispersion slope or anomalous dispersion, and that negative group delay is also possible for baseband signals with electronic circuits whose phase response has negative slope in the vicinity of the frequency origin. We experimentally demonstrate that the output signal through the circuits precedes the input signal with maintaining the pulse shape. The relations to superluminality and causality are also discussed.

- **Chapter 4: Circuit simulation of slowing and storing light for baseband signal**

In this chapter, we deal with a circuit analogy to deceleration or storage of light in highly dispersive media, which can be regarded as an opposite limit of superluminal propagation described in the previous chapter. First, electromagnetically induced transparency (EIT), which realizes a highly dispersive medium and slow propagation, is introduced from a phenomenological point of view, and procedures for storage of light in the EIT media are illustrated with its condition. Next, we propose a circuit model to mimic slow propagation and storage of light, and demonstrate the control of pulse propagation, i. e. deceleration or storage of the pulse, for baseband signals. The condition for the storage of the baseband signal is also discussed in comparison with that for the atomic EIT system.

- **Chapter 5: Artificial atoms interacting with electromagnetic fields**

In comparison with the isolated quantum systems discussed in Chap. 2, quantum systems interacting with external fields are described. We focus especially on a two-level atom, which has a single absorption profile, and a three-level atom, which shows EIT phenomena with narrow-band transparency in a broad absorption profile. After the analysis of each quantum system using Schrödinger equation derived from its Hamiltonian, each classical analogy is introduced. As the classical analogy, the circuit models are first introduced,

and then the metamaterial implementations are reviewed. The complete analogy is established between the atomic media and the metamaterials.

- **Chapter 6: Storage of electromagnetic waves in metamaterial**

This chapter focuses on the storage of EM waves in metamaterial. Tunable metamaterial that mimics EIT effects induced in three-level atoms is proposed. It has variable capacitors, or varactor diodes, which enable us to dynamically control the EIT effects by applying bias voltage. After the analysis with its circuit model, we demonstrate semi-static control of EIT effects such as sharp transparency and slow propagation by observing the transmission spectra and the group delays for various bias voltages. Next, amplitude modulation of continuous waves and storage of an EM pulse are demonstrated by dynamically changing the transmission property of the EIT metamaterial. It is also confirmed that the metamaterial correctly stores and reproduces the phase distribution of propagating EM waves.

- **Chapter 7: Nonlinearity enhancement using doubly resonant metamaterial**

The topic of this chapter is enhancement of nonlinear electromagnetic response, especially second harmonic generation (SHG), in metamaterials. We start with a conventional method using singly resonant metamaterial that resonates for fundamental waves, and introduce doubly resonant metamaterial that resonates for both of fundamental waves and second harmonic waves in order to further enhance the SHG process. It is also described that these nonlinear metamaterials can be regarded as artificial four-level atoms. The doubly resonant metamaterial shows SHG enhancement around two orders of magnitude, compared with the singly resonant metamaterial.

- **Chapter 8: Summary and discussion**

The summary and discussion are provided. We also mention the relations with recent topics and future works.

From Chap. 3 to Chap. 6, the central subject is the control of the group velocity related superluminal or subluminal propagations, and they are closely related.

As a summary of this section, we classify the subjects in various points of views.

- Isolated quantum system or open quantum system

The quantum systems can be classified into two systems: isolated quantum systems where energy is conserved; open quantum systems which interact with outer space and exchange energy. Chapter 2 deals with the former case, and the other chapters deal with the latter case.

- Non-resonant metamaterial or resonant metamaterial

Except Chap. 3 and 4, which are designed for baseband signals, the structures are based on coupled resonators. Even for the models operating for the baseband signals, we also refer to them as “*metamaterials*,” which are usually used for oscillating waves. This is justified because elements of the models proposed in Chap. 3 and 4 are distributed homogeneously enough that the signal change for neighboring elements is negligibly small.

- Artificial atom or crystal

The coupled resonators aligned in a chain, which provide the classical analogy to Schrödinger equation discussed in Chap. 2, can be regarded as arrayed meta-atoms or artificial crystal introduced in Chap. 1.1.4. They are also regarded as transmission-line metamaterial whose dispersion relation is the same as that of the Schrödinger equation. On the other hand, the EIT metamaterial in Chap. 5 and 6 and the doubly resonant metamaterial in Chap. 7 can be regarded as artificial atoms with three levels and four levels, respectively.

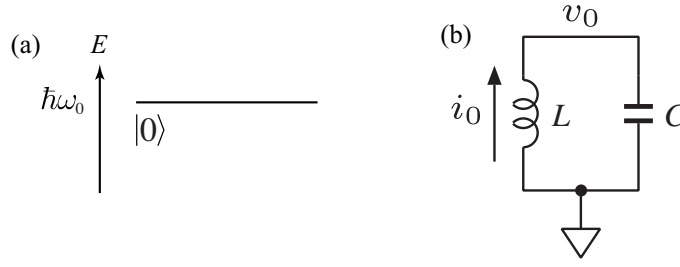
Chapter 2

Simulation of closed quantum systems

In this chapter, we propose circuit models in analogies with closed quantum systems, where total populations are conserved. We start with quantum systems with finite number of states and their circuit models. For simulating arbitrary two-level evolution, nonreciprocal circuit elements called gyrators are introduced. Next, the circuit model to simulate the Schrödinger equation is introduced. We also propose another circuit model to simulate the Schrödinger equation in the presence of vector potential. These circuit models can demonstrate various quantum phenomena, such as tunneling effect and Aharonov-Bohm effect, and help us to understand various concepts in quantum mechanics: the wavefunction expressed by a complex function; probability flow; Rabi oscillation in the two-level system, and so on.

2.1 Isolated quantum system

An isolated quantum system with a single state $|0\rangle$ as shown in Fig. 2.1(a) can be described by the Hamiltonian $\hat{H} = \hbar\omega_0|0\rangle\langle 0|$, where ω_0 is the eigenfrequency for $|0\rangle$. Assuming an initial state to be $|\psi(0)\rangle = |0\rangle$, the state for $t = t_0$ is expressed

Figure 2.1: (a) Isolated quantum state. (b) LC resonator.

by

$$|\psi(t)\rangle = e^{-i\hat{H}t_0/\hbar}|0\rangle = e^{-i\omega_0 t_0}|0\rangle. \quad (2.1)$$

Here, we consider an LC resonator as shown in Fig. 2.1. With the current in the inductor i_0 and the voltage across the capacitor v_0 , the equation of motions can be derived as

$$L \frac{di_0}{dt} = v_0, \quad C \frac{dv_0}{dt} = -i_0. \quad (2.2)$$

We introduce a complex number

$$u_0 = \sqrt{\frac{C_0}{2}}v_0 + i\sqrt{\frac{L_0}{2}}i_0, \quad (2.3)$$

and Eq. (2.2) can be written as

$$\frac{du_0}{dt} = -i\omega_0 u_0, \quad (2.4)$$

where $\omega_0 = 1/\sqrt{L_0 C_0}$. This is the equation of motions for a harmonic oscillator and the solution is given by

$$u(t_0) = e^{-i\omega_0 t_0} u(0). \quad (2.5)$$

There is clear relationship between the quantum system written with the time evolution given by Eq. (2.1) and the classical harmonic oscillator written by Eq. (2.5).

2.2 Two-level system

In this section, we consider a two-level system as a simplest example of interacting quantum system, and propose a classical counterpart.

We suppose that the quantum system as shown in Fig. 2.2(a) is composed of two quantum states $|1\rangle$ and $|2\rangle$ with the energy of $\hbar\omega_1$ and $\hbar\omega_2$ respectively, and these two levels are interacting with each other. Here, we introduce an Hamiltonian,

$$\hat{H} = \hbar\Omega_1 \frac{\hat{\sigma}_1}{2} + \hbar\Omega_2 \frac{\hat{\sigma}_2}{2} + \hbar\Delta \frac{\hat{\sigma}_3}{2}, \quad (2.6)$$

where $\Delta = \omega_1 - \omega_2$ and Pauli matrices are defined as

$$\hat{\sigma}_1 = \begin{pmatrix} 0 & 1 \\ 1 & 0 \end{pmatrix}, \quad \hat{\sigma}_2 = \begin{pmatrix} 0 & i \\ -i & 0 \end{pmatrix}, \quad \hat{\sigma}_3 = \begin{pmatrix} 1 & 0 \\ 0 & -1 \end{pmatrix}. \quad (2.7)$$

Time evolution for any interacting two-level systems, such as spin precession in magnetic field and optically driven Rabi oscillation in two-level systems, can be described by the Hamiltonian given by Eq. (2.6). The parameters Ω_1 and Ω_2 represent the interaction strength between the two states. It is easy to calculate the time evolution of the quantum system for the initial state with $|\psi(0)\rangle = |1\rangle$ and the population for $|1\rangle$, $P_1(t) = |\langle 1|\psi(t)\rangle|^2$ is given by

$$P_1(t) = \cos^2\left(\frac{\Omega t}{2}\right) + \left(\frac{\Delta}{\Omega}\right)^2 \sin^2\left(\frac{\Omega t}{2}\right), \quad (2.8)$$

where $\Omega = \sqrt{\Delta^2 + \Omega_1^2 + \Omega_2^2}$, and $P_2(t) \equiv |\langle 2|\psi(t)\rangle|^2 = 1 - P_1$. If $\Delta = 0$, we obtain

$$P_1(t) = \frac{1 + \cos \Omega t}{2}, \quad P_2(t) = \frac{1 - \cos \Omega t}{2}. \quad (2.9)$$

The quantum state oscillates between $|1\rangle$ and $|2\rangle$ at the rate $\Omega = \sqrt{\Omega_1^2 + \Omega_2^2}$ as shown in Fig 2.2(b) and it is called Rabi oscillation.

Before introducing the circuit model of the quantum system, we consider the flow of the probabilities between $|1\rangle$ and $|2\rangle$. If the state is written by $|\psi(t)\rangle = c_1(t)|1\rangle + c_2(t)|2\rangle$, we obtain

$$\frac{dP_1}{dt} = \frac{1}{\hbar} \text{Im}\{c_1^* c_2 \langle 1|\hat{H}|2\rangle\}. \quad (2.10)$$

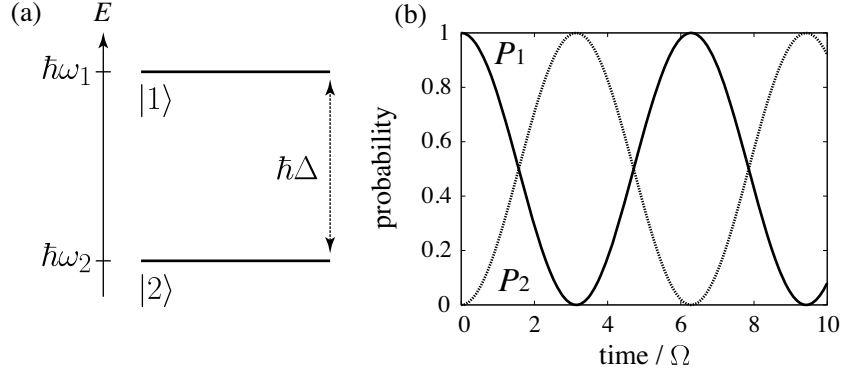


Figure 2.2: (a) Two-level system. (b) Rabi oscillations.

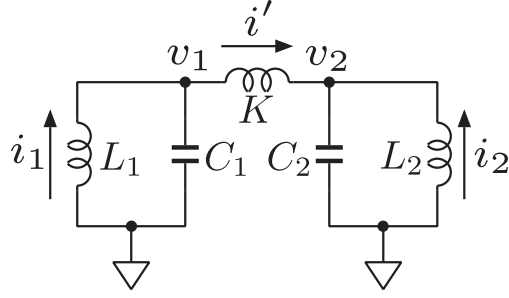


Figure 2.3: Inductor-coupled resonator.

If $\Delta = \Omega_2 = 0$ is assumed, the above relation is reduced to

$$\frac{dP_1}{dt} = -\frac{dP_2}{dt} = -|c_1 c_2| \Omega_1 \sin \phi, \quad (2.11)$$

where ϕ defines the phase difference in c_1 and c_2 as $c_1 c_2^* = |c_1 c_2| e^{i\phi}$. The direction of the probability flow depends on the relative phase ϕ , or the coherence between $|1\rangle$ and $|2\rangle$. This property is derived from the wave nature of the quantum system.

2.2.1 Inductor-coupled resonator

In this section, we consider two LC resonators connected with an inductor K as shown in Fig. 2.3. If we define the voltage applied to each capacitor as v_n ($n = 1, 2$)

and the current in each inductor as i_n , Kirchhoff's laws yield

$$L_n \frac{di_n}{dt} = -v_n, \quad (2.12)$$

$$C_n \frac{dv_n}{dt} = i_n + \frac{1}{K} \int_0^t (v_m - v_n) dt' \quad (m \neq n). \quad (2.13)$$

For small coupling $K \gg L_n$, Eq. (2.13) can be reduced to

$$C_n \frac{dv_n}{dt} = i_n - \frac{L_m}{K} i_m. \quad (2.14)$$

We introduce the following complex variables,

$$u_n = \sqrt{\frac{C_n}{2U}} v_n + i \sqrt{\frac{L_n}{2U}} i_n, \quad (2.15)$$

where U represents the total energy stored in two resonators

$$U = \frac{1}{2} \sum_n (C_n v_n^2 + L_n i_n^2). \quad (2.16)$$

The quantity $|u_n|^2$ can be regarded as the normalized energy stored in n -th resonator. With the new variables u_n , Eq. (2.14) is written as

$$\frac{du_n}{dt} = -i\omega_n u_n + i\omega_n \alpha \frac{u_m - u_m^*}{2}, \quad (2.17)$$

where the resonant frequency is defined as $\omega_n = 1/\sqrt{L_n C_n}$ and $\alpha = \sqrt{L_1 L_2}/K$. In small coupling limit $\alpha \sim 0$, the solution of Eq. (2.17) is written as $u_n = u_n(0) e^{-i\omega_n t}$. For finite $\alpha (\ll 1)$, the harmonic oscillation in each resonator is weakly driven by the oscillation in the other resonator. If $\omega_n \sim \omega_m$, the term with u_m in Eq. (2.17) contributes to effective excitation of the harmonic oscillation in n -th resonator, because of the near-resonance oscillation. On the other hand, counter-rotating term u_m^* in Eq. (2.17) can be neglected. With the approximation, we rewrite Eq. (2.17) in rotating frame expressed by $u_n = \tilde{u}_n e^{-i\bar{\omega} t}$, where $\bar{\omega} = (\omega_1 + \omega_2)/2$, as follows:

$$\frac{d\tilde{u}_1}{dt} = -\frac{i\Delta}{2} \tilde{u}_1 - \frac{i\Omega_1}{2} \tilde{u}_2, \quad (2.18)$$

$$\frac{d\tilde{u}_2}{dt} = \frac{i\Delta}{2} \tilde{u}_2 - \frac{i\Omega_1}{2} \tilde{u}_1, \quad (2.19)$$

where $\Delta = \omega_1 - \omega_2$, $\Omega_1 = -\alpha\omega_1 (\sim -\alpha\omega_2)$. It is easily found that these equations are identical to Eq. (2.6) for $\Omega_2 = 0$ by multiplying $i\hbar$. There is a definite analogy

Table 2.1: Correspondence between two-level system and coupled resonator.

Two-level system	Coupled resonator
Real part of wavefunction	v_n – Voltage of each capacitor
Imaginary part of wavefunction	i_n – Current in each inductor
Probability distribution	$\frac{Cv_n^2}{2} + \frac{Li_n^2}{2}$ – Energy stored in each resonator.
Coupling Ω_1	K – Coupling between resonators
Detuning Δ	$\omega_1 - \omega_2$ – Difference of resonant frequencies

between interacting two-level system and classical coupled resonator. We summarize the correspondence between the two systems in Table. 2.1.

The analogy helps us deeply understand abstract concepts of quantum mechanics and provides profound physical insight. It is well known that energy is exchanged between two classical resonators such as two tuning forks with the same resonant frequency ($\Delta = 0$) at a certain rate, which is determined by the coupling. This effect is a classical counterpart to Rabi oscillation in quantum system.

Power flow The probability in the two-level system corresponds to the normalized energy stored in two LC resonators. The energy flow from the left resonator to right one in Fig. 2.3 can be easily calculated for $C = C_1 = C_2$ and $L = L_1 = L_2$ as

$$J_{L \rightarrow R} = v_1 i' = -\frac{L}{K} v_1 (i_1 - i_2) = \frac{i\bar{\omega}U}{2} \frac{L}{K} (u_1 + u_1^*)(u_1 - u_1^* - u_2 + u_2^*). \quad (2.20)$$

Ignoring the terms, $u_1 u_1$, $u_1 u_2$, $u_1^* u_1^*$, and $u_1^* u_2^*$, which oscillate at a high frequency of $+2\bar{\omega}$ or $-2\bar{\omega}$, we obtain

$$J_{L \rightarrow R} = \frac{i\bar{\omega}U}{2} \frac{L}{K} (u_1 u_2^* - u_1^* u_2). \quad (2.21)$$

If the phase difference between the oscillation in each resonator is given by θ , i.e. $u_1/|u_1| = u_2/|u_2|e^{-i\theta}$

$$J_{L \rightarrow R} = \frac{\bar{\omega}UL}{K} |u_1||u_2| \sin \theta. \quad (2.22)$$

This expression indicates that the energy flows from a resonator with advanced phase into the other resonator. It is common to the quantum system, where the direction of the probability flow is determined by the phase difference between the two states as expressed by Eq. (2.11).

2.2.2 Gyration-coupled resonator

We introduce a circuit component called a “gyrator”, proposed by Tellegen. The gyrator was introduced as a fifth linear passive circuit element besides the capacitor, resistor, inductor, and transformer [52]. The gyrator can be represented by two voltage-controlled current sources as shown in Fig. 2.4(a) [53]. The input current I_1 and output current I_2 are controlled by the voltage-controlled current source attached to the output side and input side, respectively, as $I_1 = gV_2$ and $I_2 = -gV_1$, where g is a constant called mutual conductance. It is noted that this function could be implemented by a passive element, because the energies consumed in the two voltage-controlled current sources cancel each other out, $I_1V_1 + I_2V_2 = gV_2V_1 - gV_1V_2 = 0$.

The response of the gyrator depends on the propagation direction of the waves

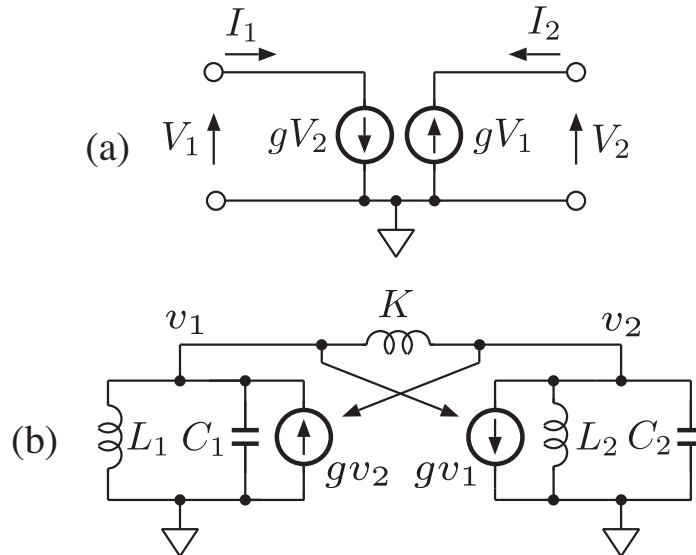


Figure 2.4: (a) Gyrator. (b) Gyrator-coupled resonator.

[54], because of the antisymmetric arrangement of the two current sources. The asymmetric response for different propagation directions is the most important property of the gyrator and is called nonreciprocity.* In fact, any passive circuit network with nonreciprocity can be constructed with the gyrators and the other reciprocal elements [55]. The nonreciprocity is utilized in some applications such as an isolator to separate incident and reflected waves by employing the difference in the response between forward and backward waves [56].

Here, we extend the coupled resonator in Fig. 2.3 by introducing the gyrator as shown in 2.4(b). For this gyrator-coupled resonator, the equation of motions is given by

$$L_1 \frac{di_1}{dt} = -v_1, \quad C_1 \frac{dv_1}{dt} = i_1 + \frac{1}{K} \int_0^t (v_2 - v_1) dt' + gv_2, \quad (2.23)$$

$$L_2 \frac{di_2}{dt} = -v_2, \quad C_2 \frac{dv_2}{dt} = i_2 + \frac{1}{K} \int_0^t (v_1 - v_2) dt' - gv_1. \quad (2.24)$$

Using the same procedure and the same approximation for deriving Eqs. (2.18) and (2.19), we obtain the following equations:

$$\frac{d\tilde{u}_1}{dt} = -\frac{i\Delta}{2}\tilde{u}_1 - \frac{i\Omega_1}{2}\tilde{u}_2 - \frac{\Omega_2}{2}\tilde{u}_2, \quad (2.25)$$

$$\frac{d\tilde{u}_2}{dt} = \frac{i\Delta}{2}\tilde{u}_2 - \frac{i\Omega_1}{2}\tilde{u}_1 + \frac{\Omega_2}{2}\tilde{u}_1, \quad (2.26)$$

where $\Omega_2 = -g/(2\sqrt{C_1 C_2})$. Suppose $|\psi(t)\rangle = \tilde{u}_1(t)|1\rangle + \tilde{u}_2(t)|2\rangle$, Eqs. (2.25) and (2.26) are formally rewritten with the Hamiltonian defined in Eq. (2.6) as

$$i\hbar \frac{d|\psi\rangle}{dt} = \hat{H}|\psi\rangle. \quad (2.27)$$

As the result, the gyrator coupled resonator can be regarded as classical analogy to the general two-level system. To express universal interaction of the two-level system in the circuit model, nonreciprocal element is indispensable. This circuit model can be applicable to the classical analogy of CP violation [57]

*While the gyrator is a passive nonreciprocal element, active element can be also used to induce nonreciprocity. Especially, nonreciprocal interaction using frequency mixing has been attractive much attentions recently. This is discussed later in Sec. 8.2

2.3 Circuit model of the Schrödinger equation

In this section, we consider a series of resonators as shown in Fig. 2.5, where each resonator composed of a capacitor C and an inductor L is coupled through inductors K to adjacent resonators. The following equations for the n -th resonator are derived from Kirchhoff's laws:

$$L \frac{di_n}{dt} = -v_n, \quad (2.28)$$

$$C \frac{dv_n}{dt} = i_n + \frac{1}{K} \int_0^t (v_{n-1} - v_n) dt' + \frac{1}{K} \int_0^t (v_{n+1} - v_n) dt', \quad (2.29)$$

where $v_n(t)$ and $i_n(t)$ represent the voltage across the capacitor and the current flowing through the inductor L , respectively. Assuming the coupling inductor K to be so large that almost all the energy U is stored in the resonators as

$$U = \frac{1}{2} \sum_n (Cv_n^2 + Li_n^2), \quad (2.30)$$

we introduce a dimensionless complex variable

$$u_n = \sqrt{\frac{C}{2U}} v_n + i \sqrt{\frac{L}{2U}} i_n, \quad (2.31)$$

which satisfies

$$\sum_n |u_n|^2 = 1. \quad (2.32)$$

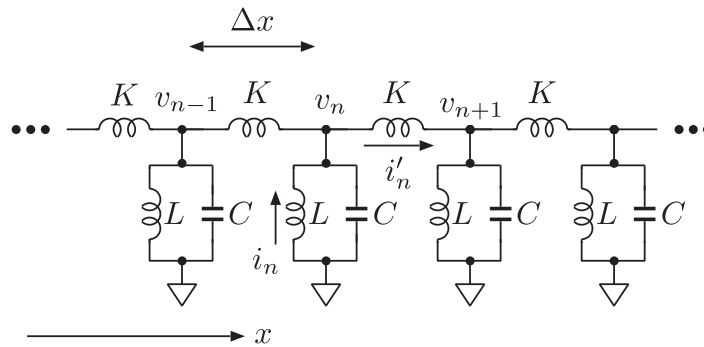


Figure 2.5: Circuit model for the Schrödinger equation.

We can rewrite Eqs. (2.28) and (2.29) as follows:

$$\frac{du_n}{dt} = -i\omega_0 u_n - \frac{1}{\sqrt{2CU}} \frac{L}{K} (i_{n-1} - 2i_n + i_{n+1}). \quad (2.33)$$

In the 0-th order approximation, where the last term in Eq. (2.33) is negligibly small ($K \rightarrow \infty$), i.e. the resonators are decoupled, Eq. (2.33) can be simplified as $du_n^0/dt = -i\omega_0 u_n^0$ with resonance frequency $\omega_0 \equiv 1/\sqrt{LC}$ and its solution is given by

$$u_n^0(t) = u_n(0) e^{-i\omega_0 t}. \quad (2.34)$$

The current can be expressed as

$$i_n^0(t) = -i\sqrt{\frac{U}{2L}} (u_n^0 - u_n^{0*}). \quad (2.35)$$

The same approximation used in Sec. 2.2.1 to derive Eqs. (2.18) and (2.19) from Eq. (2.17) is also valid for large K . This is because the first term in Eq. (2.35) effectively drives the oscillator due to resonance, while the second term, the counter-rotating term, has little influence on the motion of the oscillator. Ignoring the second term in Eq. (2.35), we obtain the motion equation of $u_n(t)$:

$$\frac{du_n}{dt} = -i\omega_0 u_n + \frac{i\omega_0}{2} \frac{L}{K} (u_{n-1} - 2u_n + u_{n+1}). \quad (2.36)$$

We will show that the above equation is identical to the discretized Schrödinger equation. Assuming that a unit cell consisting of L , C , and K occupies a length Δx in the x direction, each element constant should scale as

$$C = \gamma\Delta x, \quad L = \lambda/\Delta x, \quad K = \kappa\Delta x, \quad (2.37)$$

because the series impedance $j\omega K$ ($i = -j$) and the parallel admittance $j\omega C + 1/j\omega L$ should be proportional to Δx . Note that the resonance frequency $\omega_0 = 1/\sqrt{LC} = 1/\sqrt{\gamma\lambda}$ is independent of Δx . With $u_n = \psi_n \sqrt{\Delta x}$, Eq. (2.36) can be replaced by

$$\frac{d\psi_n}{dt} = -i\omega_0 \psi_n + \frac{i\omega_0}{2} \frac{\lambda}{\kappa(\Delta x)^2} (\psi_{n-1} - 2\psi_n + \psi_{n+1}), \quad (2.38)$$

and in the limit $\Delta x \rightarrow 0$, we have

$$\frac{d\psi(x)}{dt} = -i\omega_0 \psi(x) + i\omega_0 \sigma \frac{\partial^2 \psi(x)}{\partial x^2}, \quad (2.39)$$

Table 2.2: Correspondence between the parameters in the Schrödinger equation and those in the circuit model.

Schrödinger Eq.	Circuit model
$\text{Re } \psi$ – Real part of wavefunction	v_n – Voltage of each capacitor
$\text{Im } \psi$ – Imaginary part of wavefunction	i_n – Current in each inductor
$ \psi ^2$ – Probability distribution	$\frac{Cv_n^2}{2} + \frac{Li_n^2}{2}$ – Energy stored in each site
m – Mass	$\hbar\kappa\sqrt{\frac{\gamma}{\lambda}}$ – Coupling between resonators
V – Potential	$\hbar\omega_0$ – Resonant frequency

where $\sigma \equiv \lambda/(2\kappa)$, $x \equiv n\Delta x$ and the wavefunction is defined as $\psi(x) = \psi(n\Delta x) = \psi_n$. It is easy to show that the above equation is equivalent to the one-dimensional Schrödinger equation

$$i\hbar\frac{d\psi(x)}{dt} = -\frac{\hbar^2}{2m}\frac{\partial^2\psi(x)}{\partial x^2} + V\psi(x), \quad (2.40)$$

by using the relations

$$m \equiv \frac{\hbar}{2\omega_0\sigma} = \hbar\kappa\sqrt{\frac{\gamma}{\lambda}}, \quad V \equiv \hbar\omega_0 = \frac{\hbar}{\sqrt{\gamma\lambda}}. \quad (2.41)$$

In our circuit model of the Schrödinger equation, the potential energy V is represented by the resonance frequency ω_0 ($= 1/\sqrt{\gamma\lambda}$) and the mass m of the particle is proportional to the coupling inductance κ ($= K/\Delta x$). This is consistent with the fact that the coupling among the resonators becomes weak with increasing inductance K . By changing γ and λ in each resonator, keeping their ratio constant in order to keep the mass constant, we can represent the spatially dependent potential energy $V(x)$ without changing the mass m . The real and imaginary parts of the wavefunction $\psi(x)$ correspond to the voltage v_n and the current i_n , respectively. The normalized energy stored in the n -th resonator is given as $|u_n|^2$, so $|\psi(x)|^2 = |u_n|^2/\Delta x$ can be regarded as energy density normalized to satisfy $\int |\psi(x)|^2 dx = 1$. We summarize the correspondence between the parameters in the original Schrödinger equation and those in the circuit model in Table 2.2.

In the derivation of the discretized Schrödinger equation (2.38), we used two approximations: the weak coupling approximation for applying a perturbative approach and the rotating-wave approximation to eliminate the counter-rotating term. In Eq. (2.39), L/K determines the magnitude of the coupling or the perturbation, therefore the condition $L/K \ll 1$ is required for the weak coupling approximation. In addition, a condition on the excitation of waves is imposed for validating the rotating-wave approximation. The excitation frequency should be tuned around the resonant frequency ω_0 within the restricted linewidth $|\Delta\omega_0| \ll \omega_0$ so that we can ignore the nonresonant contributions.

Power flow The circuit model enables us to derive the power flow, which corresponds to the probability flow in quantum mechanics. The power flow p_n passing through the coupling inductor between the n -th and $(n+1)$ -th resonators is given by the product of the voltage v_n and the current i'_n in Fig. 2.5:

$$p_n = v_n i'_n = v_n \frac{1}{K} \int (v_n - v_{n+1}) dt = -v_n \frac{L}{K} (i_n - i_{n+1}). \quad (2.42)$$

We normalize p_n by the total energy U ,

$$j_n = \frac{p_n}{U} = \frac{i\omega_0}{2} (u_n + u_n^*) \frac{L}{K} [(u_n - u_n^*) - (u_{n+1} - u_{n+1}^*)], \quad (2.43)$$

where we have used Eq. (2.31). Averaging in time, the terms, $u_n u_n$, $u_n u_{n+1}$, $u_n^* u_n^*$, and $u_n^* u_{n+1}^*$, which oscillate at a high frequency of $+2\omega$ or -2ω , can be eliminated as

$$\begin{aligned} \langle j_n \rangle &= \frac{i\omega_0}{2} \frac{L}{K} [u_n^* (u_n - u_{n+1}) - u_n (u_n^* - u_{n+1}^*)] \\ &= \frac{i\omega_0}{2} \frac{\lambda}{\kappa \Delta x} [\psi_n^* (\psi_n - \psi_{n+1}) - \psi_n (\psi_n^* - \psi_{n+1}^*)]. \end{aligned}$$

In the limit $\Delta x \rightarrow 0$, $J(n\Delta x) = \langle j_n \rangle$ approaches

$$J(x) = \frac{i\hbar}{2m} \left(\psi \frac{d\psi^*}{dx} - \psi^* \frac{d\psi}{dx} \right), \quad (2.44)$$

which gives the probability flux in quantum mechanics [58]. With $\psi(x) = |\psi(x)|e^{i\theta(x)}$, $J(x)$ can be expressed as

$$J(x) = \frac{\hbar}{m} |\psi(x)|^2 \frac{d}{dx} \theta(x), \quad (2.45)$$

which means that the probability flow is proportional to the spatial change in the phase $\frac{d\theta}{dx}$ and the probability density $|\psi(x)|^2$.

2.4 Simulation of the Schrödinger equation

2.4.1 Procedures

For the simulation of the Schrödinger equation for a given potential $V(x)$, we set the resonance frequency of the n -th resonator $\omega_n = V(n\Delta x)/\hbar$ by adjusting L and C proportionally so as not to change the mass m . The mass can be controlled by adjusting the coupling inductor K . The absolute value of the resonant frequency

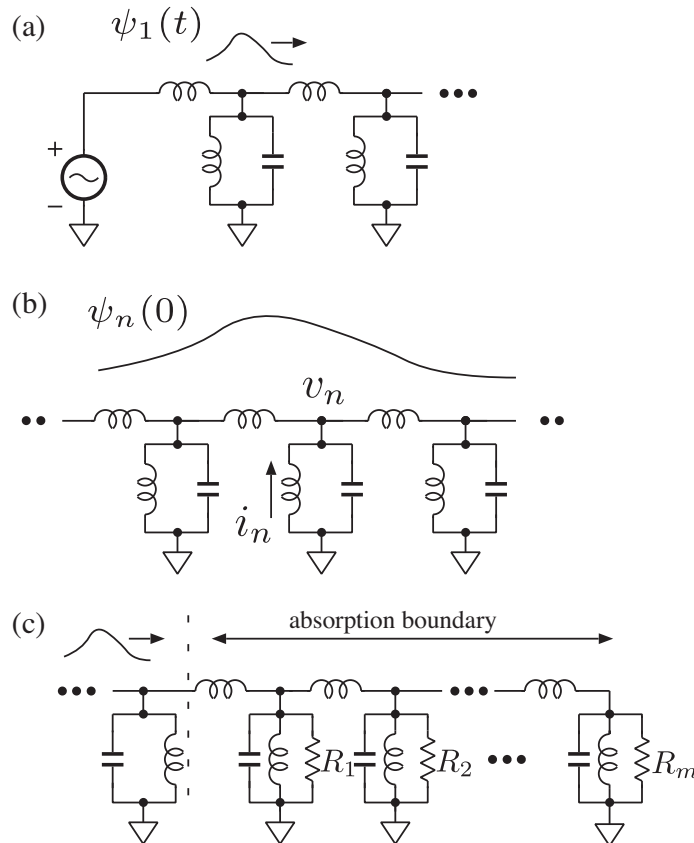


Figure 2.6: (a) Boundary condition at the edge of the circuit network. (b) Boundary condition imposed on the spatial distributions at $t = 0$. (c) Absorption boundary.

is not important because the potential energy can be shifted uniformly, $V'(x) = V(x) + \hbar\bar{\omega}$, by replacing the wavefunction ψ with $\psi' \equiv \exp(-i\bar{\omega}t)\psi$.

There are two ways to set the boundary conditions; (1) $\tilde{\psi}_1(t) = \psi(t, x_0)$ as a function of time at a fixed point $x = x_0$ and (2) $\tilde{\psi}_n(0) = \psi(0, n\Delta x)$ as a spatial function at the initial time $t = 0$. In the former case, $\tilde{\psi}_1(t)$ represents the excitation waveform of the first resonator as shown in Fig. 2.6(a). To satisfy the rotating-wave approximation, the spectrum center of the excitation, ω_c , should be near resonant $\omega_c \sim \omega_0$ and the spectrum width should be restricted as $\Delta\omega \ll \omega_c$. In the latter case, the initial spatial waveform $\tilde{\psi}_n(0)$ determines the initial condition on $v_n(0)$ and $i_n(0)$ in each resonator. In this case, the discretization step Δx should be fine enough to represent the initial waveform faithfully.

The reflection at the ends of the circuit array has to be suppressed sufficiently in the simulation of unbounded motion. We introduce an additional resistor R_a ($a = 1, 2, \dots, m$) in each resonator as in Fig. 2.6(c) in order to realize absorption boundary. The losses in the resistors gradually attenuate the amplitude of the propagating waves. The resistance R_1 at the entrance of the absorption boundary should be large enough not to change the parallel admittance composed of L and C : $1/R \ll |\omega_c C - 1/(\omega_c L)|$. The sudden change in the wave impedance causes reflection. With a series of gradually decreasing resistances, $R_1 > R_2 > R_3 \dots$, the incident wave can be effectively absorbed without reflection.

2.4.2 Free propagation

In this section, we simulate the free propagation of quantum waves in constant potential energy, using 200 coupled resonators and 10 damped resonators for absorption boundaries with the parameters shown in Table 2.3. To excite the wave, we connect a voltage source at the first resonator. The voltage source generates a sinusoidal wave with a Gaussian envelope, $V(t) = V_0 e^{-(t-\tau)^2(\Delta\omega)^2} \sin \omega_c t$ with $V_0 = 1.4$ mV, $\tau = 20$ ms, $\Delta\omega = 100$ Hz, and $\omega_c = 11$ kHz. Note that the carrier frequency ω_c is close to the resonant frequency of the circuit $\omega_0 = 1/\sqrt{LC} = 10$ kHz and the bandwidth is sufficiently limited, $\Delta\omega \ll \omega_c$.

The time evolution of the circuit is analyzed with a circuit simulator called

Table 2.3: Parameters for simulation of free propagation.

n	K / mH	L / mH	$C / \mu\text{F}$	ω_0 / kHz	$R / \text{k}\Omega$
1 ~ 200	25	10	1	10	—
201 ~ 210	25	10	1	10	$5 \times (n - 200)^{-1}$

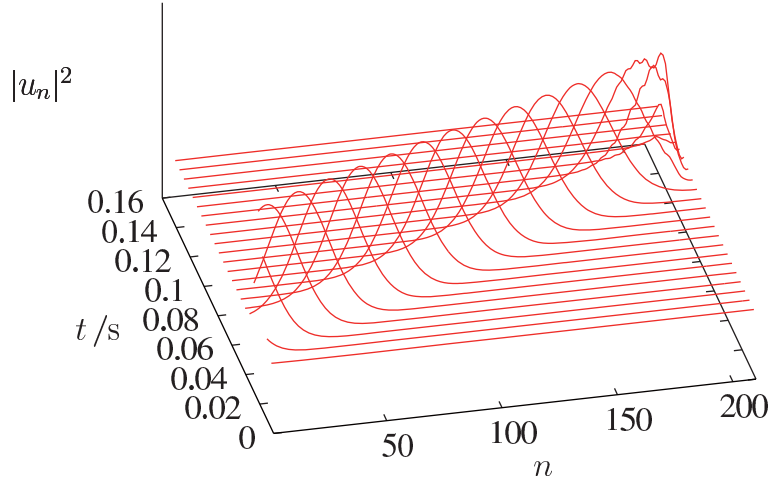


Figure 2.7: Simulation results for free propagation.

Ngspice [59]. A sample code is shown in Appendix A. The raw data of $|u_n|^2$ contains rapid oscillations attributed to the counter-rotating term in Eq. (2.33). It is possible to suppress these undesirable oscillations by decreasing the coupling L/K or by restricting the excitation spectrum close to ω_0 . To satisfy these conditions, however, we need to increase the number of circuits, which results in a longer simulation time. Another remedy is to smoothen $|u_n(t)|^2$ by averaging it over a certain period that is longer than the period of the rapid oscillation. Figure 2.7 shows the normalized energy distribution obtained by averaging the raw data of $|u_n|^2$ over 6.3 ms, which is ten times as long as $2\pi/\omega_0$. The propagation velocity is estimated as $\nu = 2.7$ circuit/ms from the simulation. The group velocity $v_g = d\omega/dk|_{\omega=\omega_c} = \sqrt{2\hbar(\omega_c - \omega_0)/m}$ for the quantum wave traveling in free space can be rewritten as $v_g = \sqrt{2(\omega_c - \omega_0)\omega_0 L/K} \cdot \Delta x$ in the circuit model. The delay per unit circuit is given as $\Delta x/v_g \sim 0.35$ ms, which is consistent with the simula-

tion result $1/\nu = 0.37$ ms. At the absorption boundary, the propagating wave is attenuated sufficiently and the reflection is negligibly small.

2.4.3 Tunneling problem

In this section, we consider the tunneling problem as illustrated in Fig. 2.8(a) with $n = 400$ coupled resonators. The potential wall, region II, is represented by $\Delta n = 5$ resonators with resonance frequency $\omega_w = 10.6$ kHz. The other regions, I and III, consist of 200 and 195 resonators with $\omega_0 = 10$ kHz. The circuit parameters are summarized in Table 2.4. The voltage source connected to the $n = 1$ resonator excites a Gaussian signal, $V(t) = V_0 e^{-(t-\tau)^2/(\Delta\omega)^2} \sin \omega_c t$, where $V_0 = 1.4$ mV, $\tau = 30$ ms, $\Delta\omega = 50$ Hz, and $\omega_c = 10.5$ kHz. The results are shown in Fig. 2.9. At the boundary of the wall, $n = 200$, some of the incident wave is reflected and interferes

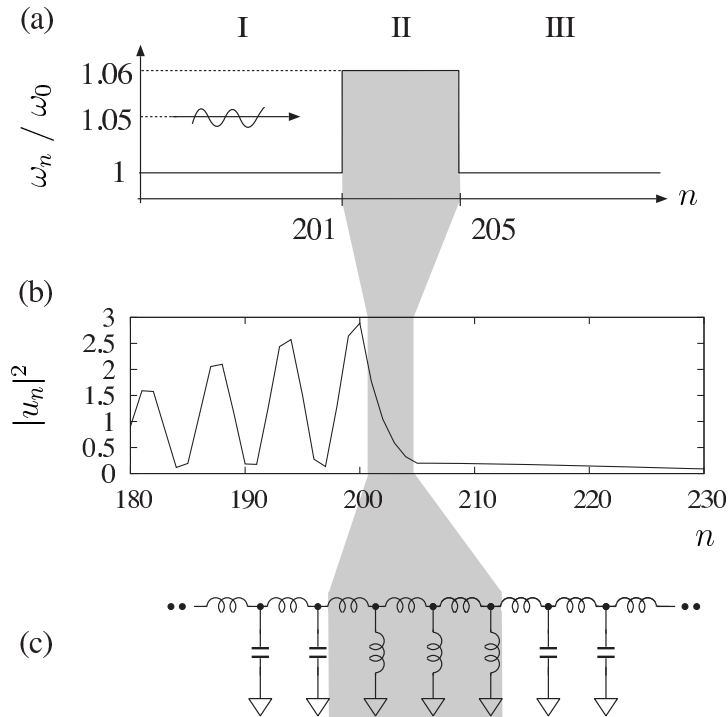


Figure 2.8: Tunneling problem. (a) Potential. (b) Simulation result at $t = 132$ ms in the vicinity of the potential wall. (c) Circuit representation for tunneling effects.

Table 2.4: Parameters for simulation of tunneling problem.

n	K / mH	L / mH	$C / \mu\text{F}$	ω_0 / kHz
1 ~ 200	25	10	1	10
201 ~ 205	25	9.43	0.943	10.6
206 ~ 400	25	10	1	10

with the reflected wave. In Fig. 2.8(b), an enlarged snap shot at $t = 132 \text{ ms}$ is shown. The incident wave exponentially decays in the wall domain (shaded), because we impose a condition in which the potential energy of the wall is higher than the energy of the incident wave, $\omega_w > \omega_c$. Some fraction of the incident wave survives after the exponential attenuation in the wall. The transmissivity, or the tunneling probability, is estimated as 21%. In quantum theory, the tunneling probability for a barrier of height V and width a is given as follows [60]:

$$T = \left\{ 1 + \frac{V_0^2 \sin^2 k'a}{4E(E - V_0)} \right\}^{-1}, \quad k' = \frac{\sqrt{2m(E - V_0)}}{\hbar}. \quad (2.46)$$

This can be rewritten in terms of the circuit parameters as

$$T = \left\{ 1 + \frac{(\omega_w - \omega_0)^2 \sin^2(\theta' \Delta n)}{4(\omega_c - \omega_0)(\omega_c - \omega_w)} \right\}^{-1}, \quad \theta' = \sqrt{\frac{2K}{L} \frac{\omega_c - \omega_w}{\omega_0}}, \quad (2.47)$$

which gives $T = 24\%$ in the simulated case.

As described above, the circuit model can simulate the Schrödinger equation correctly and the circuit representation provides a clear view on the tunneling problem. The admittance of the parallel LC resonators is $Y = jX$, where $X \equiv \omega_c C - 1/\omega_c L$. The sign of X changes from negative to positive at the resonant frequency ω_0 ; $X > 0$ in regions I and III ($\omega_c > \omega_0$) and $X < 0$ in region II ($\omega_c < \omega_w$). The capacitance C is dominant in the former case, and the inductance L is dominant in the latter case. Thus, we can simplify our circuit model as Fig. 2.8(c). In region I and III, the circuit forms an LC (inductor–capacitor) ladder network, which is well known as a transmission line, and the incident wave propagates freely. On the other hand, in region II, the circuit forms an inductor–inductor ladder network and

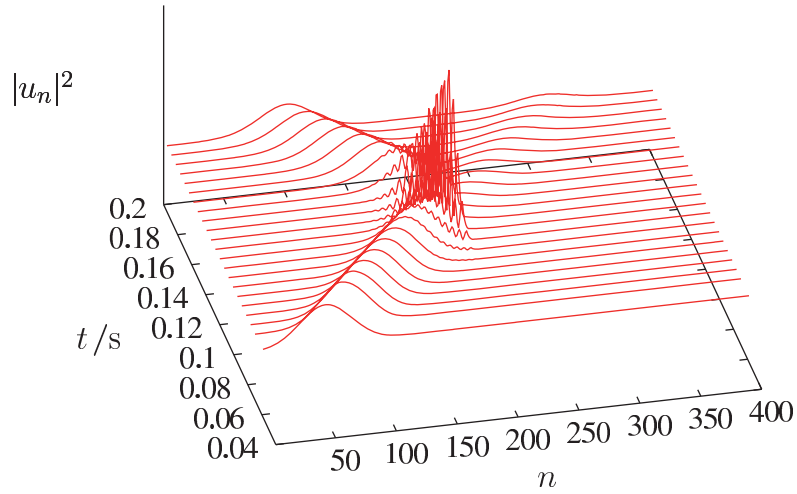


Figure 2.9: Simulation results for tunneling problem.

the propagating wave cannot exist. The voltage is divided in each ladder step and is exponentially attenuated in the wall domain. A small but finite voltage emerges from the wall domain as the result of multiple voltage divisions in the inductor ladder. This is the circuit interpretation of the tunneling phenomenon in quantum physics.

2.5 Circuit model of the Schrödinger equation in a vector potential

2.5.1 Discretization of the Schrödinger equation in a vector potential

In this section, we consider the Schrödinger equation in the presence of a vector potential \mathbf{A} or magnetic field $\mathbf{B} = \text{rot}\mathbf{A}$. Under the condition where the propagation of quantum waves is restricted in the x direction, the Schrödinger equation is written as

$$i\hbar \frac{d\psi(x)}{dt} = \frac{1}{2m} \left(-i\hbar \frac{\partial}{\partial x} - qA(x) \right)^2 \psi(x) + V(x)\psi(x). \quad (2.48)$$

Using the solution of the Schrödinger equation $\psi^{(0)}(x)$ in free space in the absence of a vector potential ($A = 0$), the solution of Eq. (2.48) can be expressed as $\psi(x) = \psi^{(0)}(x) e^{i\phi(x)}$, where

$$\phi(x) = \frac{q}{\hbar} \int_C A(x') dx' \quad (2.49)$$

represents an additional phase shift induced by the presence of $A(x)$ along a path C [58]. The additional phase shift depends on the direction of the integration. As a result, two counter-propagating waves acquire the same amount of additional phase shift but with opposite sign.

For modeling with electric circuits, the spatial difference should be expressed in finite difference form with a discretized wave function $\psi_n = \psi(n\Delta x)$ and discretized vector potential $A_{n+\frac{1}{2}} = A(n\Delta x + \frac{\Delta x}{2})$. In order to discretize the second-order derivative of x , we use two methods: forward difference $\vec{\delta}$ and backward difference $\overleftarrow{\delta}$ defined as

$$\vec{\delta} f(x) \equiv \frac{f(x + \Delta x) - f(x)}{\Delta x}, \quad \overleftarrow{\delta} f(x) \equiv \frac{f(x) - f(x - \Delta x)}{\Delta x}, \quad (2.50)$$

and we obtain

$$\begin{aligned} \left(-i\hbar \frac{\partial}{\partial x} - qA\right)^2 \psi &\sim (-i\hbar \vec{\delta} - qA)(-i\hbar \overleftarrow{\delta} - qA)\psi \\ &\sim -\hbar^2 \vec{\delta}(\overleftarrow{\delta} \psi) + iq\hbar \vec{\delta}(A\psi) + iq\hbar A(\overleftarrow{\delta} \psi) \\ &= -\hbar^2 \frac{\psi_{n+1} - 2\psi_n + \psi_{n-1}}{(\Delta x)^2} + iq\hbar \frac{A_{n+\frac{1}{2}}\psi_{n+1} - A_{n-\frac{1}{2}}\psi_{n-1}}{\Delta x}, \end{aligned}$$

where we omit the A^2 term because it is negligibly small. As a result, the discretized Schrödinger equation can be written as

$$i\hbar \frac{d\psi_n}{dt} = \frac{-\hbar^2}{2m} \frac{\psi_{n+1} - 2\psi_n + \psi_{n-1}}{(\Delta x)^2} + \frac{iq\hbar}{2m} \frac{A_{n+\frac{1}{2}}\psi_{n+1} - A_{n-\frac{1}{2}}\psi_{n-1}}{\Delta x} + V\psi_n. \quad (2.51)$$

2.5.2 Circuit model for the Schrödinger equation in a vector potential

We insert gyrators between the resonators in Fig. 2.5 as shown in Fig. 2.10. Kirchhoff's laws yield

$$L \frac{di_n}{dt} = -v_n, \quad (2.52)$$

$$C \frac{dv_n}{dt} = i_n + \frac{1}{K} \int (v_{n-1} - v_n) dt + \frac{1}{K} \int (v_{n+1} - v_n) dt - g_{n-\frac{1}{2}} v_{n-1} + g_{n+\frac{1}{2}} v_{n+1}. \quad (2.53)$$

By using the same procedures and the same approximation as described in Sec. 2.3, we obtain

$$\frac{du_n}{dt} = -i\omega_0 u_n + \frac{i\omega_0 L}{2} \frac{1}{K} (u_{n-1} - 2u_n + u_{n+1}) + \frac{1}{2C} (g_{n+\frac{1}{2}} u_{n+1} - g_{n-\frac{1}{2}} u_{n-1}), \quad (2.54)$$

which corresponds to Eq. (2.36) in Sec. 2.3. The last two terms represent the contribution of the vector potential. With Eqs. (2.37) and $\psi_n = u_n / \sqrt{\Delta x}$, Eq. (2.54) can be rewritten as

$$\frac{d\psi_n}{dt} = -i\omega_0 \psi_n + \frac{i\omega_0}{2} \frac{\lambda}{\kappa(\Delta x)^2} (\psi_{n-1} - 2\psi_n + \psi_{n+1}) + \frac{1}{2\gamma} \frac{g_{n+\frac{1}{2}} \psi_{n+1} - g_{n-\frac{1}{2}} \psi_{n-1}}{\Delta x}. \quad (2.55)$$

The above equation is clearly identical to Eq. (2.51) with Eq. (2.41) and

$$A_{n+\frac{1}{2}} = \frac{m}{q} \frac{g_{n+\frac{1}{2}}}{\gamma} = \frac{\hbar}{q} \cdot \kappa \omega_0 g_{n+\frac{1}{2}}. \quad (2.56)$$

The vector potential $A(x)$ can be represented by the mutual conductance $g_{n+\frac{1}{2}}$ of the gyrators in the circuit model.

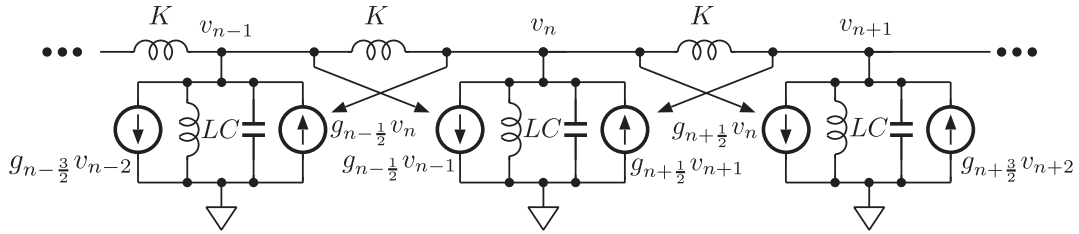


Figure 2.10: Circuit model for the Schrödinger equation in a vector potential.

2.5.3 Aharonov–Bohm effect

Suppose that a magnetic field B is applied at the center of a ring with radius r and a uniform vector potential A is generated along the ring counterclockwise as shown in Fig. 2.11(a). The wavepacket excited at the origin O is split into two parts, waves L and R , each of which propagates along the ring in opposite directions and interferes with each other at the opposite point P , $x = \pi r$. Without the vector potential, $A = 0$, the two waves constructively interfere at P . On the other hand, in the presence of the vector potential A , the vector potential induces additional phase shifts given by Eq. (2.49). The additional phase shifts at point P for wave L and wave R are expressed as

$$\phi_L(P) = \frac{q}{\hbar} \int_{C_L} A dx' = \frac{qAl}{\hbar}, \quad \phi_R(P) = \frac{q}{\hbar} \int_{C_R} (-A) dx' = -\frac{qAl}{\hbar}, \quad (2.57)$$

where C_L and C_R represent the integration path along counterclockwise and clockwise arcs, respectively, from O to P , and $l = \pi r$. Note that the direction of the traveling waves with respect to that of the vector potential determines the signs of the phase shifts. As a result, the interference fringe is shifted by a phase given as $\Delta\phi = \phi_L(P) - \phi_R(P) = 2qAl/\hbar = (q/\hbar)\Phi$, where Φ corresponds to the magnetic flux through the ring. This phenomenon is called the Aharonov–Bohm effect.

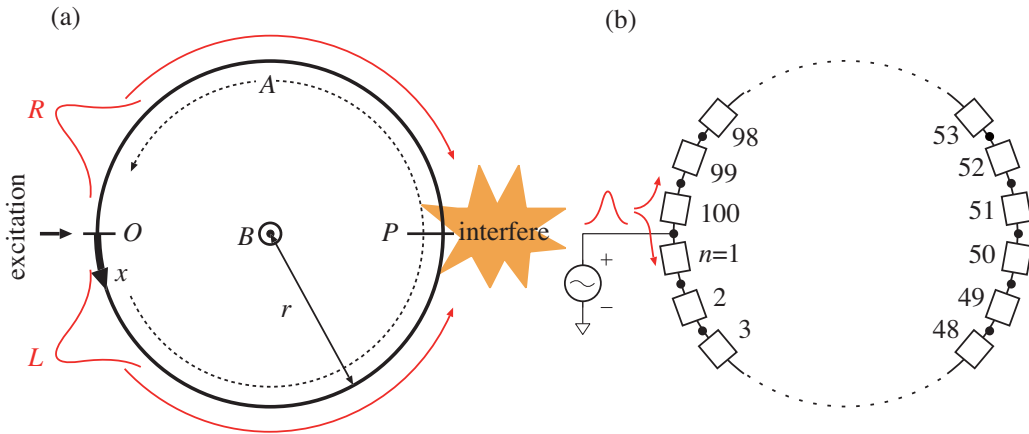


Figure 2.11: (a) Aharonov–Bohm effect. (b) Simulation setup for observing the Aharonov–Bohm effect. A loop is formed with the circuits in Fig. 2.10 (b) having 100 sections.

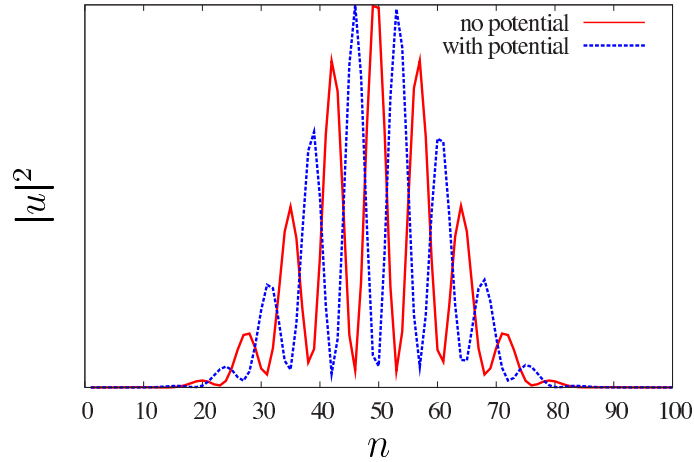


Figure 2.12: Simulation results for the Aharonov–Bohm effect at $t = 50$ ms.

Figure 2.11(b) illustrates the circuit model to simulate the Aharonov–Bohm effect. We make a loop by connecting each end of 100 components as shown in Fig. 2.11(b), and excite the circuits at a point between $n = 1$ and $n = 100$ with a voltage source. The parameters used in the demonstration are shown in Table 2.5. The voltage source provides a Gaussian signal, $V(t) = V_0 e^{-(t-\tau)^2(\Delta\omega)^2} \sin \omega_c t$ with $V_0 = 1$ V, $\tau = 20$ ms, $\Delta\omega = 100$ Hz, and $\omega_c = 10.3$ kHz. We demonstrate two cases: no vector potential with $g = 0$ and a finite potential with $g = 0.126$ mS.

In the absence of A , or g , two waves traveling in different directions constructively interfere at around $n = 50$ as shown by the red solid line in Fig. 2.12, because of the symmetry of the circuits. The symmetry can be broken by introducing the vector potential with finite g . When passing each element, the counterclockwise rotating wavepacket acquires an additional phase shift given by

$$\Delta\phi_L = \frac{q}{\hbar} A \Delta x = K \omega_0 g, \quad (2.58)$$

Table 2.5: Parameters for simulation of the Aharonov–Bohm effect.

n	K / mH	L / mH	C / μ F	ω_0 / kHz	g / mS
$1 \sim 100$	25	10	1	10	0 or 0.126

which can be derived from Eq. (2.56). On the other hand, the clockwise rotating wave experiences the same amount of additional phase shift, but with opposite sign, i.e. $\Delta\phi_R = -\Delta\phi_L$. The difference in the signs results from the nonreciprocity of the gyrators. The total phase difference between the two waves at $n = 50$ is estimated as $\phi = \Delta\phi_L \times 50 - \Delta\phi_R \times 50 = K\omega_0 g \times 100 \sim \pi$ for $g = 0.126$ mS, and so the destructive interference occurs at $n = 50$ as shown by the dashed line in Fig. 2.12. The interference fringes for two cases are anti-phase, which is a manifestation of the Aharonov–Bohm effect in the circuit model.

2.6 Discussions

We have introduced circuit models based on parallel inductor/capacitor resonators coupled with inductors in order to simulate the Schrödinger equation. The wavefunction $\psi(x)$, which is a complex function, can be represented by the combination of two real quantities: the voltage v_n and the current i_n in the resonators, and the probability $|\psi(x)|^2$ corresponds to the energy stored in the resonator. Our circuit model is equivalent to the circuit representation of the waveguide with a cut-off frequency $\omega_{\text{off}} = 1/\sqrt{LC}$ for electromagnetic waves and the propagation of the waves is governed by the Klein–Gordon equation [61]. In the low energy excitation limit, or non-relativistic limit, the Klein–Gordon equation can be approximated by the Schrödinger equation [62]. In the circuit analogy, the non-relativistic limit corresponds to the condition where the waves are excited near the resonant frequency, and then the circuit model we proposed obeys the Schrödinger equation under the condition.

The proposed models can be applied to various kinds of analysis of quantum problems: steady state problems in binding potentials and the dynamics of quantum wave propagation, even in the presence of vector potentials. We demonstrated various kinds of simulations, and all the results are in good agreement with the theoretical prediction derived from the original Schrödinger equation. In order to simulate the Schrödinger equation in the presence of a vector potential, we introduced the gyrator, which is a nonreciprocal component, and demonstrated the circuit simulation of the Aharonov–Bohm effect. The phase difference between two

waves is induced by the nonreciprocity, which makes the circuits behave differently for forward and backward waves, and the interference fringe formed by the two waves is shifted. The circuit models can be easily extended to multi-dimensional networks to simulate the Schrödinger equation in higher dimensions. The circuit analogy provides intuitive insight into quantum physics and may help find new phenomena in quantum physics or in circuit theory.

Chapter 3

Circuit simulation of superluminal light for baseband signal

Einstein's relativity theory assures that nothing can travel faster than the speed of light in a vacuum, $c = 299792458$ m/s and the communication faster than c violates causality, which means that a cause must precede its effect. Among several definitions of light speed, the group velocity, which gives the speed of the light envelope, is sometimes believed to define the speed of transmitting information, because the information is often encoded by modulating the amplitude of the light. However, Brillouin and Sommerfeld pointed out that the group velocity v_g could be larger than c , the speed of light in a vacuum, or even be negative [63]. For superluminal group velocities ($v_g > c$), the transit time of the light envelope through the medium is smaller than that in vacuum with the same wavelength. For negative group velocities, the envelope leaves before it enters the medium. In fact, Chu and Wong demonstrated experimentally that the light in a Ga:N crystal can be propagated at such extraordinary group velocities ($v_g > c$ or $v_g < 0$) under substantial absorption [64]. In 2000, Wang et al. realized the similar situation without absorption using gain-assisted linear dispersion and demonstrated light propagation at negative group velocities [65, 66].

In this chapter, we first provide the theoretical description on pulse propagation in dispersive media, introducing various types of group velocities: subluminal ($v_g < c$) group velocity, which is the main subject in the next chapter; superluminal

($v_g > c$) or negative ($v_g < 0$) group velocity. Next, some researches on superluminal or negative group velocity are reviewed. We derive the propagation equation for the envelope of the pulse traveling in a specific direction. Next, we introduce a circuit model to simulate the motion of the pulse envelope with negative group velocity and show experimental results [67, 68]. In the last of the chapter, the physical meanings of the superluminal propagation are discussed in terms of the causality.

3.1 Pulse propagation in dispersive media

In a dispersive medium, the wave equation in one dimension with respect to electric field $E(x, t)$ is given by

$$\frac{\partial^2 E}{\partial t^2} - c^2 \frac{\partial^2 E}{\partial x^2} = -\frac{1}{\epsilon_0} \frac{\partial^2 P}{\partial t^2}, \quad (3.1)$$

where $P(x, t)$ is the polarization of the medium induced by the electric field [69]. We introduce envelopes, $\mathcal{E}(x, t)$ and $\mathcal{P}(x, t)$ as

$$E(x, t) = \mathcal{E}(x, t) e^{-i(\omega_0 t - k_0 x)} + \text{c.c.}, \quad (3.2)$$

$$P(x, t) = \mathcal{P}(x, t) e^{-i(\omega_0 t - k_0 x)} + \text{c.c.}, \quad (3.3)$$

where c.c. stands for the complex conjugate of the preceding term. The carrier frequency ω_0 is located near the center of the spectrum of the electric field. The associated wavenumber $k_0 (> 0)$ will be determined later.

We assume that $\mathcal{E}(x, t)$ and $\mathcal{P}(x, t)$ are slowly varying functions with respect to space and time, and satisfy the following relations:

$$\left| \frac{\partial^2 \mathcal{E}}{\partial t^2} \right| \ll \omega_0 \left| \frac{\partial \mathcal{E}}{\partial t} \right| \ll \omega_0^2 |\mathcal{E}|, \quad \left| \frac{\partial^2 \mathcal{E}}{\partial x^2} \right| \ll k_0 \left| \frac{\partial \mathcal{E}}{\partial x} \right| \ll k_0^2 |\mathcal{E}|. \quad (3.4)$$

The same relations for $\mathcal{P}(x, t)$ are satisfied. If a pulse is introduced with envelope duration $\Delta\tau$, the first relation in Eq. (3.4) can be rewritten roughly as

$$\frac{|\mathcal{E}|}{\omega_0^2 \Delta\tau^2} \ll \frac{|\mathcal{E}|}{\omega_0 \Delta\tau} \ll |\mathcal{E}|. \quad (3.5)$$

In optical experiments, we can safely assume that the pulse width $\Delta\tau$ is much longer than the carrier period $2\pi/\omega_0$, and $\omega_0 \Delta\tau \gg 1$ is satisfied. Therefore the second

derivative terms can be neglected as second-order infinitesimals. The same is true for spatial derivatives. Thus the terms in Eq. (3.1) can be approximated as

$$\frac{\partial^2 E}{\partial t^2} \simeq \left[-2i\omega_0 \frac{\partial \mathcal{E}}{\partial t} - \omega_0^2 \mathcal{E} \right] e^{-i(\omega_0 t - k_0 x)} + \text{c.c.}, \quad (3.6)$$

$$c^2 \frac{\partial^2 E}{\partial x^2} \simeq c^2 \left[2ik_0 \frac{\partial \mathcal{E}}{\partial x} - k_0^2 \mathcal{E} \right] e^{-i(\omega_0 t - k_0 x)} + \text{c.c.}, \quad (3.7)$$

$$\frac{1}{\epsilon_0} \frac{\partial^2 P}{\partial t^2} \simeq \frac{1}{\epsilon_0} \left[-2i\omega_0 \frac{\partial \mathcal{P}}{\partial t} - \omega_0^2 \mathcal{P} \right] e^{-i(\omega_0 t - k_0 x)} + \text{c.c.} \quad (3.8)$$

We retained the first-order terms because the zeroth-order terms cancel as will be shown later. For slowly varying envelopes, the spectrum of the electric field is confined within narrow regions: $[\pm\omega_0 - \Delta\omega/2, \pm\omega_0 + \Delta\omega/2]$, where $\Delta\omega$ ($\sim \Delta\tau^{-1}$) represents the spectral width. Then the susceptibility of the medium $\chi(\omega, x)$ can be regarded as a linear function of ω within the spectral width, and the relation between $\mathcal{E}(x, t)$ and $\mathcal{P}(x, t)$ can be presented as

$$\mathcal{P}(x, t) = \epsilon_0 \chi_0 \mathcal{E}(x, t) + i\epsilon_0 \chi_1 \frac{\partial \mathcal{E}}{\partial t}(x, t), \quad (3.9)$$

where $\chi_0 = \chi(\omega_0)$ and $\chi_1 = (d\chi/d\omega)(\omega_0)$. The derivation of Eq. (3.9) is given in Appendix B. With the help of Eq. (3.9), Eq. (3.8) can be represented as

$$\frac{1}{\epsilon_0} \frac{\partial^2 P}{\partial t^2} \simeq \left[2\omega_0 \chi_1 \frac{\partial^2 \mathcal{E}}{\partial t^2} - i\omega_0 (2\chi_0 + \omega_0 \chi_1) \frac{\partial \mathcal{E}}{\partial t} - \omega_0^2 \chi_0 \mathcal{E} \right] + \text{c.c.} \quad (3.10)$$

By substituting Eqs. (3.6), (3.7), and (3.10) into the wave equation (3.1), we obtain

$$2\omega_0 \chi_1 \frac{\partial^2 \mathcal{E}}{\partial t^2} + \left[2i\omega_0 \left(1 + \chi_0 + \frac{\omega_0 \chi_1}{2} \right) \frac{\partial \mathcal{E}}{\partial t} + 2ic^2 k_0 \frac{\partial \mathcal{E}}{\partial x} \right] - [\omega_0^2 (1 + \chi_0) - c^2 k_0^2] \mathcal{E} = 0. \quad (3.11)$$

When we choose ω_0 and k_0 so as to satisfy the dispersion relation, $k_0 = n_0 \omega_0 / c$, where $n_0 = \sqrt{1 + \chi_0}$, we can remove the last term of Eq. (3.11). In addition, we assume $|\chi_1|/\Delta\tau \ll 1$, so that the first term of Eq. (3.11) can be negligible relative to the next term $2i\omega_0 \frac{\partial \mathcal{E}}{\partial t}$. This condition guarantees a linear dispersion relation within the bandwidth $\Delta\omega$.

Simplifying Eq. (3.11), we obtain a propagation equation for the envelope \mathcal{E} :

$$\frac{\partial \mathcal{E}}{\partial t} + v_g \frac{\partial \mathcal{E}}{\partial x} = 0, \quad (3.12)$$

where

$$v_g \equiv \frac{c}{n_0 + \frac{\omega_0 \chi_1}{2n_0}}, \quad (3.13)$$

represents the velocity of the envelope. Note that Eq. (3.13) can be derived from the well-known formula for group velocity:

$$v_g \equiv \left[\frac{\partial k}{\partial \omega}(\omega_0) \right]^{-1}, \quad (3.14)$$

where $k = \omega \sqrt{1 + \chi(\omega)}/c$. The solution of Eq. (3.12), $\mathcal{E}(x - v_g t)$, is a one-way propagating wave at the velocity of v_g .

The group velocity defined by Eq. (3.13) depends on the refractive index n_0 and the slope χ_1 of the electric susceptibility in frequency domain. Depending on the value of χ_1 , the group velocity can be classified into three cases. (I) For $\chi_1 > \frac{2n_0(1-n_0)}{\omega_0}$, the group velocity is less than c . (II) For $-\frac{2n_0^2}{\omega_0} < \chi_1 < \frac{2n_0(1-n_0)}{\omega_0}$, the group velocity exceeds c and superluminal propagation of light pulse is observed. (III) For $\chi_1 < -\frac{2n_0^2}{\omega_0}$, the group velocity becomes negative. In this case, the pulse comes out before it enters into the medium. Both of the two cases (II) and (III) are often referred to as *superluminal*, because the transit time of the pulse through the medium is less than that in a vacuum. If $n_0 \sim 1$, negative slope $\chi_1 < 0$, which is called anomalous dispersion, corresponds to the superluminal case, (II) or (III). In anomalous dispersive media $\chi < 0$, the refractive index $n = \sqrt{1 + \chi(\omega)}$ decreases with increasing the frequency ω .

3.2 Realization of anomalous dispersion for superluminal propagation

In order to realize superluminal propagation $v_g > c$ or $v_g < 0$, anomalous dispersion should be implemented. It is well known that the dispersive property dramatically changes in the vicinity of resonant absorption. Figure 3.1(a) shows the real part and imaginary part of the electric susceptibility (denoted as χ' and χ'' respectively) for a medium with Lorentz absorption. It is clear that the slope of χ'

becomes negative around the resonant frequency ω_0 (shaded region), and anomalous dispersion, or superluminal propagation, can be expected in this region. Based on this anomalous dispersion, Chu and Wong experimentally demonstrated that the light in a Ga:N crystal can be propagated at anomalous group velocities ($v_g > c$ or $v_g < 0$) in the absorption region [64]. However it is inevitable that the shape of the light pulse is strongly distorted due to the absorption, which is represented as the imaginary part χ'' . The standard definition of the group velocity loses its physical meaning if the waveform is strongly distorted. A new definition of group velocities that considers the distortion of the spectrum caused by the absorption was proposed recently [70].

After the demonstration of superluminal propagation under the absorption,

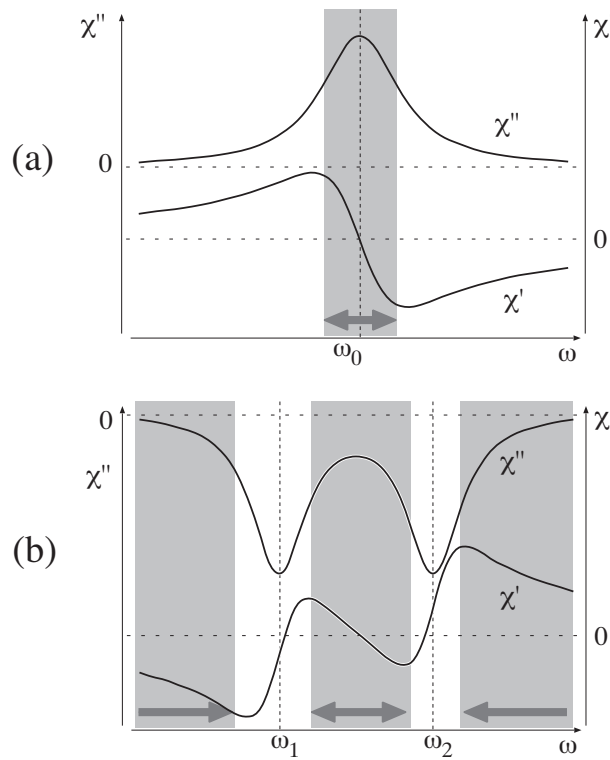


Figure 3.1: Real part χ' and imaginary part χ'' of susceptibility for (a) medium with an absorption line and (b) medium with two gain lines. Shaded regions correspond to the anomalous dispersive band.

some researchers attributed the unnatural phenomena to the heavy distortion of the pulse. To avoid the criticism concerned with the attenuation of the pulses, Wang et al. proposed anomalous dispersion without absorption using gain-assisted linear dispersion, and experimentally realized light propagation at negative group velocities [65, 66]. They used an active medium with two Raman gain profiles, whose susceptibility is shown in Fig. 3.1(b). The susceptibility of the gain lines is reversed compared with that of the absorption lines, and the anomalous dispersion is realized outside the gain lines. Especially, at the center of the gain lines, small $|\chi''|$ is expected and the distortion of the pulse is relatively small. As a result, the output pulse from the anomalous dispersive medium is almost identical to the input pulse by temporal displacement. In Wang's experiment, the output pulse transmitting through 6-cm medium precedes the input pulse by 63 ns, from which the group velocity is estimated to be $v_g = -6 \text{ cm}/63 \text{ ns} = -c/315$.

The superluminal propagation is counterintuitive and is likely to cause many misunderstandings. However, it is the direct result of the interference between waves with different frequencies and is consistent with relativistic causality. Anomalous dispersion with no absorption induces phase shifts that depend on the frequency, thereby enhancing the front part of the pulse by constructive interference and canceling the rear part by destructive interference. The pulse shape is maintained if the phase shift is a linear function of the frequency.

3.3 Negative group delay

Interference does not occur only in light propagation, but also in other wave or oscillation dynamics. Signals in electrical circuits also interfere. In lumped constant electronic circuits, we cannot define the group velocity, because there is no finite length scale. Instead, we can define the group delay, which is the time difference between the input and output signal envelopes. If it is negative, the output pulse precedes the input. The negative delays are closely connected to the superluminal or negative group velocities in spatially extended systems, which is discussed later.

3.3.1 Group delay

In this section, we extend the concept of the superluminal propagation to a lumped system as shown in Fig. 3.2, which may not have the dimension of length. If the linearity of the system is assumed, the relation between an input signal $v_{\text{in}}(t)$ and an output signal $v_{\text{out}}(t)$ is represented as

$$v_{\text{out}}(t) = h(t) * v_{\text{in}}(t), \quad (3.15)$$

where $h(t)$ is the impulse response of the system. Here we introduce Fourier transform defined as

$$\tilde{F}(\omega) = \int_{-\infty}^{\infty} f(t) e^{i\omega t} dt, \quad (3.16)$$

and express Eq. (3.15) in frequency domain as follows:

$$\tilde{V}_{\text{out}}(\omega) = H(\omega)\tilde{V}_{\text{in}}(\omega), \quad (3.17)$$

where $\tilde{V}_{\text{in}}(\omega)$, $\tilde{V}_{\text{out}}(\omega)$, and $H(\omega)$ are the Fourier transformed functions of $v_{\text{in}}(t)$, $v_{\text{out}}(t)$, and $h(t)$, respectively. The function $H(\omega)$ is called a transfer function, or frequency response, which determines the response of the linear system.

Ideal delay If the impulse response is given by $h(t) = \delta(t - t_d)$, where $\delta(t)$ is a delta function, Eq. (3.17) becomes $v_{\text{out}}(t) = v_{\text{in}}(t - t_d)$. The frequency response is

$$H(\omega) = e^{i\omega t_d}. \quad (3.18)$$

In this system, the output signal is delayed by t_d for any input signal. This ideal delay is valid only for positive delay $t_d > 0$, because the impulse response should be causal, in other words, $h(t) = 0$ for $t < 0$. The frequency response can be rewritten as $H(\omega) = A(\omega)e^{i\phi(\omega)}$, where $A(\omega)$ and $\phi(\omega)$ represent the amplitude response and the phase response respectively. For ideal delay,

$$A(\omega) = 1, \quad \phi(\omega) = \omega t_d \quad (3.19)$$

are derived. A flat amplitude response and linear phase response with respect to the frequency are required to realize ideal delay.

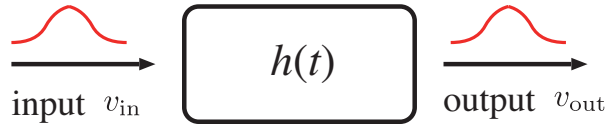


Figure 3.2: Lumped system.

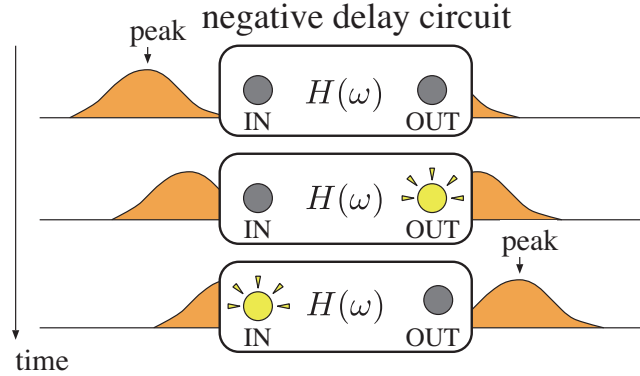


Figure 3.3: An electronic black box for negative delays. The input and the output are monitored by LEDs. When a pulse is fed to the input, the LED at the output lights up before the LED at the input.

Group delay It is impossible to realize negative delay for any input signal, but the negative delay is allowed for band-limited signals. Here we introduce the slope of the phase response at specific frequency $\omega = \omega_0$ as

$$t_d = \left. \frac{d\phi}{d\omega} \right|_{\omega_0}. \quad (3.20)$$

If the amplitude is unity $A(\omega) \sim 1$ and the phase is linear $\phi(\omega) \sim \omega t_d$ in the bandwidth of an input signal, Eq. (3.18) is valid for the band-limited signals and the output signal is temporally shifted by the delay t_d , which is called group delay. In this case, the causality, $h(t) = 0$ for $t < 0$, does not restrict the value of the group delay, and positive and negative group delay are allowed. For $t_d > 0$, the input precedes the output (normal delay) and for $t_d < 0$, the output precedes the input (negative delay) as shown in Fig. 3.3.

3.3.2 Superluminal propagation and negative delay

To translate the above discussion into light propagation through a dispersive medium of length L , we let v_{in} and v_{out} correspond to the envelopes of the input and output field, respectively. When monochromatic light with frequency ω is propagated in the medium, the phase of the field is shifted by $\phi(\omega) = k(\omega)L$, where $k(\omega)$ is the wavenumber in the medium. If $k(\omega)$ is linear in the bandwidth, we have with the help of Eq. (3.20)

$$t_{\text{d}} = L \left. \frac{dk}{d\omega} \right|_{\omega_0} = \frac{L}{v_{\text{g}}}, \quad (3.21)$$

where $d\omega/dk|_{\omega_0}$ is the group velocity v_{g} . The envelope of the light is delayed by L/v_{g} .

If the difference between the propagation time of the envelope in the dispersive medium and that in a vacuum with the same length L is negative, that is,

$$\Delta t = t_{\text{d}} - L/c = L(v_{\text{g}}^{-1} - c^{-1}) < 0, \quad (3.22)$$

then the light propagation in the medium is superluminal. There are two cases that satisfy this condition; $v_{\text{g}} > c$ and $v_{\text{g}} < 0$. In the former case, the output envelope precedes the output for the vacuum case but does not precede the input. In the latter case, the output precedes the input, or the medium produces the negative group delay $t_{\text{d}} < 0$.

3.4 Circuits and experiment

3.4.1 Negative delay circuit for baseband signals

In Fig. 3.4, we show a negative delay circuit for baseband ($\omega_0 = 0$) signals. This circuit is basically a non-inverting (imperfect) differentiator. Its transfer function is obtained as

$$H(\omega) = 1 - i\omega T, \quad (3.23)$$

where $T = RC$.

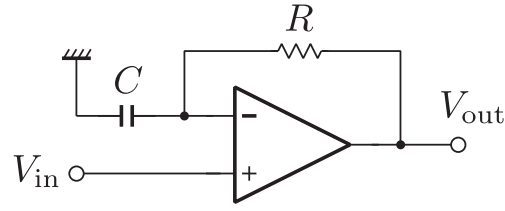


Figure 3.4: Negative delay circuit for baseband signal can be constructed with an operational amplifier. The transfer function is $H(\omega) = 1 - i\omega T$.

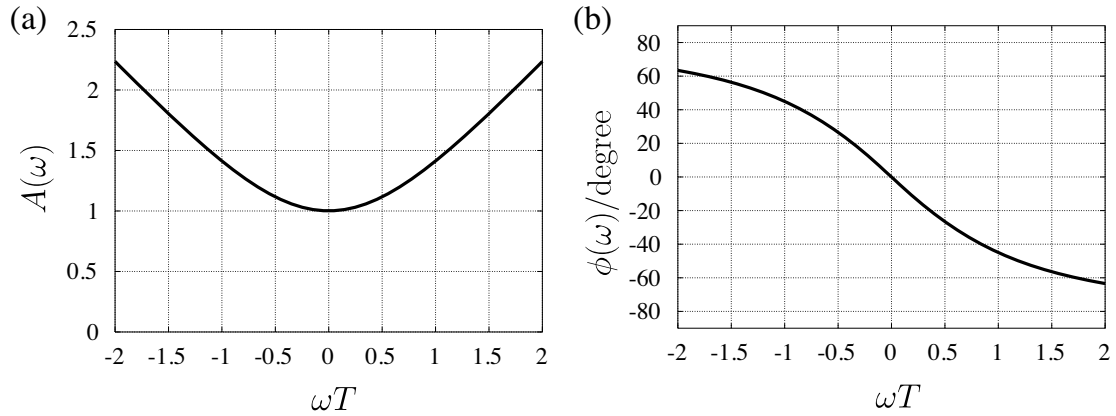


Figure 3.5: (a) Amplitude of the transfer function $A(\omega) = |H(\omega)|$ and (b) phase $\phi(\omega) = \arg H(\omega)$.

In the low-frequency region ($|\omega| \ll 1/T$), $H(\omega)$ is approximated by

$$A(\omega) = 1 + O(\omega^2 T^2), \quad (3.24)$$

$$\phi(\omega) = -\omega T + O(\omega^3 T^3), \quad (3.25)$$

which mean that the amplitude is nearly constant and the phase increases linearly with frequency. Then the group delay becomes negative:

$$t_d = \left. \frac{d\phi}{d\omega} \right|_{\omega=0} = -T < 0. \quad (3.26)$$

As seen in Fig. 3.5, the amplitude $A(\omega)$ and the phase $\phi(\omega)$ of the transfer function are not linear except when $|\omega|T \ll 1$ due to the higher order terms in Eqs. (3.24) and (3.25). These terms induce distortion of the waveform of the output. To keep the distortion as small as possible, the spectrum of the input signal must

be restricted within the frequency region $|\omega| \ll 1/T$. For this purpose low-pass filters are needed.

3.4.2 Low-pass filter

To prepare a band-limited pulse we introduce low-pass filters. The initial source is a rectangular pulse from a timer IC (integrated circuit). Because the rectangular pulse has high-frequency components, the negative delay circuit does not work properly. We must eliminate the high-frequency components with low-pass filters. As shown in Fig. 3.6, we introduce a two-stage low-pass filter. The transfer function of each filter is

$$H_{\text{LP}}(\omega) = \frac{\alpha}{1 - i\omega T_{\text{LP}}(3 - \alpha) - (\omega T_{\text{LP}})^2}, \quad (3.27)$$

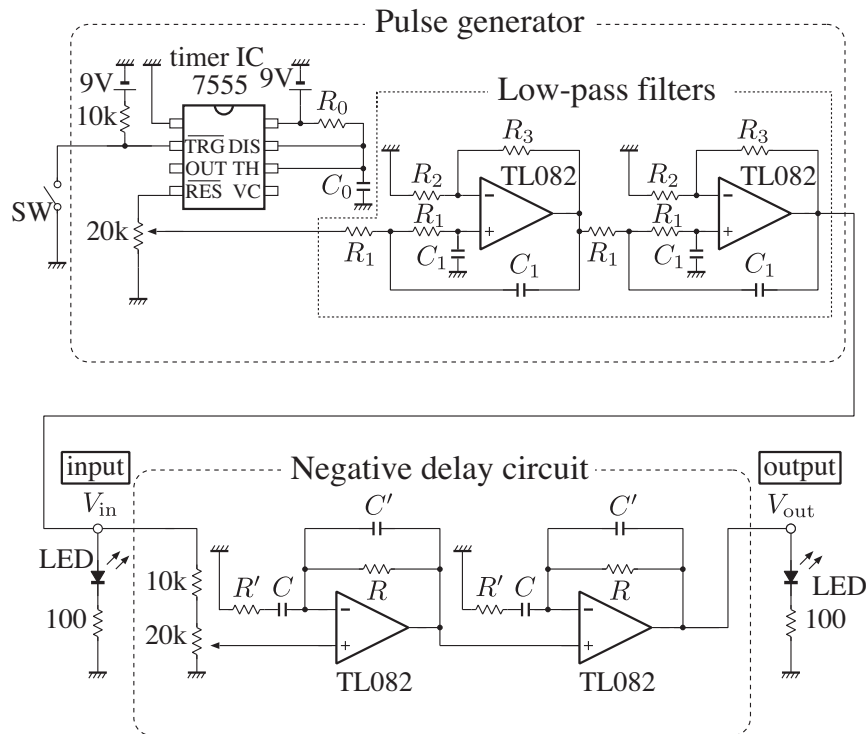


Figure 3.6: Overall circuits. Upper section: pulse generator. Lower section: negative delay circuit.

Table 3.1: Circuit parameters.

R_0	6.8 M Ω	R	1 M Ω
C_0	0.22 μ F	C	0.22 μ F
T_{rec}	1.5 s	R'	10 k Ω
R_1	2.2 M Ω	C'	22 nF
C_1	0.22 μ F	T	0.22 s
R_2	10 k Ω		
R_3	2.2 k Ω		
$\Delta\omega$	1.6 Hz		

where $T_{\text{LP}} = R_1 C_1$ and $\alpha = (1 + R_3/R_2)$. The order of the filter is given by the order of the denominator and the total order of the two-stage low-pass filter and is given by $m = 4$. By changing α , we can tailor the characteristics of the filter. In our experiment we choose $\alpha = 1.268$, which corresponds to a Bessel filter [53]. The Bessel filter is designed so that the overshoot for rectangular waves is small. The cut-off frequency is defined as $\Delta\omega = 0.7861/T_{\text{LP}}$.

3.4.3 Experiment

We show the overall circuit diagram for the negative delay experiment in Fig. 3.6 and the parameters in Table 3.1. The pulse generator in the upper section of Fig. 3.6 is subdivided into the generator of the single-shot rectangular wave and the low-pass filters. In the first part, when triggered by the switch, the timer IC generates a single pulse, whose width is determined by the time constant $T_{\text{rec}} = R_0 C_0 = 1.5$ s. The rectangular pulse is shaped by the two-stage low-pass filters. We take the cut-off frequency of the low-pass filter to be $\Delta\omega = 0.35/T$, so that $A(\omega)$ and $\phi(\omega)$ can be considered to be constant and linear, respectively, below the cut-off frequency (see Fig. 3.5). Finally, the band-limited single pulse is sent to the input of the negative delay circuit in the lower section of Fig. 3.6.

Two delay circuits shown in Fig. 3.4 are cascaded for larger advance times. The input and output terminals are monitored by LEDs. Their turn-on voltage is about

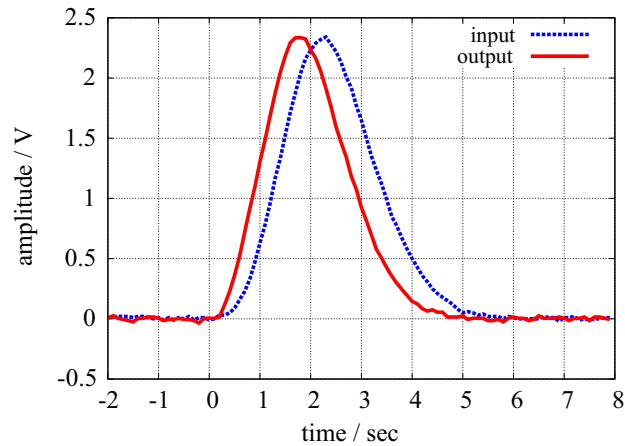


Figure 3.7: Experimental results. The oscilloscope traces show the input and output pulses. The output precedes the input owing to the negative delay.

1.1 V. The variable resistor at the input is adjusted so that the input and the output have the same height.

The experimental result is shown in Fig. 3.7. The input and output waveforms are acquired by an oscilloscope. The origin of the time ($t = 0$) is the moment when the switch in Fig. 3.6 is turned on. We see that the output precedes the input considerably (more than 20% of the pulse width). The slight distortion of the output waveform is caused by the non-ideal frequency dependence of $A(\omega)$ and $\phi(\omega)$, as mentioned in Sec. 3.4.1.

The expected negative delay derived from Eq. (3.26) is $2T = 0.44$ s; we have connected two circuits (each with time constant $T = 0.22$ s) in series for a larger effect. This delay quantitatively agrees with the experimental result, where the time difference between the output and the input peaks is about 0.5 s. The time scale is chosen so that we can directly observe the negative delay with two LEDs connected at the input and the output terminals. We also could use two voltmeters (or circuit testers) to monitor the waveforms, and we could dispense with an oscilloscope.

The actual negative delay circuit in Fig. 3.6 differs from that shown in Fig. 3.4. The resistor R' and the capacitor C' are added to suppress high-frequency noises. As shown in Fig. 3.5, the gain at $|\omega|T > 1$ is large. Although the high-frequency

components of the input signal are suppressed by the low-pass filters, internal and external noise with high frequency are unavoidable. With R' and C' , the high-frequency gain is limited. The parameters are chosen to satisfy $R'C, C'R \ll T$, so that the phase $\phi(\omega)$ for $|\omega|T < 1$ is not affected.

3.5 Realization of larger negative delay

The negative delay in the above experiment is about 20% of the pulse width. This delay is larger than the values obtained in other superluminal-velocity or negative-delay experiments. We now consider how to make even larger negative delays. We assume a noise-free environment for simplicity.

By cascading the negative delay circuits, the time advance can be increased. One might expect that, by increasing the number of stages n , the total time advance can be increased linearly with n . But, unfortunately, this is not the case. It is obvious from Eqs. (3.24) and (3.25) that the increase in n leads to the distortion of the waveform. When n circuits are connected in cascade, the total transfer function can be written as $H^n(\omega)$. Correspondingly, the amplitude and the phase are given as

$$A^n(\omega) \sim 1 + \frac{n(\omega T)^2}{2}, \quad (3.28)$$

$$n\phi(\omega) \sim n\omega T. \quad (3.29)$$

To keep the wave distortion below a certain level, we have to limit the excess gain $A^n(\omega) - 1$ within the bandwidth by some value γ ;

$$\frac{n(\omega T)^2}{2} \leq \frac{n(\Delta\omega T)^2}{2} = \gamma. \quad (3.30)$$

Then the advance time per circuit should satisfy

$$T = \sqrt{\frac{2\gamma}{n}} \Delta\omega^{-1} = \sqrt{\frac{2\gamma}{n}} T_w, \quad (3.31)$$

where T_w is the pulse width determined by the cut-off frequency of the low-pass filter.

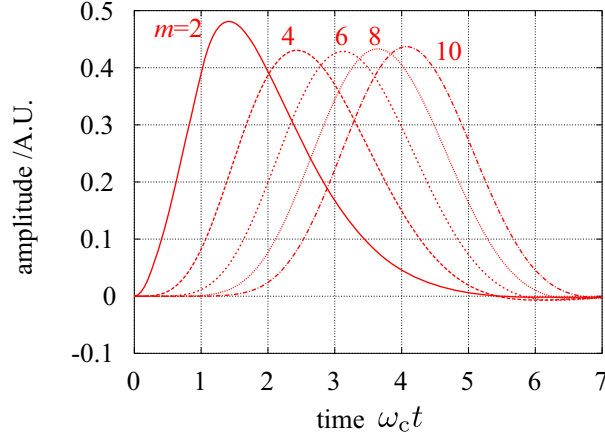


Figure 3.8: Responses of the Bessel filter to a rectangular wave. The orders of filters are $m = 2, 4, 6, 8,$ and 10 .

If we want to increase the time advance while conserving the pulse width and the shape of the signal, we must reduce the time advance T per circuit by the factor $1/\sqrt{n}$. Therefore, the total time advance T_{total} scales as

$$T_{\text{total}} = nT = \sqrt{2n\gamma} T_w, \quad (3.32)$$

which is a slowly increasing function of n .

In addition, there is another factor to be considered. It is impossible to advance the signal beyond the time when the switch is turned on in the rectangular pulse generator in Fig. 3.6. A causal transfer function cannot generate negative delays unconditionally. The reason for the advance is that the slow rising part of the pulse, which has been suppressed by the low-pass filter, is amplified by the negative delay circuit. The slowness of the rising part of the pulse is determined by the order m of the low-pass filter. Figure 3.8 represents the responses of various order Bessel filters with the same cut-off $\Delta\omega$ to a rectangular wave with a unit height and a pulse width $(\Delta\omega)^{-1}$. The pulse shapes, especially the widths of the pulses, are similar to each other due to the same cut-off frequency, but the higher the order of the filter, the more the rising part is delayed. Hence we need a high order filter to attain a large time advance. In other words, the pulse must be delayed appropriately in advance to obtain a large negative delay.

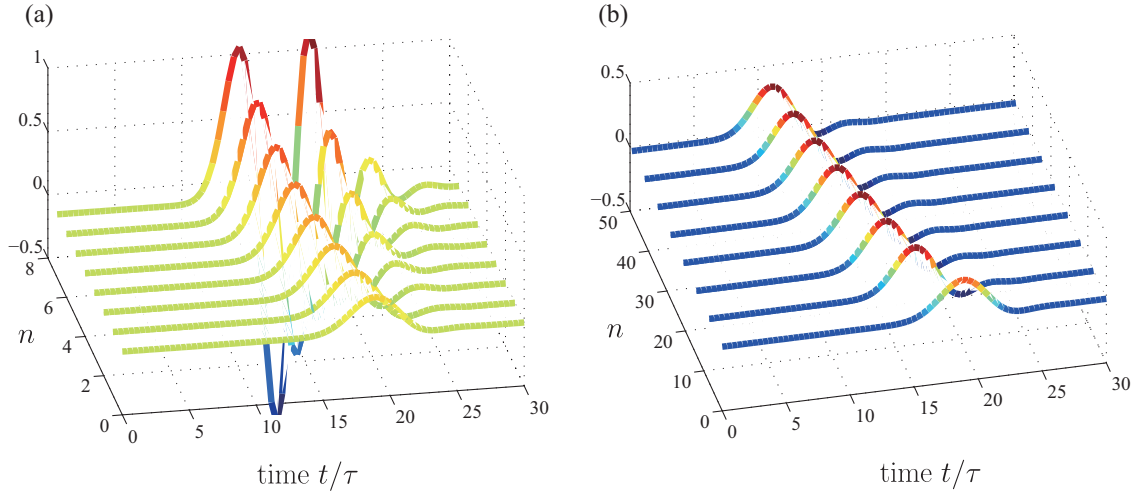


Figure 3.9: Cascading negative delay circuits. Time axis is normalized by the time constant τ . The negative delay per a circuit is given as (a) $T(= 1.155\tau)$ for $n = 0, 1, \dots, 7$ and (b) T/\sqrt{n} for $n = 0, 7, \dots, 49$.

Moreover, the short-time behavior of the total circuit including the low-pass filters and the negative delay circuits is determined by the composite transfer function at high frequency ($\omega \rightarrow \infty$). The order of the low-pass filter m should not be smaller than the number of the stages n of the negative delay circuits. Otherwise, the total transfer function would diverge at $\omega \rightarrow \infty$, and the derivative of the rectangular pulse would appear at the output.

In order to verify the above discussion, we prepare a heavily band-limited signal from a rectangular pulse with the width of τ by using five 10th-order Bessel filters with the cut-off frequency of $1/\tau$. In a simple cascading scheme with fixed negative delay T , which is assumed to $T = 1.155\tau$, the output signals for various n is obtained as shown in Fig. 3.9(a). It is confirmed that the increase in n causes severe distortions of pulse shapes. On the other hand, by applying scaling law given by Eq. (3.31), or adjusting the negative delay per a circuit to be T/\sqrt{n} , we can avoid the heavy distortions as shown in Fig. 3.9(b). It is also clear that the temporal advancement can be larger than the pulse width of the input pulse.

3.6 Summary and discussion

We have demonstrated negative group delays in a simple electronic circuit. A considerably large negative delay (0.44 s) can easily be achieved. It is slow enough to be seen with the naked eye using LEDs or voltmeters. The negative delay amounts to 20% of the pulse width. In the light experiment,[65] $t_d - L/c$ is 62 ns and is only a few percent of the pulse width, $4 \mu\text{s}$. This circuit model is useful for understanding the physics of superluminal propagation as well as negative group delays.

Here it should be noted that the group velocity has no direct connection with relativistic causality, and therefore it can exceed the speed of light c in a vacuum. The group velocity is defined just for band-limited signals and the input signals should be carefully prepared. On the other hand, the front velocity v_f (or the wavefront velocity) is constrained by causality and is equal to c , namely, $|v_f| = L/|t_f| = c$. This is the direct consequence of the fact that any media cannot respond to electromagnetic waves in the high frequency limit, i. e. $k(\omega) \rightarrow \omega/c$ ($\omega \rightarrow \infty$). In lumped systems ($L = 0$), the wavefront delay t_f must vanish. Actually all of the pulses in our system have their wavefronts at $t = 0$, the moment when the original rectangular pulse rises or the switch is turned on.

Chapter 4

Circuit simulation of slowing and storing light for baseband signal

In this chapter, we focus on extremely slow propagation of light and the storage of light, and we present a circuit model to simulate the phenomena for baseband signal. This circuit model is very clear and instructive, as in the case of superluminal propagation discussed in the previous chapter. We can set the time constant slow enough to observe the propagation as blinks of a series of light emitting diodes (LEDs) that monitor the output of each stage.

4.1 Slowing or storing light in atomic system

4.1.1 Control of group velocity with electromagnetically induced transparency

As described in the previous chapter, the group velocity crucially depends on the slope of the dispersion relations and subluminal group velocity $v_g < c$ is realized in normal-dispersion regions $\chi_1 > 0$. Extremely slow propagation can be realized in a highly dispersive medium $\chi_1 \gg 1$, and has been realized by utilizing electromagnetically induced transparency (EIT) [71]. In this chapter, we deal with EIT effects qualitatively, omitting rigorous description, which is provided in the next chapter. The EIT effects are induced in the medium composed of three-level atoms as shown

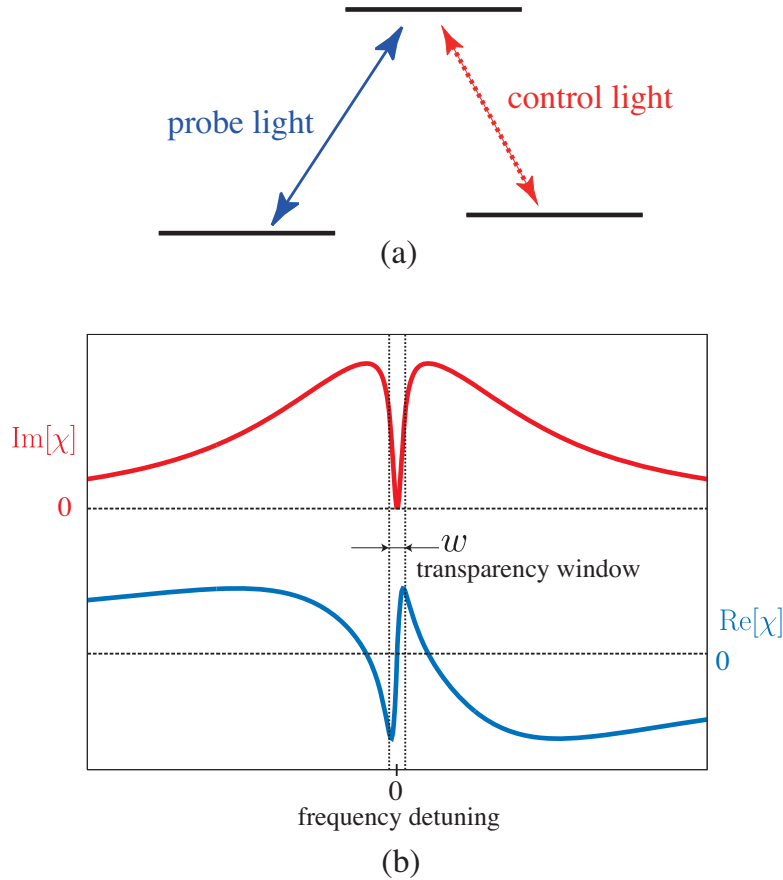


Figure 4.1: (a) Three-level system. (b) Electric susceptibility for the probe light in the presence of the control light.

in Fig. 4.1 (a). If a light called a probe light is tuned to an optical transition, it is absorbed in the medium. On the other hand, in the presence of another light called a control light, which is tuned to the other transition, the two light beams destructively interfere with each other through the common upper level, and the light absorption disappears. As shown in Fig. 4.1 (b), the real part of the electric susceptibility for the probe light, as well as the imaginary part, varies largely within a very narrow bandwidth called a “transparency window” where the absorption vanishes. As a result, the medium becomes highly dispersive $\chi_1 = d(\text{Re}[\chi])/d\omega \gg 1$, and the group velocity of the probe light becomes much smaller than c . Hau *et al.* successfully reduced group velocity to 17 m/s in a laser-cooled atomic gas [72].

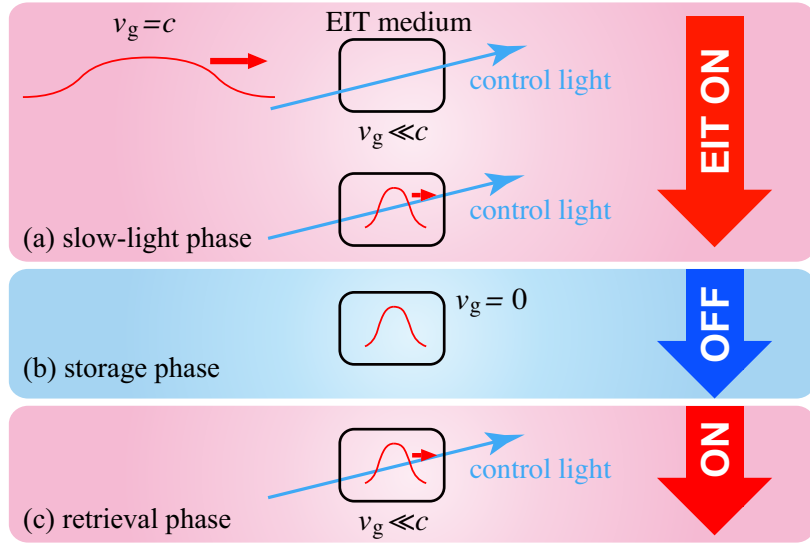


Figure 4.2: Procedures for light-pulse storage.

They prepared a single shot pulse with a duration of $2.5 \mu\text{s}$ and a pulse length of 750 m in a vacuum, and fed it into the EIT medium. Because it had been slowed down, the pulse length was compressed into $43 \mu\text{m}$ in the medium.

The group velocity is proportional to the width of the transparency window w , which is determined by the intensity of the control light: the weaker the control light, the smaller the group velocity. However, the pulse cannot be slowed down unconditionally. The lower limit of the group velocity is given by the condition that the transparency window must be wider than the bandwidth of the probe pulse. If not, the pulse shape will be deformed by the absorption. This situation is often called the EIT condition.

This limitation can be overcome and storage of light is possible by dynamically changing the intensity of the control light when the probe pulse is traveling in an EIT medium [73, 74]. Procedures for the storage of light in the EIT medium are shown in Fig. 4.2, which consists of three phases: (a) slow-light phase; (b) storage phase; and (c) retrieval phase. At the first phase, the intensity of the control light is kept constant and the incident pulse is spatially compressed into the medium as shown in Fig. 4.2(a). After the entire probe pulse fits into the EIT medium, the control light is gradually reduced, and the probe pulse is slowed down without

changing its spatial profile. The pulse is stored in the medium when the control light is eventually turned off as shown in Fig. 4.2(b). During this storage process, the spectral width of the probe pulse is compressed and fitted in the transparency window, which narrows according to the dimming of control light. The stored pulse can be restarted by restoring the control light as shown in Fig. 4.2(c). The released pulse is identical to the original one, because the freezing and releasing processes are carried out coherently. Such characteristics of light pulses as amplitude, phase, and beam profile can be stored. Even the quantum state of light can be stored in the medium, so this method is promising for quantum memory.

4.1.2 EIT condition

For EIT media, $\chi(\omega)$ changes sharply within the EIT window, whose width is w . The slope of χ is estimated as $\chi_1 = d\chi/d\omega \sim \alpha/w$, where α is the variation of χ in the window. Normally α corresponds to the optical thickness of the medium and can be of the order of unity. Assuming $n \sim 1$, we have an estimation

$$v_g \sim \frac{2w}{\omega_0}c, \quad (4.1)$$

for the group velocity (3.13). Roughly speaking, w is proportional to the square of Rabi frequency for the control light Ω_c , which is proportional to the amplitude of the control light. The width w can be effectively reduced to the atomic decoherence rate, which can be 100 kHz or even smaller. Therefore an extremely low velocity, $v_g \sim 10^{-9}c$, or virtual stopping, is possible.

The pulse spectrum must be contained within the EIT window. Namely, the spectral width $\Delta\omega$ of the envelope must satisfy the condition:

$$\Delta\omega < w. \quad (4.2)$$

This link between the group velocity and the bandwidth condition is a very important issue in slow light experiments. A similar restriction comes into play in the cases of superluminal or negative group velocities as described in the previous chapter [67, 68].

4.1.3 Change in spectral or spatial profile

If v_g is constant in time and space, it is easy to show that the solution of Eq. (3.12) is $f(t - x/v_g)$. This means that the envelope propagates in the medium at group velocity v_g , retaining its shape.

When v_g is a function of x , the solution of Eq. (3.12) can be written as

$$\mathcal{E}(t, x) = \phi \left(t - \int_0^x \frac{dx'}{v_g(x')} \right), \quad (4.3)$$

where $\mathcal{E}(t, 0) \equiv \phi(t)$ is the boundary condition at $x = 0$. The temporal profile of the pulse, or the spectrum, is conserved at any x , while the spatial profile shrinks (stretches) at small (large) $v_g(x)$, explaining why the pulse length is compressed when the light pulse is fed from the vacuum into the EIT medium.

Although the group velocity could be decreased further by reducing the width w of the transparency window, w must be wider than the bandwidth of the pulse, $\Delta\omega$, which is constant regardless of $v_g(x)$. Therefore, the spectral width $\Delta\omega$ of the initial pulse establishes the lower limit of the velocity.

On the other hand, when v_g is a function of t , the solution of Eq. (3.12) is given by

$$\mathcal{E}(t, x) = \psi \left(x - \int_0^t v_g(t') dt' \right), \quad (4.4)$$

where $\mathcal{E}(0, x) \equiv \psi(x)$ is the initial condition at $t = 0$. In this case, the spatial profile of the pulse is identical at any time t , but the temporal profile changes according to $v_g(t)$. When $v_g(t)$ decreases, the temporal profile, i.e. the pulse width, spreads out, compressing the frequency spectrum.

If the EIT condition is initially satisfied, it is fulfilled all the times no matter how much we diminish the velocity v_g or the transparency window w , because the spectral width $\Delta\omega$ is decreased accordingly. With this method, the stopping of light has been carried out.

4.2 Circuit model

4.2.1 All-pass filter

We will show how to simulate the pulse propagation described by Eq. (3.12) using an electronic circuit. First, we divide x into uniform steps as $x = n\Delta x$ (n is an integer). We discretize the second term of Eq. (3.12) as

$$v_g \frac{\partial \mathcal{E}}{\partial x} \rightarrow \frac{1}{T} \{v_{n+1}(t) - v_n(t)\}, \quad (4.5)$$

where $T \equiv \Delta x/v_g$ and $v_n(t) \equiv \mathcal{E}(n\Delta x, t)$. We approximate the first term of Eq. (3.12) as

$$\frac{\partial \mathcal{E}}{\partial t} \rightarrow \frac{d}{dt} \left\{ \frac{v_{n+1}(t) + v_n(t)}{2} \right\}. \quad (4.6)$$

Then the discretized version of Eq. (3.12) is obtained;

$$\frac{d}{dt} \left[\frac{v_{n+1}(t) + v_n(t)}{2} \right] + \frac{1}{T} [v_{n+1}(t) - v_n(t)] = 0. \quad (4.7)$$

After introducing the Fourier transform of $v_n(t)$,

$$V_n(\omega) = \int_{-\infty}^{\infty} v_n(t) e^{i\omega t} dt, \quad (4.8)$$

we have the difference equation

$$V_{n+1}(\omega) = H(\omega)V_n(\omega), \quad (4.9)$$

where

$$H(\omega) = \frac{1 + i\omega T/2}{1 - i\omega T/2} \quad (4.10)$$

is the transfer function.

The circuit illustrated in Fig. 4.3 has the transfer function given by Eq. (4.10). It is a well-known all-pass filter, which is used as a phase shifter [53]. The circuit provides a group delay T for signals whose spectrum is limited within the bandwidth $1/T$ [68]. Replacing the medium with length Δx by the circuit with $T = \Delta x/v_g$

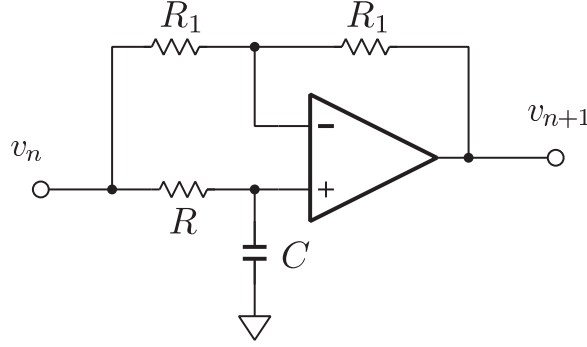


Figure 4.3: Elementary circuit for the simulation.

and cascading the circuits, we can simulate the envelope propagation described by Eq. (3.12).

The quantity $\nu_d \equiv 1/T$, which appears in Eq. (4.7), corresponds to the velocity v_g in Eq. (3.12). Even though the dimension of ν_d is different from that of velocities, hereafter we call it a “velocity.” It is the number of stages passed by the pulse per unit time.

4.2.2 Spectrum conditions

The above discretization is valid when envelope $\mathcal{E}(x, t)$ is smooth enough that the changes of $\mathcal{E}(x, t)$ over Δx can be ignored. From Eq. (4.7), the fractional change between $v_n(t)$ and $v_{n+1}(t)$ is estimated as

$$\left| \frac{v_{n+1}(t) - v_n(t)}{v_n(t)} \right| \simeq \frac{1}{\nu_d} \left| \frac{1}{v_n(t)} \frac{dv_n(t)}{dt} \right| < \frac{\Delta\omega}{\nu_d}, \quad (4.11)$$

where we have assumed that $v_n(t) \simeq v_{n+1}(t)$ and $\Delta\omega$ is the bandwidth of $v_n(t)$. If the condition

$$\Delta\omega/\nu_d = \Delta\omega \cdot T \ll 1 \quad (4.12)$$

is satisfied, the discretization is justified. This condition, $\Delta\omega \cdot T \ll 1$, coincides with the condition that each phase shifter works as an ideal group-delay circuit: $H(\omega) \sim \exp(i\omega T)$. Thus we have found that the spectrum of the input signals must be restricted within $\Delta\omega \ll \nu_d$, which corresponds to the EIT condition in the atomic system.

4.3 Experiment

4.3.1 Circuit parameters and input signal

The experimental setup is shown in Fig. 4.4, and the parameters of the delay circuit are shown in the inset. Forty delay circuits were cascaded. Each output is monitored with an LED. The delay time $T = 2RC$, or the speed $\nu_d = 1/T$, can be electronically changed with two analog switches (DG441) connected to the resistors. In Table 4.1 we show the relationship between the switch configurations and the constants (R , T , and ν_d).

The arbitrary waveform generator (Tektronix: AFG320) provides Gaussian pulses to the input of the delay circuits. The waveform is given by

$$v_0(t) = \begin{cases} 0 & (t < 0, \quad t > 5 \text{ s}), \\ V_0 e^{-4(t-t_s)^2/(\Delta\tau)^2} & (0 \leq t \leq 5 \text{ s}), \end{cases} \quad (4.13)$$

where $V_0 = 1.0 \text{ V}$, $t_s = 2.5 \text{ s}$, and $\Delta\tau = 1.0 \text{ s}$. The frequency spectrum of $v_0(t)$ is limited within $\Delta\omega \sim 4/\Delta\tau = 4.0 \text{ Hz}$.

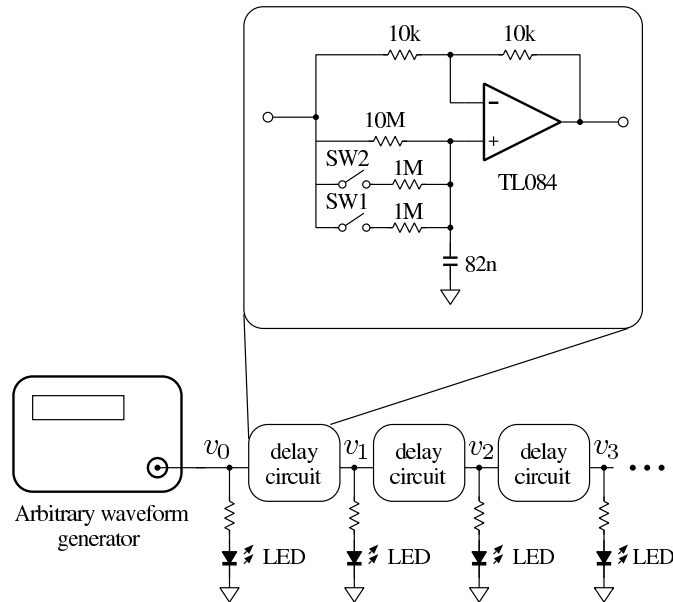
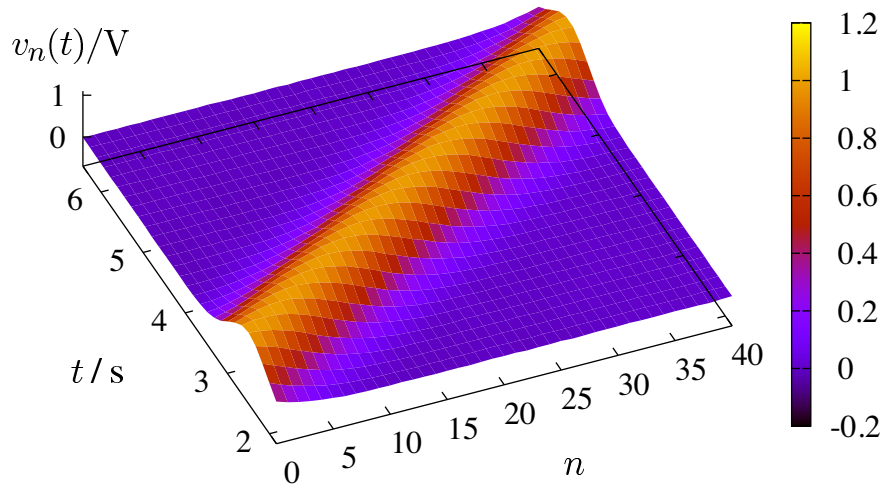


Figure 4.4: Schematic diagram of overall setup and circuit parameters.

Table 4.1: Switch configurations and parameters. $C = 82$ nF.

SW1	SW2	R	$T(= 2RC)$	$\nu_d(= 1/T)$
ON	ON	476 k Ω	0.078 s	13 /s
ON	OFF	909 k Ω	0.15 s	6.7 /s
OFF	OFF	10 M Ω	1.6 s	0.62 /s

Figure 4.5: Experimental result for wave propagation at constant speed $\nu_d = 13$ /s.

4.3.2 Constant speed propagation

Figure 4.5 shows the experimental result for $\nu_d = 13$ /s. The Gaussian-shaped pulse propagates at the speed of 13 circuits per second with its shape unchanged. In this case, the spectrum condition, Eq. (4.12), is satisfied as $\Delta\omega/\nu_d \sim 0.31 < 1$, which guarantees that the pulse travels with little distortion. The pulse length is estimated to be $\Delta n = \nu_d \Delta\tau \sim 13$.

4.3.3 Pulse length compression

In this section we consider a situation where the speed ν_d is dependent on the location n . We divide the cascaded circuits into two regions: $n < 25$ (Region I) and

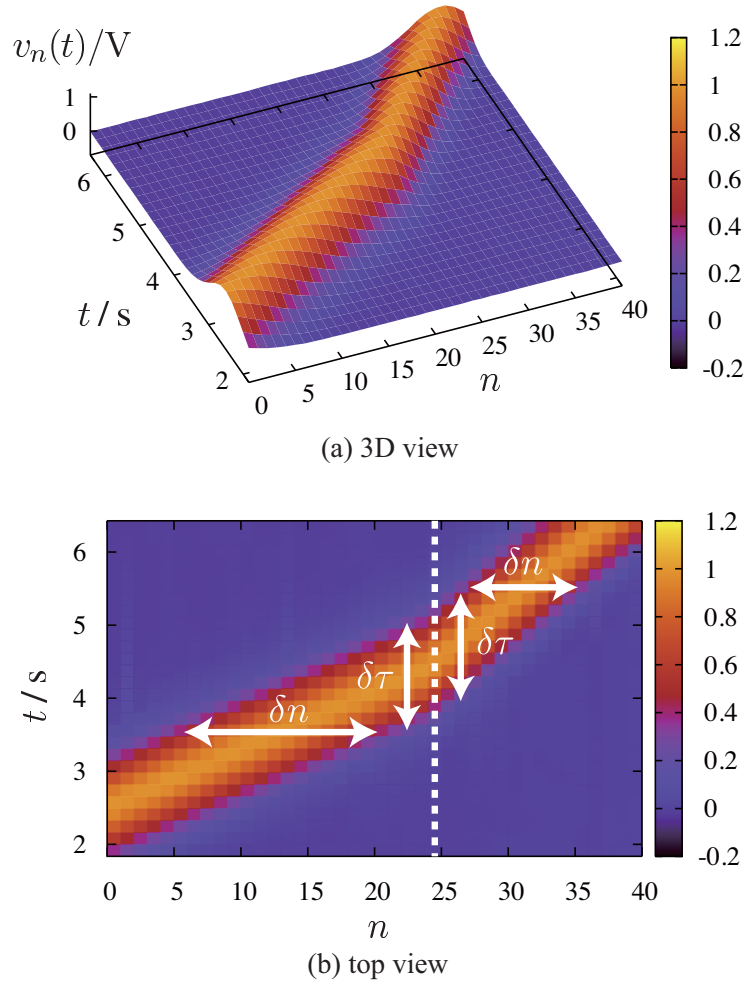


Figure 4.6: Pulse length compression. Pulse which runs at $v_1 = 13/s$ in $n < 25$, slows down to $v_2 = 6.7/s$ in $n \geq 25$.

$n \geq 25$ (Region II). The velocity in each region is set as

$$\nu_d(n) = \begin{cases} \nu_1 & (\text{Region I; } n < 25) \\ \nu_2 & (\text{Region II; } 25 \leq n) \end{cases}. \quad (4.14)$$

This case corresponds to the light propagation experiment in which the pulse is fed from a vacuum (Region I) into the EIT medium (Region II).

Figure 4.6 shows the results when $\nu_1 = 13/s$ and $\nu_2 = 6.7/s (\sim \nu_1/2)$. At the boundary $n = 25$, the speed of the pulse propagation is almost cut in half. Note

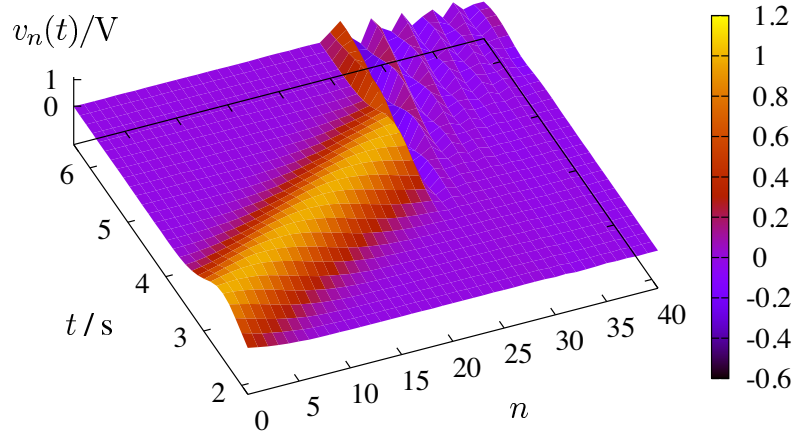


Figure 4.7: Experimental result for $v_1 = 13/s$ in $n < 25$ and $v_2 = 0.62/s$ in $n \geq 25$. The pulse is collapsed in $n \geq 25$, because the spectrum condition is violated.

that the pulse has to be continuously connected at the boundary, which is marked by the dashed line, because the output of the 24th circuit is connected to the input of the 25th circuit. Hence the pulse width $\Delta\tau$ in time domain remains unchanged for any location n , and the spectral width $\Delta\omega$ is also invariable. In the present case, for both of the regions, the spectrum conditions are satisfied as $\Delta\omega/\nu_1 = 0.31 < 1$ and $\Delta\omega/\nu_2 = 0.60 < 1$, and the Gaussian shape is almost maintained through the propagation. On the other hand, the pulse length Δn in Region II is compressed into about half the length: $\Delta n_1 = \nu_1 \Delta\tau \sim 13$ in Region I and $\Delta n_2 = \nu_2 \Delta\tau \sim 6.7$ in Region II. This is because, after the leading part of the pulse reaches the boundary, the rear part travels faster in Region I than the leading part runs in Region II. As mentioned before, the same pulse compression occurs when the light pulse prepared in the vacuum is fed into the EIT medium.

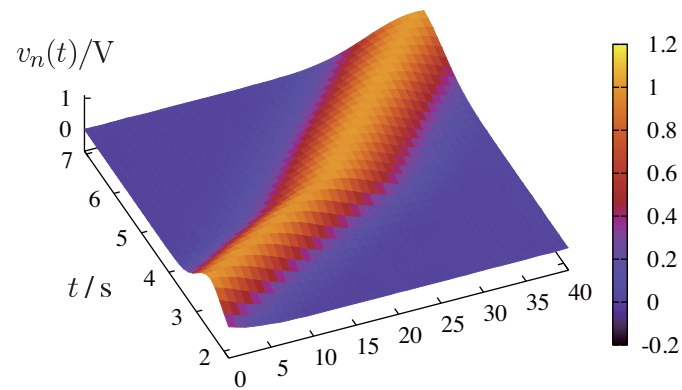
Next we used the parameters $\nu_1 = 13/s$ and $\nu_2 = 0.62/s$ ($\sim \nu_1/20$). One might assume that the pulse will be slowed by $1/20$ and compressed spatially by $1/20$. But we obtained the results shown in Fig. 4.7. The shape of the pulse collapses completely in Region II, because the spectrum condition is violated in Region II ($\Delta\omega/\nu_2 = 6.4 > 1$). The spectrum condition sets the lower speed limit: $\Delta\omega = 4.0/s$.

In experiments with slow light by means of EIT, similar spectrum conditions exist. If the spectrum of the light pulse is wider than the transparency window of

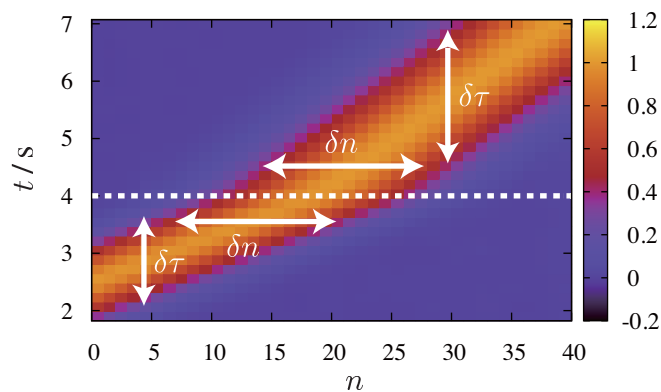
the EIT medium, the pulse shape is strongly modified due to the absorption.

4.3.4 Pulse storage

Here we deal with cases where the speed v_a is a function of time. For simplicity, we divide the time interval into three periods, and in each period the velocity is



(a) 3D view



(b) top view

Figure 4.8: Changing the speed v_g in time. Pulse which initially travels at $v_1 = 13/s$ slows down to $v_2 = 6.7/s$

kept constant:

$$\nu_d(t) = \begin{cases} \nu_1 & (\text{Period I; } t < 4 \text{ s}) \\ \nu_2 & (\text{Period II; } 4 \text{ s} \leq t < 7 \text{ s}) \\ \nu_3 & (\text{Period III; } 7 \text{ s} \leq t) \end{cases}. \quad (4.15)$$

First we consider the case $\nu_1 = 13$ /s and $\nu_2 = \nu_3 = 6.7$ /s. The results are shown in Fig. 4.8. At the end of Period I ($t = 4$ s), most of the pulse has entered the circuits. It is then instantaneously slowed down from the leading edge to the rear edge. In this case, the boundary condition that assures the continuity of the wave at $t = 4$ s is imposed. As a result, the pulse length Δn is unchanged, while the pulse width in time domain, $\Delta\tau$, doubles after the switching. In other words, the frequency spectrum is compressed into half, and $\Delta\omega$ is halved. This means that $\Delta\omega/\nu_d$ remained constant ($= 0.31$). Spectral change is one of the typical phenomena in time-varying systems. This situation corresponds to a case where we change the group velocity while the entire pulse is in the EIT medium ($0 < n \leq 40$).

The violation of the spectrum condition, as discussed in the previous section, can be avoided by the strategy of changing ν_d in time. It is possible to attain much slower propagation, or even to stop the pulse. We modified the time sequence so that $\nu_1 = 13$ /s, $\nu_2 = 0.62$ /s, and $\nu_3 = 13$ /s. The results are shown in Fig. 4.9. In Period II, the propagation of the pulse is almost frozen. The pulse is released at $t = 7$ s. As mentioned above, the spectrum conditions are always satisfied because $\Delta\omega/\nu_d$ is conserved in any time. Hence the pulse can propagate or be frozen without changing its shape in a time-varying system.

In the EIT case, the change in group velocity is attributed to a dark-state polariton, which is a coupled mode of the electric field and the atomic coherence [74, 75]. The velocity of the polariton is determined by the mixing ratio, which depends on the control light intensity. The atom-like polariton runs slower, and the purely atomic polariton stays still. The pulse shape is imprinted in the spatial distribution of atomic coherence, and the storage time is limited by the relaxation time of the atomic coherence. In the circuit model, by adding a resistor R' in parallel with each capacitor we can simulate the effect of decoherence. In the stopping stage, the voltage of each capacitor decays exponentially due to the discharge through the

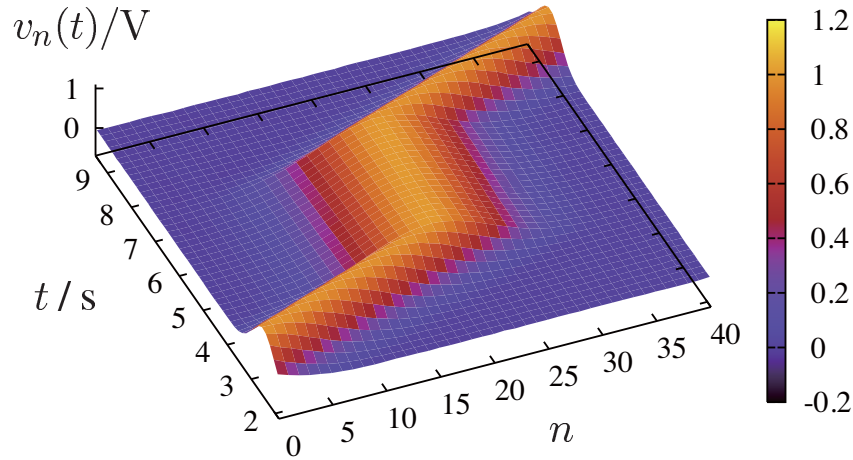


Figure 4.9: Pulse freezing.

parallel resistor. The storage time is limited by the time constant $R'C$, which corresponds to the decoherence time in an EIT experiment.

4.4 Summary

We have introduced the electronic circuit that simulates slow light and stopped light. Most of the properties in the simulation are analogous to the light propagation in the EIT medium. However the mechanism of the velocity control is much simpler in the case of the circuit simulation: without knowing the details of EIT and dark-state polaritons, we can understand the physics of slow light and frozen light. In addition, simulations with circuits has an advantage because the parameters can be changed easily. We illustrate three cases: constant v_g , position-dependent velocities $v_g(x)$, and time-varying velocities $v_g(t)$. It would be interesting to consider a general case where velocity is a function of space and time, $v_g(x, t)$ (for example Ref. [76]). For cases where implementation with EIT methods is difficult, the circuit model may be feasible.

The present model deals with envelopes and can only describe one-way wave propagations. It cannot be used to reproduce such bidirectional phenomena as reflections and interference, where forward and backward waves must both be con-

sidered. But it does reproduce one of the most fundamental properties of waves: a disturbance propagates at a certain velocity, retaining its shape through a medium.

Chapter 5

Artificial atoms interacting with electromagnetic fields

In Chap. 2, we have shown the circuit models for closed quantum systems. The interaction among the quantum states is included, and total energy, which corresponds to the total population of quantum states, is always conserved. On the other hand, in quantum systems with open channels, the total population of relevant states is not necessarily conserved. The population transfer is often induced by external fields, and the field energy is absorbed or amplified. In this chapter, we introduce circuit analogies and metamaterial analogies to such open quantum systems including an atomic EIT system.

5.1 Classical model of two-level system interacting with external fields

5.1.1 Linear response of two-level atoms

The simplest example of quantum system interacting with open space is a two-level system interacting with external fields, such as atomic excitation by oscillating electric or magnetic field, spin precession by static magnetic field, and so on. In this section, we consider atomic transition between two levels by electric fields

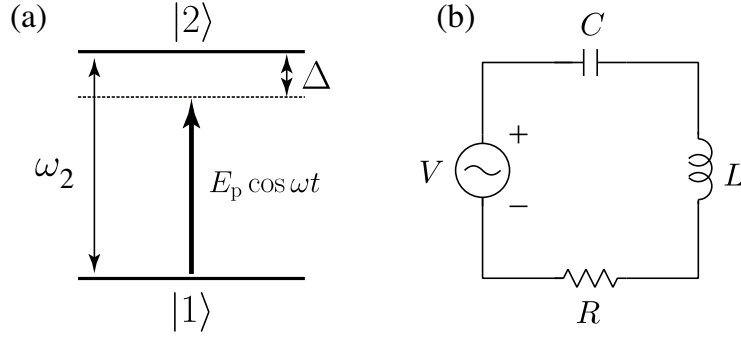


Figure 5.1: (a) Two-level system interacting with oscillating fields. (b) Circuit model.

$E = E_p \cos \omega t$ as shown in Fig. 5.1 (a). We suppose that a ground state $|1\rangle$ and an excited $|2\rangle$ state are connected with an electric dipole moment, whose operator is defined as $\hat{p}_p = p_p|2\rangle\langle 1| + \text{H.c.}$ Assuming the origin of the energy is at the ground level $|1\rangle$ for simplicity, we can write the Hamiltonian of the system as

$$\hat{H} = -\hat{p}_p E_p \cos \omega t + \hbar \omega_2 |2\rangle\langle 2|, \quad (5.1)$$

where $E_p \cos \omega t$ is the electric field and ω_2 is the transition frequency. For near-resonance case, where the detuning $\Delta \equiv \omega_2 - \omega$ is less than the linewidth γ_2 , rotating-wave approximation can be applied, and we obtain

$$\hat{H} = -\frac{\hbar \Omega_p}{2} e^{-i\omega t} |2\rangle\langle 1| - \frac{\hbar \Omega_p^*}{2} e^{i\omega t} |1\rangle\langle 2| + \hbar \omega_2 |2\rangle\langle 2|, \quad (5.2)$$

with $\Omega_p \equiv p_p E_p / \hbar$, which is called Rabi frequency [69]. If the state is given by $|\psi\rangle = C_1(t)|1\rangle + C_2(t)|2\rangle$, the Schrödinger equation yields

$$\frac{d}{dt} \begin{pmatrix} C_1 \\ C_2 \end{pmatrix} = -i \begin{pmatrix} 0 & -\frac{\Omega_p^*}{2} e^{i\omega t} \\ -\frac{\Omega_p}{2} e^{-i\omega t} & \omega_2 \end{pmatrix} \begin{pmatrix} C_1 \\ C_2 \end{pmatrix}. \quad (5.3)$$

The effect of the decay at $|2\rangle$ can be phenomenologically introduced as follows:

$$\frac{d}{dt} \begin{pmatrix} C_1 \\ C_2 \end{pmatrix} = -i \begin{pmatrix} 0 & -\frac{\Omega_p^*}{2} e^{i\omega t} \\ -\frac{\Omega_p}{2} e^{-i\omega t} & \omega_2 - i\frac{\gamma_2}{2} \end{pmatrix} \begin{pmatrix} C_1 \\ C_2 \end{pmatrix}. \quad (5.4)$$

Weak-field approximation If the field is weak enough to satisfy $\Omega_p \ll \gamma_2$, it is fairly assumed that only the ground state $|1\rangle$ is occupied, i. e. $C_1(t) = 1$.* Under this condition, Eq. (5.4) is reduced to

$$\frac{dC_2}{dt} = -\left(i\omega_2 + \frac{\gamma_2}{2}\right) C_2 + i\frac{\Omega_p}{2} e^{-i\omega t}. \quad (5.5)$$

In a rotating frame defined as $\tilde{C}_2 = e^{i\omega t} C_2$, the above relation can be written as

$$\frac{d\tilde{C}_2}{dt} = -\left(i\Delta + \frac{\gamma_2}{2}\right) \tilde{C}_2 + i\frac{\Omega_p}{2}, \quad (5.6)$$

where $\Delta = \omega_2 - \omega$. The steady-state solution can be easily derived from $d\tilde{C}_2/dt = 0$ as

$$\tilde{C}_2(t) = \frac{i\Omega_p}{2} \frac{1}{i\Delta + \frac{\gamma_2}{2}}, \quad C_2(t) = \frac{i\Omega_p}{2} \frac{1}{i\Delta + \frac{\gamma_2}{2}} e^{-i\omega t}. \quad (5.7)$$

Susceptibility of atomic media The electric dipole moment per an atom is given by

$$\begin{aligned} p_0 &\equiv \langle \psi | \hat{p}_p | \psi \rangle = p_p^* C_1^*(t) C_2(t) + \text{c.c.} \\ &= \tilde{p}_p e^{-i\omega t} + \text{c.c.} \end{aligned} \quad (5.8)$$

where

$$\tilde{p}_p \equiv \frac{i|p_p|^2}{2\hbar} \frac{E_p}{i\Delta + \frac{\gamma_2}{2}}. \quad (5.9)$$

If the medium is composed of the two-level atoms with the density of N , the total electric polarization is $p_p N$. The complex susceptibility χ is obtained from $\tilde{p}_p N = \epsilon_0 \chi E_p$, and the real part χ' and imaginary part χ'' are derived from Eq. (5.7) as

$$\chi' = \text{Re} \left[\frac{i|p_p|^2 N}{2\epsilon_0 \hbar} \frac{1}{i\Delta + \frac{\gamma_2}{2}} \right] = \frac{|p_p|^2 N}{2\epsilon_0 \hbar} \frac{\Delta}{\Delta^2 + \left(\frac{\gamma_2}{2}\right)^2}, \quad (5.10)$$

$$\chi'' = \text{Im} \left[\frac{i|p_p|^2 N}{2\epsilon_0 \hbar} \frac{1}{i\Delta + \frac{\gamma_2}{2}} \right] = \frac{|p_p|^2 N}{2\epsilon_0 \hbar} \frac{\frac{\gamma_2}{2}}{\Delta^2 + \left(\frac{\gamma_2}{2}\right)^2}, \quad (5.11)$$

*Phase factor can be ignored because the origin of the energy level is at $|1\rangle$.

respectively. The dispersive profiles of χ' and χ'' have been shown in Fig. 3.1 (a), and the absorption spectrum related with χ'' shows a Lorentzian profile with the width of γ_2 . During the derivation, we have assumed weak-field approximation $\Omega_p \ll \gamma_2$, ignoring saturation effects. Therefore the derived susceptibilities represent the linear response of the medium.

5.1.2 Circuit analogy of two-level system interacting with external fields

The differential equation (5.5) can be regarded as the equation of motions for a harmonic oscillator with the resonant frequency ω_2 driven by external force rotating at ω . The circuit analogy can be an LC resonator driven by an external voltage source as shown in Fig. 5.1(b). The evolution of the LC resonator is governed by

$$L \frac{d^2 i}{dt^2} + R \frac{di}{dt} + \frac{i}{C} = \frac{d}{dt}(\tilde{v} \cos \omega t). \quad (5.12)$$

If the amplitude \tilde{v} of the external voltage source changes slowly enough to satisfy $|d\tilde{v}/dt| < \omega$, the current envelope \tilde{i} , which is defined through $i = \tilde{i} e^{-i\omega t} + \text{c.c.}$, also varies slowly. In terms of \tilde{i} and \tilde{v} , the first and second terms in the left-hand side of Eq. (5.12) and the term in the right-hand side of Eq. (5.12) are rewritten as

$$L \frac{d^2 i}{dt^2} = L \frac{d^2 \tilde{i}}{dt^2} e^{-i\omega t} - 2i\omega L \frac{d\tilde{i}}{dt} e^{-i\omega t} - \omega^2 L \tilde{i} e^{-i\omega t} + \text{c.c.}, \quad (5.13)$$

$$R \frac{di}{dt} = R \frac{d\tilde{i}}{dt} e^{-i\omega t} - i\omega R \tilde{i} e^{-i\omega t} + \text{c.c.}, \quad (5.14)$$

$$\frac{d}{dt}(\tilde{v} \cos \omega t) = \frac{d\tilde{v}}{dt} e^{-i\omega t} - i\omega \tilde{v} e^{-i\omega t} + \text{c.c.} \quad (5.15)$$

By applying slow varying envelope approximation, we can ignore the first terms in each of Eqs. (5.13), (5.14), and (5.15). Then, for the factors with $e^{-i\omega t}$, Eq. (5.12) is reduced to

$$\frac{d\tilde{i}}{dt} + \frac{i(\omega_2^2 - \omega^2)}{2\omega} \tilde{i} + \frac{R}{2L} \tilde{i} = \frac{\tilde{v}}{2L}. \quad (5.16)$$

For near-resonance condition, $\omega_2 + \omega \sim 2\omega$ can be used for the second term, and we obtain

$$\frac{d\tilde{i}}{dt} = - \left(i\Delta + \frac{R}{2L} \right) \tilde{i} + \frac{\tilde{v}}{2L}, \quad (5.17)$$

Table 5.1: Correspondence between two-level system in driving field and LC resonator driven by external voltage source.

Driven two-level system	Driven LC resonator
transition frequency : ω_2	resonant frequency : $1/\sqrt{LC}$
external field : $E_p \cos \omega t$	external voltage source : $\tilde{v} \cos \omega t$
population for $ 2\rangle$: C_2 (coherence between $ 1\rangle$ and $ 2\rangle$)	current in the resonator : i
decay rate for $ 2\rangle$: γ_2	dissipation rate : R/L
absorption : $\text{Im}[\chi]$	dissipated power : $\text{Re}[P_c]$

where we use the same definition $\Delta = \omega_2 - \omega$ as introduced in the previous section. Comparing Eqs. (5.6) and (5.17), we can find that the LC resonator is described by the same differential equation as the quantum two-level system, by assuming $\gamma_2 = R/L$ and $\Omega_p = -i\tilde{v}/L$. The current in steady state can be easily obtained as

$$\tilde{i} = \frac{1}{i\Delta + \frac{\gamma_2}{2}} \frac{\tilde{v}}{2L}. \quad (5.18)$$

Here, we introduce a complex power, which is given by

$$P_c = \tilde{v}^* \tilde{i} = \frac{|\tilde{v}|^2}{2L} \frac{1}{i\Delta + \frac{\gamma_2}{2}}. \quad (5.19)$$

The real part and imaginary part of P_c is

$$P_r \equiv \text{Re}[P_c] = \frac{|\tilde{v}|^2}{2L} \frac{\frac{\gamma_2}{2}}{\Delta^2 + \left(\frac{\gamma_2}{2}\right)^2}, \quad P_i \equiv \text{Im}[P_c] = -\frac{|\tilde{v}|^2}{2L} \frac{\Delta}{\Delta^2 + \left(\frac{\gamma_2}{2}\right)^2}. \quad (5.20)$$

The real (imaginary) part of P_c corresponds to the imaginary (real) part of the complex susceptibility. It is natural because the real part of P_c represents the energy dissipation in the resistor and shows a Lorentzian profile with the width of $\gamma_2 = R/L$.

The correspondences between the quantum system for driven two-level atoms and its circuit model are summarized in Table 5.1.

5.1.3 Metamaterial analogy of two-level system

The constituents of the metamaterial that resonates at a specific frequency can be regarded as artificial atoms (meta-atoms) analogous to the two-level atoms, because the circuit models of the meta-atoms are well described by LC resonators. There are various kinds of resonant meta-atoms, such as dipole resonators, cut-wire structures, and split ring resonators as shown in Figs. 5.2 (a)(b)(c), respectively. Here, we take a cut-wire structure as a typical example of metamaterials with electric dipole oscillation. As shown in Fig. 5.2 (d), the metallic parts and the gaps between the cut-wires can be regarded as inductors and capacitors, respectively. In the presence of electric field E aligned along the cut-wire structure, electric charges $\pm q$ accumulated at both ends of the bar structure form an electric dipole $p = qd$, where d represents the effective dipole length determined by the charge distribution. For oscillating field with the complex amplitude \tilde{E} , the same relation can be assumed as $\tilde{p} = \tilde{q}d$, where \tilde{p} and \tilde{q} are the complex amplitude of the electric dipole and the charges, respectively. From $i = dq/dt$, the complex amplitude of the current, \tilde{i} , is represented as

$$\tilde{i} = -i\omega\tilde{q}. \quad (5.21)$$

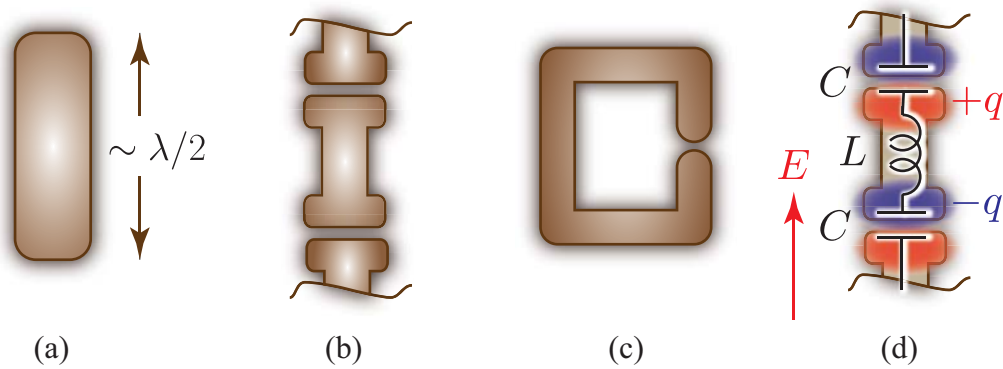


Figure 5.2: Various meta-atoms (a) Dipole resonator. (b) Cut-wire structure. (c) Split ring resonator. (d) Circuit model for cut-wire structure.

The voltage applied to each unit cell with the length of l can be roughly estimated as $\tilde{v} = \tilde{E}l$. Hence, Eq. (5.18) gives

$$\tilde{p} = i \frac{ld}{2\omega L} \frac{1}{i\Delta + \frac{\gamma_2}{2}} \tilde{E}. \quad (5.22)$$

For the meta-atom density of N , we can obtain the electric susceptibility of the metamaterial as follows:

$$\chi = \frac{\tilde{p}N}{\epsilon_0 \tilde{E}} = i \frac{ldN}{2\epsilon_0 \omega L} \frac{1}{i\Delta + \frac{\gamma_2}{2}}. \quad (5.23)$$

The susceptibilities of two-level atoms and the metamaterial are the same except the coefficients, and it is plausible to identify the metamaterial composed of artificial atoms like cut-wires with the medium composed of two-level atoms.

5.2 Classical model of EIT

5.2.1 EIT effect with three-level atoms

In this section, we consider EIT effects in three-level atoms with two ground states, $|1\rangle$ and $|3\rangle$, and a common excited state $|2\rangle$ as shown in Fig. 5.3. The dipole moment for $|1\rangle \rightarrow |2\rangle$ and $|3\rangle \rightarrow |2\rangle$ are defined as $\hat{p}_p = p_p|2\rangle\langle 1| + \text{H.c.}$ and $\hat{p}_c = p_c|2\rangle\langle 3| + \text{H.c.}$, respectively. We suppose that a probe field, $E_p \cos \omega t$, induces the transition from $|1\rangle$ to $|2\rangle$ with a detuning $\Delta (= \omega_2 - \omega)$, and the other field $E_c \cos \omega_c t$, called control field, connects the transition between $|3\rangle$ and $|2\rangle$ with no detuning, $\omega_c = \omega_2 - \omega_3$. The Hamiltonian of the system is given by

$$\hat{H} = -\hat{p}_p E_p \cos \omega t - \hat{p}_c E_c \cos \omega_c t + \hbar \omega_2 |2\rangle\langle 2| + \hbar \omega_3 |3\rangle\langle 3|. \quad (5.24)$$

For near-resonance case, rotating-wave approximation can be applied, and we obtain

$$\begin{aligned} \hat{H} = & -\frac{\hbar \Omega_p}{2} e^{-i\omega t} |2\rangle\langle 1| - \frac{\hbar \Omega_p^*}{2} e^{i\omega t} |1\rangle\langle 2| - \frac{\hbar \Omega_c}{2} e^{-i\omega_c t} |2\rangle\langle 3| - \frac{\hbar \Omega_c^*}{2} e^{i\omega_c t} |3\rangle\langle 2| \\ & + \hbar \omega_2 |2\rangle\langle 2| + \hbar \omega_3 |3\rangle\langle 3|, \end{aligned} \quad (5.25)$$

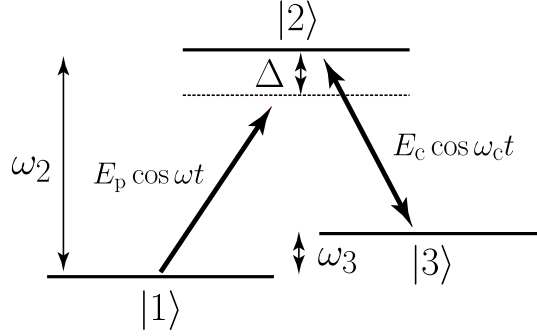


Figure 5.3: Three-level system interacting with probe and control light.

where Rabi frequencies are defined as $\Omega_p \equiv p_p E_p / \hbar$ and $\Omega_c \equiv p_c E_c / \hbar$. If the state is given by $|\psi\rangle = C_1(t)|1\rangle + C_2(t)|2\rangle + C_3(t)|3\rangle$, the Schrödinger equation yields

$$\frac{d}{dt} \begin{pmatrix} C_1 \\ C_2 \\ C_3 \end{pmatrix} = -i \begin{pmatrix} 0 & -\frac{\Omega_p^*}{2} e^{i\omega t} & 0 \\ -\frac{\Omega_p}{2} e^{-i\omega t} & \omega_2 & -\frac{\Omega_c}{2} e^{-i\omega_c t} \\ 0 & -\frac{\Omega_c^*}{2} e^{i\omega_c t} & \omega_3 \end{pmatrix} \begin{pmatrix} C_1 \\ C_2 \\ C_3 \end{pmatrix}. \quad (5.26)$$

The effects of the decay at $|2\rangle$ and $|3\rangle$ can be phenomenologically introduced as follows:

$$\frac{d}{dt} \begin{pmatrix} C_1 \\ C_2 \\ C_3 \end{pmatrix} = -i \begin{pmatrix} 0 & -\frac{\Omega_p^*}{2} e^{i\omega t} & 0 \\ -\frac{\Omega_p}{2} e^{-i\omega t} & \omega_2 - i\frac{\gamma_2}{2} & -\frac{\Omega_c}{2} e^{-i\omega_c t} \\ 0 & -\frac{\Omega_c^*}{2} e^{i\omega_c t} & \omega_3 - i\frac{\gamma_3}{2} \end{pmatrix} \begin{pmatrix} C_1 \\ C_2 \\ C_3 \end{pmatrix}. \quad (5.27)$$

We can suppose that the decay rate at the excited state $|2\rangle$ is much larger than that at the ground state $|3\rangle$, i.e. $\gamma_2 \gg \gamma_3$.

Weak-field approximation If the probe field is weak enough to satisfy $\Omega_p \ll \gamma_2$, Ω_c , we can assume $C_1(t) = 1$. Under this condition, Eq. (5.27) becomes

$$\frac{d}{dt} \begin{pmatrix} C_2 \\ C_3 \end{pmatrix} = - \begin{pmatrix} i\omega_2 + \frac{\gamma_2}{2} & -i\frac{\Omega_c}{2} e^{-i\omega_c t} \\ -i\frac{\Omega_c^*}{2} e^{i\omega_c t} & i\omega_3 + \frac{\gamma_3}{2} \end{pmatrix} \begin{pmatrix} C_2 \\ C_3 \end{pmatrix} + \frac{i}{2} \begin{pmatrix} \Omega_p e^{-i\omega t} \\ 0 \end{pmatrix}. \quad (5.28)$$

In a rotating frame defined as $\tilde{C}_2 = e^{i\omega t} C_2$ and $\tilde{C}_3 = e^{i\omega t} e^{-i\omega_c t} C_3$, the above relation can be written as

$$\frac{d}{dt} \begin{pmatrix} \tilde{C}_2 \\ \tilde{C}_3 \end{pmatrix} = - \begin{pmatrix} i\Delta + \frac{\gamma_2}{2} & -i\frac{\Omega_c}{2} \\ -i\frac{\Omega_c}{2} & i\Delta + \frac{\gamma_3}{2} \end{pmatrix} \begin{pmatrix} \tilde{C}_2 \\ \tilde{C}_3 \end{pmatrix} + \frac{i}{2} \begin{pmatrix} \Omega_p \\ 0 \end{pmatrix}. \quad (5.29)$$

The steady-state solution can be easily derived from $d\tilde{C}_2/dt = d\tilde{C}_3/dt = 0$ as

$$\tilde{C}_2 = \frac{i\Omega_p}{2} \frac{i\Delta + \frac{\gamma_3}{2}}{\left(i\Delta + \frac{\gamma_2}{2}\right) \left(i\Delta + \frac{\gamma_3}{2}\right) + \left|\frac{\Omega_c}{2}\right|^2}. \quad (5.30)$$

Susceptibility of EIT media As the same in Sec. 5.1.1, the complex susceptibility for the probe light is derived as

$$\chi = \frac{i|p_p|^2 N}{2\epsilon_0 \hbar} \frac{i\Delta + \frac{\gamma_3}{2}}{\left(i\Delta + \frac{\gamma_2}{2}\right) \left(i\Delta + \frac{\gamma_3}{2}\right) + \left|\frac{\Omega_c}{2}\right|^2}. \quad (5.31)$$

5.2.2 Circuit analogy of EIT effects

In 2002, Alzar *et al.* proposed a method to mimic EIT effects using coupled harmonic oscillators [77]. In this section, we deal with weakly coupled *LC* resonators with the resonant frequency of $\omega_2 = 1/\sqrt{LC}$ as shown in Figs. 5.4 (a) or (b), which represent a magnetically-coupled resonator and an electrically-coupled resonator, respectively. For the time being, we consider the magnetically coupled resonator, which is almost the same as the electrically-coupled resonator. We suppose that the resonator directly driven by the external voltage oscillating at ω has a low quality (low-Q) factor while the other has a high quality (high-Q) factor, i.e. $R \gg r$. The circuit equation is given by

$$L \frac{d^2 i_1}{dt^2} + R \frac{d i_1}{dt} + \frac{i_1}{C} + M \frac{d^2 i_2}{dt^2} = \frac{d}{dt} (\tilde{v} \cos \omega t), \quad (5.32)$$

$$L \frac{d^2 i_2}{dt^2} + r \frac{d i_2}{dt} + \frac{i_2}{C} + M \frac{d^2 i_1}{dt^2} = 0, \quad (5.33)$$

where i_1 and i_2 are currents in the low-Q resonator and high-Q resonator, respectively. Through the same procedure to derive Eq. (5.17) in Sec. 5.1.2, we obtain

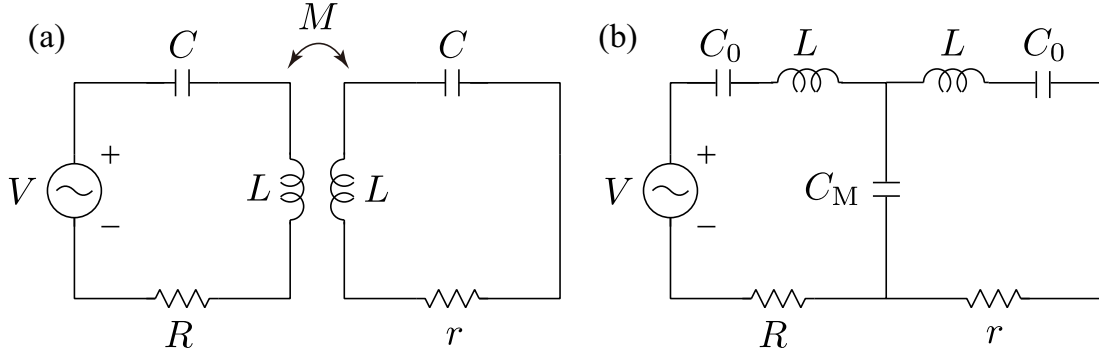


Figure 5.4: Circuit model of atomic EIT system. (a) Magnetically-coupled resonator. (b) Electrically-coupled resonator.

$$\frac{d}{dt} \begin{pmatrix} \tilde{i}_1 \\ \tilde{i}_2 \end{pmatrix} = - \begin{pmatrix} i\Delta + \frac{R}{2L} & -i\frac{\kappa\omega}{2} \\ -i\frac{\kappa\omega}{2} & i\Delta + \frac{r}{2L} \end{pmatrix} \begin{pmatrix} \tilde{i}_1 \\ \tilde{i}_2 \end{pmatrix} + \frac{1}{2} \begin{pmatrix} \tilde{v} \\ 0 \end{pmatrix}, \quad (5.34)$$

where the coupling coefficient and the detuning are introduced as $\kappa = M/L$ and $\Delta = \omega_2 - \omega$, respectively. In the derivation, we assume weak coupling limit $\kappa \ll 1$. By comparing Eq. (5.29) with Eq. (5.34), it is obvious that the currents in the circuit model are governed by the same differential equation as that for quantum states in the atomic three-level system. Then the steady-state solution is derived as

$$\tilde{i}_1 = \frac{\tilde{v}}{2L} \frac{i\Delta + \frac{\gamma_3}{2}}{\left(i\Delta + \frac{\gamma_2}{2}\right) \left(i\Delta + \frac{\gamma_3}{2}\right) + \left|\frac{\Omega_c}{2}\right|^2}, \quad (5.35)$$

by using $\gamma_2 = R/L$, $\gamma_3 = r/L$, $\Omega_c = \kappa\omega$, and $\Omega_p = -i\tilde{v}/L$.

The complex power for the current in the low-Q resonator is given as

$$P_c = \tilde{v}^* \tilde{i}_1 = \frac{|\tilde{v}|^2}{2L} \frac{i\Delta + \frac{\gamma_3}{2}}{\left(i\Delta + \frac{\gamma_2}{2}\right) \left(i\Delta + \frac{\gamma_3}{2}\right) + \left|\frac{\Omega_c}{2}\right|^2}. \quad (5.36)$$

The real part of P_c represents the dissipation and corresponds to the imaginary part of the susceptibility χ expressed by Eq. (5.31) for atomic EIT medium. As a result,

the dissipation in the circuit is suppressed in a narrow spectral region. The width of the low-dissipation region is proportional to $\Omega_c^2 = \kappa^2\omega^2$, and smaller coupling κ results in narrower low-dissipation region.[†]

In the case of the electrically-coupled resonator as shown in Fig. 5.4(b), the circuit equation is given by

$$L\frac{d^2i_1}{dt^2} + R\frac{di_1}{dt} + \frac{i_1}{C} + \frac{i_2}{C_M} = \frac{d}{dt}(\tilde{v}\cos\omega t), \quad (5.37)$$

$$L\frac{d^2i_2}{dt^2} + r\frac{di_2}{dt} + \frac{i_2}{C} + \frac{i_1}{C_M} = 0, \quad (5.38)$$

where $1/C = 1/C_0 + 1/C_M$. Equation (5.34) is replaced with

$$\frac{d}{dt} \begin{pmatrix} \tilde{i}_1 \\ \tilde{i}_2 \end{pmatrix} = - \begin{pmatrix} i\Delta + \frac{R}{2L} & \frac{i}{2\omega C_M L} \\ \frac{i}{2\omega C_M L} & i\Delta + \frac{r}{2L} \end{pmatrix} \begin{pmatrix} \tilde{i}_1 \\ \tilde{i}_2 \end{pmatrix} + \frac{1}{2} \begin{pmatrix} \tilde{v} \\ \bar{L} \\ 0 \end{pmatrix}. \quad (5.39)$$

This expression has the same form as Eq. (5.34) except the coupling term. Hence, we redefine $\Omega_c = -1/\omega C_M L$, and the electrically-coupled resonator can be regarded as identical to the magnetically-coupled resonator.

Table 5.2: Correspondence between atomic EIT system and its circuit model

Atomic EIT system	Coupled-resonator model
transition frequency : ω_2	resonant frequency : $1/\sqrt{LC}$
external field : $E_p \cos \omega t$	external voltage source : $\tilde{v} \cos \omega t$
population for $ 2\rangle$: C_2 (coherence between $ 1\rangle$ and $ 2\rangle$)	current in low-Q resonator : i_1
population for $ 3\rangle$: C_3 (coherence between $ 1\rangle$ and $ 3\rangle$)	current in high-Q resonator : i_2
decay rate for $ 2\rangle$: γ_2	dissipation rate of low-Q resonator: R/L
decay rate for $ 3\rangle$: γ_3	dissipation rate of high-Q resonator: r/L
Rabi frequency by control light : Ω_c	coupling of the resonators: $\kappa\omega$ or $1/\omega C_M L$
absorption of probe light : $\text{Im}[\chi]$	dissipated power: $\text{Re}[P_c]$

[†] $\Omega_c = \kappa\omega$ is obviously frequency dependent, though it can be considered nearly constant $\kappa\omega_2$ in the weak coupling limit $\kappa \ll 1$.

The correspondences between the quantum EIT system and its circuit model are summarized in Table 5.2.

5.2.3 Metamaterial analogy of EIT effects

The EIT effects can be realized with metamaterials composed of meta-atoms that are described by the circuit model provided in the previous section. In the circuit model, two resonators with different quality factors are coupled and only the resonator with low-Q factor is excited. On the other hand, the metamaterial to realize the EIT effects, called an EIT metamaterial, consists of meta-atoms with two resonant structures, or two resonant modes, with different quality factors, and only the resonator with low-Q factor is excited by external electromagnetic waves. In the presence of the coupling between the two resonators, which we refer to as EIT coupling, the EIT effects including narrow-band transparency and slow-light propagation are realized.

Before showing realistic structures of the EIT metamaterials, we provide an overview of the EIT effects in metamaterials with a concept model shown in Fig. 5.5 (a). The left (right) circle corresponds to the a low-Q (high-Q) resonator, and the antenna symbolically represents the function of receiving external electromagnetic waves. It should be noted that the high-Q resonator cannot be directly excited by the external fields. The resonant mode with the low-Q factor is called “*radiative*

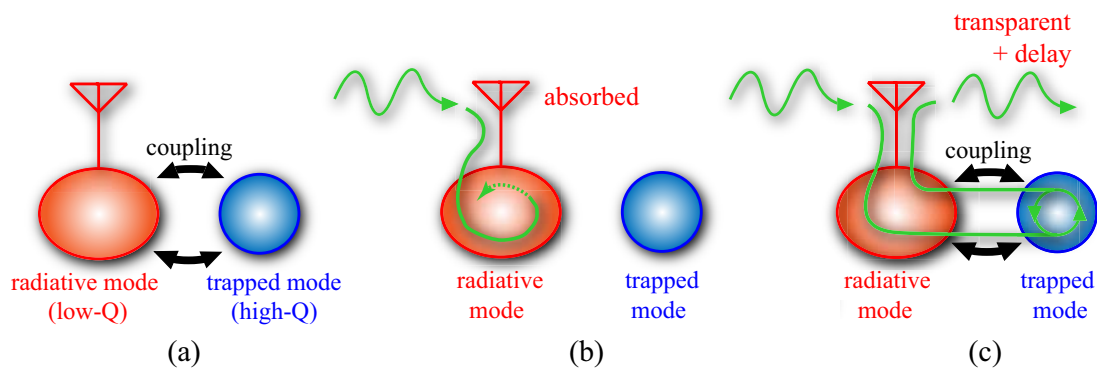


Figure 5.5: (a) Concept model of EIT metamaterial. (b) Coupling is turned off. (c) Coupling is turned on.

mode” and one with the high-Q factor is called “*trapped mode*.” Without the EIT coupling as shown in Fig. 5.5 (b), the energy in the radiative mode excited by the external fields is rapidly consumed due to high dissipation in the low-Q resonator, and, consequently, the propagating waves are absorbed in the metamaterial. On the other hand, in the presence of the EIT coupling as shown in Fig. 5.5 (c), the metamaterial is rendered transparent, because the energy received through the radiative mode is transferred into the trapped mode with low losses via the EIT coupling. In addition to the transparency, the propagation is slowed down in the metamaterial owing to the temporal storage in the trapped mode.

In actual EIT metamaterials, electric dipole resonance is often used as a radiative mode [28, 40, 78–97], because electric dipole oscillation effectively interacts with far field or propagating waves. In other words, the stored energy in the resonant mode is quickly released into propagating waves, and the quality factor as a resonator is relatively low due to the radiation dissipation. On the other hand, lower dissipative resonance such as magnetic dipole resonance and electric quadrupole resonance can be used for a trapped mode. As a typical example of the EIT metamaterials, the proposal by Zhang’s group [79] is shown in Fig. 5.6. Their EIT metamaterial is comprised of two elements: a dipole antenna shown in Fig. 5.6(a) and a pair of strips shown in Fig. 5.6(b). The polarization of incident EM field is also shown at the left-hand side of Fig. 5.6(a). As shown in Fig. 5.6(a), electric dipole resonance in the dipole antenna is induced by oscillating electric fields, when the half of the wavelength is adjusted around the length of the antenna. Hence, this resonance

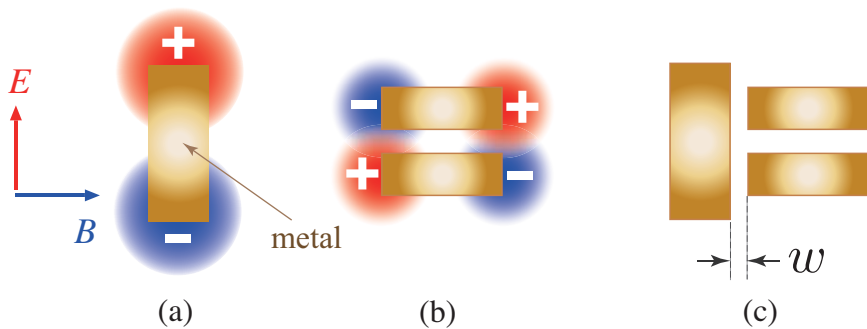


Figure 5.6: (a) Dipole antenna. (b) Pair of strips. (c) Composite structure.

serves as a radiative mode. On the other hand, the pair of stripes has an electric quadrupole resonance mode as shown in Fig. 5.6(b) and serves as a trapped mode. It should be noted that the incident EM field does not directly excite the quadrupole resonance in long wavelength limit. The resonance frequencies for the radiative mode and the trapped mode are tuned to be the same by adjusting the dimensions of the structure. In order to observe EIT effects, the radiative mode and the trapped mode are coupled with each other by placing two structures closely as shown in Fig. 5.6(c).

The circuit model of a “meta-atom” for the metamaterial is expressed by the electrically-coupled resonators as shown in Fig. 5.3(b), and the current \tilde{i}_1 in the dipole antenna can be expressed by Eq. (5.35). As described in Sec. 5.1.3, the dipole moment \tilde{p} is proportional to the current \tilde{i}_1 in the dipole antenna, and the resulting susceptibility of the metamaterial with the meta-atom density of N becomes

$$\chi = i \frac{ldN}{\epsilon_0 \omega} \frac{\tilde{i}_1}{\tilde{v}} = i \frac{ldN}{2\epsilon_0 \omega L} \frac{i\Delta + \frac{\gamma_3}{2}}{\left(i\Delta + \frac{\gamma_2}{2}\right) \left(i\Delta + \frac{\gamma_3}{2}\right) + \left|\frac{\Omega_c}{2}\right|^2}, \quad (5.40)$$

where γ_2 and γ_3 can be interpreted as the dissipation in the radiative mode and the trapped mode, respectively. As a result, the above expression is written in the same form as the susceptibility of atomic EIT medium given by Eq. (5.31). This fact means that the EIT metamaterial responds to EM fields in completely the same way as the atomic EIT medium. It is possible to control the coupling strength Ω_c by changing the distance w between the two structures instead of changing the intensity of the control light for the atomic EIT medium.

Chapter 6

Storage of electromagnetic waves in metamaterial

In the previous chapter, we have dealt with the metamaterial that mimics atomic EIT effects and shown that the metamaterial responds to classical EM waves in the same fashion as the atomic EIT medium. Various types of EIT metamaterials have been proposed, and the narrow-band transparency and slow propagation of EM waves have been experimentally demonstrated in microwave [78, 80, 86], terahertz [81, 89–91], and optical regions [28, 83, 87]. The sharp transparency can be used for accurate sensing [82] and selective excitation of highly-localized plasmonic modes [92]. However, storage of EM waves in EIT metamaterials has not been reported yet, though the storage of light in atomic EIT medium has been one of the most promising technologies as the applications of the EIT effects. In order to realize the storage of EM waves in the EIT metamaterials, it is necessary to dynamically switch the EIT effects in the same way as the case of the atomic EIT, which has been discussed in Sec. 4.1.1. In other words, the coupling strength between the radiative mode and the trapped mode of the EIT metamaterial has to be modulated instead of the intensity of the control light in atomic EIT system. Semi-static modulation of the EIT effects has been demonstrated [85, 93–95, 97], but the fast modulation, which is required for the storage of EM waves, has not been reported. In order to implement property-controllable metamaterials, which are referred to as tunable metamaterials [98], the constituents include tunable elements or material:

variable capacitors called varactor diodes [99–102] or transistors [103]; superconductor [104, 105]; photodiodes and light emitting diodes [106, 107]; photoexcitation in semiconductor [8, 95, 97, 108]; vanadium dioxide [109]; carbon nanotube [110] or graphene [111]; liquid crystal [112]; elastic material [113, 114]; plasma gas [115, 116]; micro electro mechanical systems (MEMS) [117–119] and so on. In this chapter, we propose an EIT metamaterial whose properties can be controlled by bias voltage applied to varactor diodes. We discuss the structure and the operating principle of the tunable EIT metamaterial, introducing its circuit model and numerical simulation. Then, we will show experimental demonstration of EM-wave storage in microwave region [120].

6.1 Tunable EIT metamaterial

6.1.1 Structure and operating principle

Figure 6.1(a) illustrates the unit cell of a tunable EIT metamaterial we propose. It is assumed that the capacitances of two capacitors denoted by C_1 and C_2 can be controlled and external fields have the polarization as denoted at the left-hand side of the diagram. For the case of $C_1 = C_2$, the currents in the structure form two eigenmodes as shown in Fig. 6.1(b) and (c), which are characterized by the relative phase of the currents flowing in the two capacitors as expressed by i_1 and i_2 . The

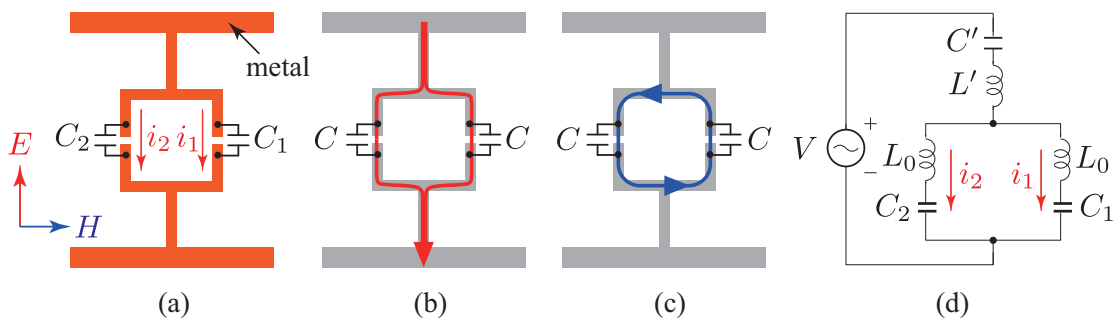


Figure 6.1: (a) Unit cell of tunable EIT metamaterial. (b) Radiative mode. (c) Trapped mode. (d) Circuit model.

symmetric current as shown in Fig. 6.1(b) forms electric dipole oscillation, which is excited by the external field and is highly radiative. On the other hand, the anti-symmetric current as shown in Fig. 6.1(c) forms loop current, or magnetic dipole oscillation, which is less radiative and is uncoupled to the external field. The former mode could be a radiative mode and the latter mode could be a trapped mode. We suppose that the resonant frequencies for these two modes are adjusted to be identical. It should be noted that the case of $C_1 = C_2$ shows no EIT effect because the two modes are eigenmode and are decoupled. By destroying the symmetry, i. e. $C_1 \neq C_2$, these two modes are coupled and EIT effects can be expected. The degree of the asymmetry determines the coupling strength and the width of the transparency window. The design of our EIT metamaterial is based on the EIT metamaterials with broken structural symmetry [78, 88, 90], and dynamical control of the structural symmetry with variable capacitors contributes to dynamical modulation of the EIT effects.

6.1.2 Circuit model

In the previous section, qualitative explanation was provided. Here we introduce a circuit model as shown in Fig. 6.1(d) to analyze our EIT metamaterial more precisely. The inductance L' , $2L_0$, and the capacitance C' correspond to the metal inductance except the loop, the loop inductance, and the capacitance between neighboring cells, respectively. It is easy to obtain the circuit equations for i_1 and i_2 as follows:

$$L' \frac{d^2(i_1 + i_2)}{dt^2} + \frac{i_1 + i_2}{C'} + L_0 \frac{d^2 i_1}{dt^2} + \frac{i_1}{C_1} = \frac{d}{dt}(\tilde{v} \cos \omega t), \quad (6.1)$$

$$L' \frac{d^2(i_1 + i_2)}{dt^2} + \frac{i_1 + i_2}{C'} + L_0 \frac{d^2 i_2}{dt^2} + \frac{i_2}{C_2} = \frac{d}{dt}(\tilde{v} \cos \omega t). \quad (6.2)$$

Here, we rewrite the above equations with another variables $i_{\pm} = i_1 \pm i_2$ as

$$L \frac{d^2 i_+}{dt^2} + \frac{i_+}{C_+} + \frac{i_-}{\Delta C} = \frac{d}{dt}(2\tilde{v} \cos \omega t), \quad (6.3)$$

$$L_0 \frac{d^2 i_-}{dt^2} + \frac{i_-}{C_-} + \frac{i_+}{\Delta C} = 0, \quad (6.4)$$

where we define $L = 2L' + L_0$ and

$$\frac{1}{C_+} = \frac{2}{C'} + \frac{1}{2C_1} + \frac{1}{2C_2}, \quad \frac{1}{C_-} = \frac{1}{2C_1} + \frac{1}{2C_2}, \quad \frac{1}{\Delta C} = \frac{1}{2C_1} - \frac{1}{2C_2}. \quad (6.5)$$

If $C_1 = C_2$, i_+ and i_- form eigenmodes with resonant frequency of $\omega_+ = 1/\sqrt{C_+L}$ and $\omega_- = 1/\sqrt{C_-L_0}$. The former forms electric dipole resonance with high radiation loss and the latter forms loop current or magnetic dipole resonance with lower loss. Taking the radiation losses into account, we modify Eqs. (6.3) and (6.4) as

$$L \frac{d^2 i_+}{dt^2} + R \frac{di_+}{dt} + \frac{i_+}{C_+} + \frac{i_-}{\Delta C} = \frac{d}{dt}(2\tilde{v} \cos \omega t), \quad (6.6)$$

$$L_0 \frac{d^2 i_-}{dt^2} + r \frac{di_-}{dt} + \frac{i_-}{C_-} + \frac{i_+}{\Delta C} = 0. \quad (6.7)$$

These equations are expressed in the same form as Eqs. (5.37) and (5.38). We suppose $\omega_+ = \omega_-$, which can be realized by tuning the dimensions of the structure and the value of the capacitances. By using the same procedure to obtain Eq. (5.35), we obtain the steady-state solution in the same form as Eq. (5.35) as follows:

$$\tilde{i}_+ = \frac{\tilde{v}}{L} \frac{i\Delta + \frac{\gamma_3}{2}}{\left(i\Delta + \frac{\gamma_2}{2}\right) \left(i\Delta + \frac{\gamma_3}{2}\right) + \left|\frac{\Omega_c}{2}\right|^2}, \quad (6.8)$$

where $\gamma_2 = R/(2L)$, $\gamma_3 = r/(2L_0)$ and the coupling Ω_c is redefined as

$$\Omega_c^2 = \frac{1}{\omega^2 (\Delta C)^2 L L_0}. \quad (6.9)$$

We assume that the structures shown in Fig. 6.1(a) are homogeneously distributed in space with the density of N . Only the in-phase current i_+ creates the electric dipole moment, and the electrical susceptibility is

$$\chi = i \frac{ldN}{\epsilon_0 \omega L} \frac{i\Delta + \frac{\gamma_3}{2}}{\left(i\Delta + \frac{\gamma_2}{2}\right) \left(i\Delta + \frac{\gamma_3}{2}\right) + \left|\frac{\Omega_c}{2}\right|^2}, \quad (6.10)$$

which can be obtained in the same way of the derivation of Eq. (5.40). For symmetric case $C_1 = C_2$, which means $1/(\Delta C) = 0$ from the definition (6.5), the coupling strength is $\Omega_c = 0$ and no EIT effect is observed. For asymmetric case $C_1 \neq C_2$, the coupling strength Ω_c becomes finite and the EIT effect can be expected. The larger the degree of the asymmetry, the wider the transparent window. These facts are consistent with the qualitative explanation discussed in the previous section.

6.2 Simulation of transmission spectra

Figure 6.2(a) shows a unit cell of our metamaterial, which is made of metal. Two variable capacitors, C_1 and C_2 , are introduced at two gaps in the center loop to dynamically control the EIT properties. We calculate the transmission properties of the metamaterial using an electromagnetic simulator (CST MW STUDIO) for various pairs of values for C_1 and C_2 . In the simulation, periodic boundary conditions are imposed for the unit cell with a size of $120\text{ mm} \times 25\text{ mm}$ as shown in Figs 6.2(b) to simulate an infinite array of the unit structures. The incident waves are vertically polarized. The thickness and permittivity of the substrate is assumed to be 0.8 mm and 3.3 .

The calculated transmission spectra are shown in Fig. 6.3(a) for $C_1 = C_2 = 2.1\text{pF}$ (bottom), $C_1 = 1.91\text{pF}, C_2 = 2.33\text{pF}$ (middle), and $C_1 = 1.75\text{pF}, C_2 = 2.63\text{pF}$ (top). For $C_1 = C_2$, the transmission is depressed over a broad spectrum. At the center of the depression, a resonant current is induced on the metal, as shown in Fig. 6.3(b). This mode forms an electric dipole oscillation, and can be regarded as a radiative mode. On the other hand, for $C_1 \neq C_2$, sharp transparent regions appear in the broad resonant line. At the transmission peak, a resonant loop current is induced, as shown in Fig. 6.3(c), and this can be regarded as a trapped mode, which has a much higher quality factor than the radiative mode and is decoupled from incident wave. (The structure is designed so that the resonant frequencies of the two modes coincide.) The electromagnetic energy received in the

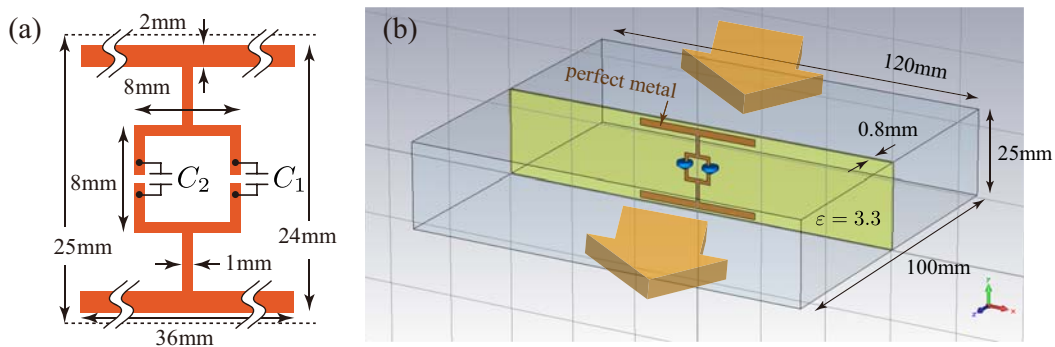


Figure 6.2: (a) Unit structure and its dimensions. (b) Simulation setup.

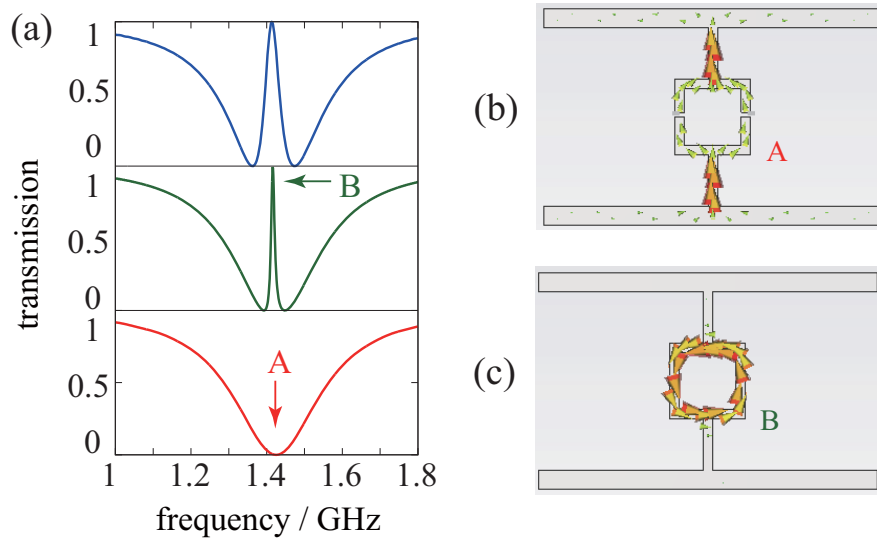


Figure 6.3: (a) Transmission spectra for $C_1 = C_2 = 2.1\text{pF}$ (bottom), $C_1 = 1.91\text{pF}, C_2 = 2.33\text{pF}$ (middle), and $C_1 = 1.75\text{pF}, C_2 = 2.63\text{pF}$ (top). Current distributions for (b) point A and (c) point B.

radiative mode is transferred into the trapped mode through a coupling, which is provided by breaking the symmetry of the metamaterial. As a result, dissipation is suppressed and the metamaterial is rendered transparent. The increase in the degree of asymmetry results in the broadening of the transparent window, as is clearly shown in the middle and top panels of Fig. 6.3(a). It is possible to control the width of the transparent window $\Delta\omega$ without changing the center of the window. This is accomplished by keeping the composite capacitance in the loop, $C_L = C_1 C_2 / (C_1 + C_2)$, constant. The minimum of $\Delta\omega$ is limited by the linewidth of an isolated trapped mode, which is determined by the radiation loss of the loop current and Ohmic loss in the capacitors. The transparency peak is deteriorated by the loss in the trapped mode.

6.3 Experimental demonstration

In this section, we first describe the fabrication of the tunable EIT metamaterial and experimental setup. Next, the semi-static characteristics obtained from the

experiment is shown. Finally, we demonstrate the storage of EM waves in the EIT metamaterial by dynamically modulating the EIT properties.

6.3.1 Fabrication of metamaterial and experimental setup

Design of the metamaterial

To experimentally demonstrate the EIT effects in the microwave region, we fabricated the proposed structures using a copper film on a dielectric substrate with a dimensions $(W \times H \times D) = (120 \text{ mm} \times 25 \text{ mm} \times 0.8 \text{ mm})$ and a permittivity of 3.3. The photographs are shown in Fig. 6.4(a) and (b). In one side of the loop, we introduced a varactor diode (Infineon BBY52-02W), whose capacitance C_1 is a function of the applied bias voltage V . The bias voltage was fed through 180-nH inductors, which were introduced to pass only the bias voltage and to isolate the structure from the bias circuitry for signals at the operating frequency of the metamaterial of over 1 GHz. Ohmic loss in the varactor diode, which is not negligible, degrades the quality factor of the trapped mode. Therefore, we used a normal capacitor ($C_2 = 1.2 \text{ pF}$) with low Ohmic loss at the other side. In this situation, unlike a simulation in which C_L is kept constant, the center and width of the transparent window are expected to change with $C_1(V)$.

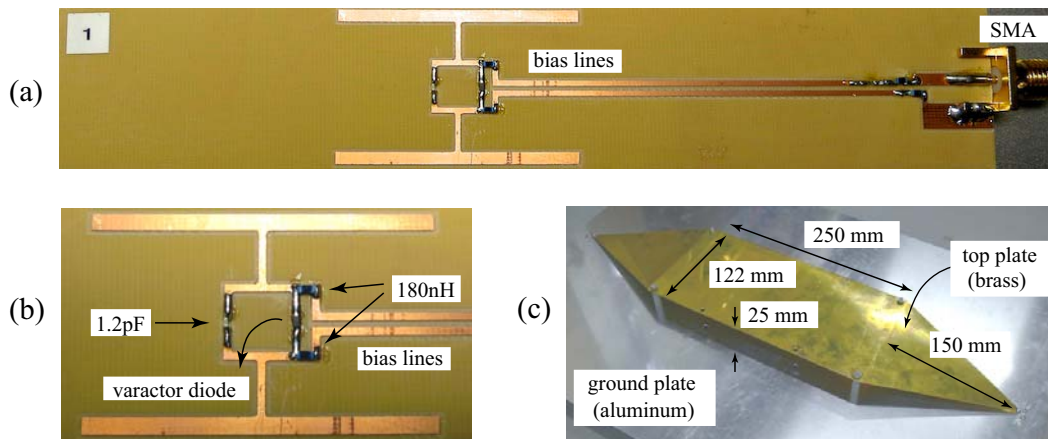


Figure 6.4: Photographs of (a) the unit structure and (b) its enlarged view. (c) Waveguide structure and its dimensions.

Waveguide

For measurements, we used a waveguide called a stripline TEM-cell as shown in Fig. 6.4(c) [121, 122]. The waveguide supports a TEM mode propagating. The tapered structures ensure that the wave impedance is maintained at 50Ω along the waveguide and the tips of the top plate are connected to the input and output ports, which have SMA connectors. Figure 6.5 shows the experimental results of the transmission spectrum with asterisks. The simulation results conducted with CST MW STUDIO are also displayed with a solid line. Around an operating frequency ~ 1.5 GHz, the waveguide exhibits high transmission around -2 dB. We also simulate electric fields at the center of the waveguide for three frequencies, 1.5 GHz, 3.0 GHz, and 6.0 GHz as shown in Figure 6.6. It is confirmed that the electric fields are almost uniformly distributed under the top plate in lower frequency region < 3.0 GHz. Thus we can expect that each element of the metamaterial interacts with nearly uniform TEM waves around the operating frequency.

Three layers of the metamaterial, each of which contained a single structure, were prepared. We placed these layers in the waveguide with a separation of 7 cm, which was sufficient to avoid undesired coupling between the layers.

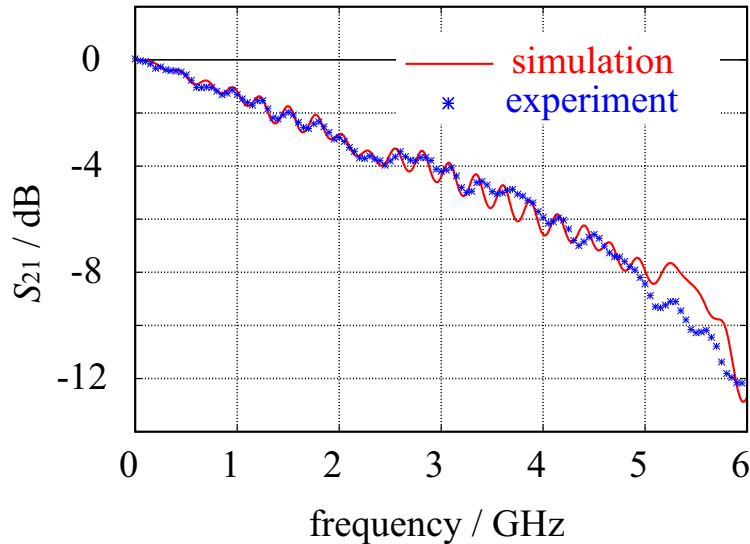


Figure 6.5: Transmission spectrum of waveguide.

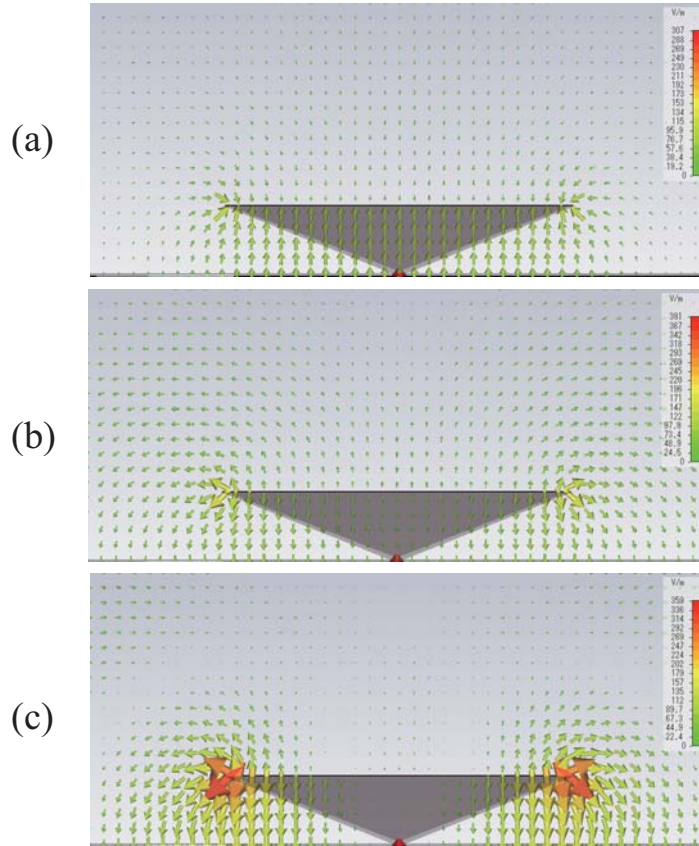


Figure 6.6: Electric field distributions at the center of the waveguide for (a) 1.5 GHz, (b) 3.0 GHz, (c) 6.0 GHz

6.3.2 Semi-static characteristics

Transmission spectra

The results of these transmission measurements for various V are shown in Fig. 6.7(a). For $V = -3.6$ V, a broad depression in the transmission is observed. This indicates that the elements of the metamaterial are symmetric, i.e., $C_1(V) \simeq C_2 = 1.2$ pF, which agrees with the value in the varactor diode data sheet. By breaking the symmetry, we can observe transparent windows. When increasing $C_1(V)$ by reducing $|V|$, the asymmetry of the structure is enhanced, and the transparent window becomes wider. The transmission peaks shift to a lower frequency because they correspond to the resonant frequencies of the trapped modes,

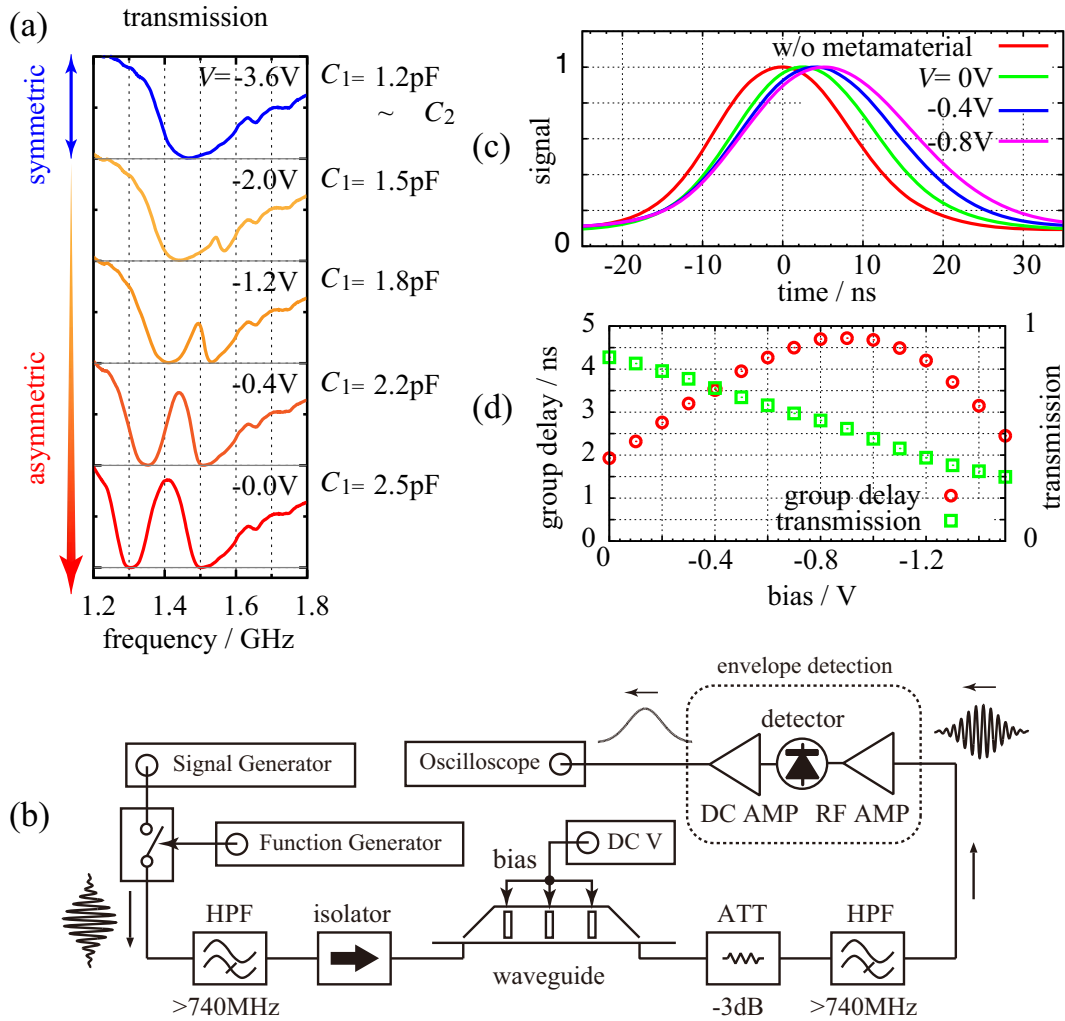


Figure 6.7: (a) Transmission spectra of EIT metamaterial for $V = 0, -0.4, -0.8, -1.2, -2.0, -3.6\text{ V}$. (b) Experimental setup for measurement of group delay. (c) Group delays for $V = 0, -0.4, -0.8\text{ V}$. (d) Relations of group delays and transmission peaks.

which are determined by the loop capacitance C_L . This is the difference from the simulation results where both capacitances are changed with keeping C_L constant.

Group delays

We also estimate the group delay of the three-layered metamaterial by measuring the transit time of pulses. Figure 6.7(b) is the brief diagram of an experimental setup, which is also used for other experiments with some modifications. A signal generator (Agilent N5183A) and a RF switch (Mini circuit 2FSWA-2-46) controlled by a function generator were used to prepare a band-limited pulse. The carrier frequency of the pulse was tuned to a transparent peak for each bias voltage. The signal passing through a high pass filter (HPF) and an isolator was sent to the waveguide, in which the three-layered metamaterial was placed. The output signal passed through an attenuator and a HPF to reduce reflections, and was introduced to the envelope detection system composed of a RF amplifier (Mini circuit 2RL-2150+), a diode detector for rectification (Agilent 8474B), and a DC amplifier (FEMTO HVA-200M-40-B). The produced envelope signal was acquired by an oscilloscope. The bias voltage applied to each element of the metamaterial was fed by a DC voltage source.

Figure 6.7(c) shows observed envelope signals transmitted through the metamaterial with the bias voltages of $V = 0, -0.4 \text{ V}, -0.8 \text{ V}$. For comparison, the output signal in the absence of the metamaterial is also displayed. We can confirm that each signal passing through the metamaterial is delayed with maintaining the shape of the pulse depending on the bias voltage.

The graph in Fig. 6.7(d) represents the group delays and transmissions at the center of transparency windows. From $V = 0$ to $V = -0.9 \text{ V}$, the group delay increases with $|V|$. This is because the transparent window becomes sharper for larger $|V|$ and the group velocity in the metamaterial becomes slower. For $V < -0.9 \text{ V}$, transparent windows are corrupted, and the group delay is decreased.

6.3.3 Dynamic modulation of EIT property

Next, we demonstrate the modulation of continuous waves by varying V with time to confirm the dynamic control of the EIT effect and to identify the timing and transient time of the modulation. The experimental setup is almost the same as Fig. 6.7(b) for the delay measurement discussed in the previous section. In this

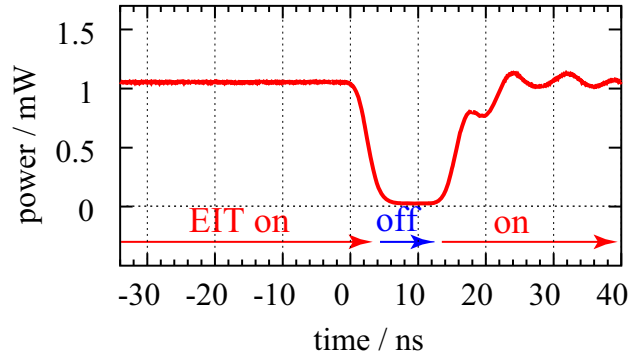


Figure 6.8: Modulation of a continuous wave.

experiment, we replaced the DC voltage source with a pulse generator (Stanford Research Systems DG645). By using the pulse generator, we applied negative rectangular pulses with an amplitude of 3.2 V, an offset of -0.4 V, and a width of $\tau = 10$ ns, at the same time for all of the varactors. With this setting, the transmission property of the metamaterial switches from the second lowest spectrum ($V = -0.4$ V) to the top spectrum ($V = -3.6$ V) in Fig. 6.7(a). The signal generator fed continuous waves at 1.440 GHz, which corresponds to the transmission peak for $V = -0.4$ V, into the waveguide containing the three-layered metamaterial.* We recorded the power of the waves transmitted through the waveguide by monitoring the envelope signals.

Figure 6.8 shows transmitted microwave power under the modulation of the metamaterial. The origin for time t is set to the moment when the signal starts to decrease. For $t < 0$, the bias is $V = -0.4$ V, and the incident waves can travel through the metamaterial because of the EIT effect. After some transient time of around 4 ns from $t = 0$, almost all of the energy is blocked by the metamaterial, because the EIT effect disappears for $V = -3.6$ V. At $t = \tau + t_T$, where t_T (~ 3 ns) is the transient time for a transparent window to emerge through the discharge of the varactor diode, the transmission starts to recover. In Fig. 6.8, the state denoted “EIT on” (“EIT off”) corresponds to the state in which the trapped mode and the radiative mode are coupled (decoupled).

*In this experiment, the switch was kept turned on.

6.3.4 Storage of EM waves

Procedures

In the Sec. 4.1.1, we introduced the procedures for light storage in atomic EIT media using Fig. 4.2. Even in the EIT metamaterial, the dynamic switching between EIT on and EIT off states enables the storage of electromagnetic waves. We explain the procedures of EM storage in the EIT metamaterial, using the concept model of the EIT metamaterial as shown Fig. 6.9. First, the metamaterial is prepared in an EIT on state, in which the radiative and trapped modes are coupled. If the spectrum of the incident pulse is in the transparent window, the pulse transmits through the metamaterial with the transit time or group delay. The delay corresponds to

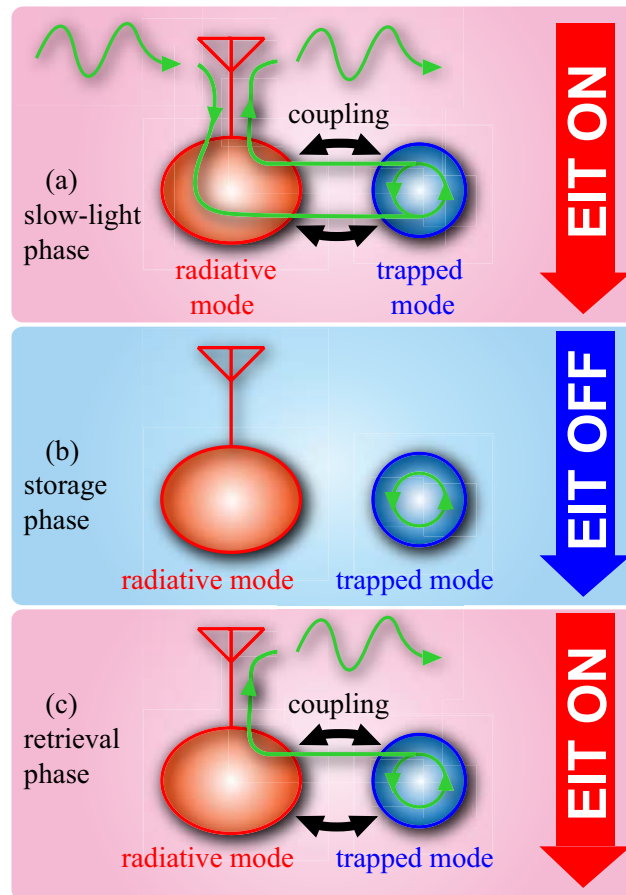


Figure 6.9: Procedures for EM storage.

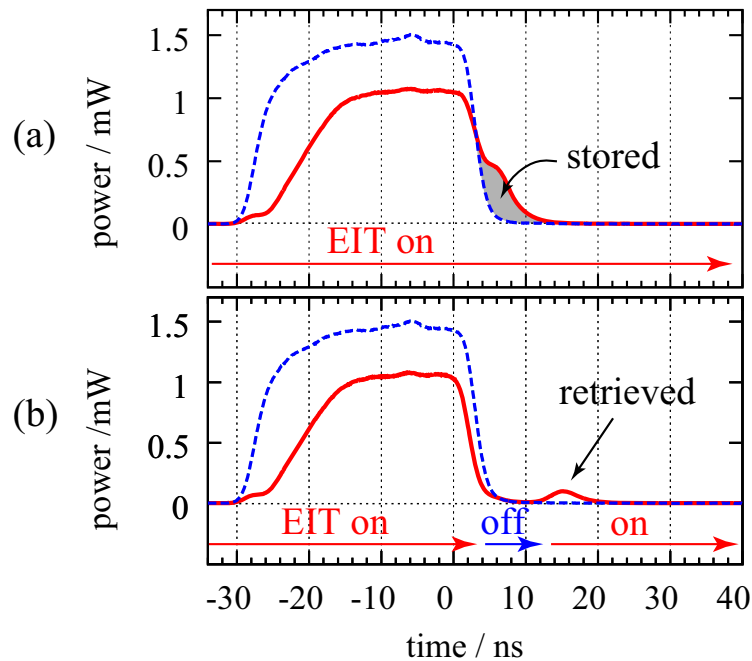


Figure 6.10: (a) Original pulse (dotted line) and transmitted pulse (solid line) for $V = -0.4$ V. (b) Storage and retrieval of electromagnetic energy for a control pulse with a width of $\tau = 10$ ns.

the time period when the electromagnetic energy received in the radiative mode is transferred into the trapped mode and returns to the radiative mode through coupling. If during the propagation the metamaterial is changed into an EIT off state, where the two resonant modes are decoupled, some of the energy is captured in the trapped mode. Then, this energy is released by returning the metamaterial to an EIT on state to reintroduce the coupling.

Experimental demonstration of EM storage

Before the demonstration of pulse storage, we measured the transmission of a pulse through the metamaterial in an EIT on state to estimate the delay of the pulse due to slow propagation in the metamaterial. We prepared a 35-ns pulse with a carrier frequency of 1.440 GHz. The dotted line and the solid line in Fig. 6.10(a) represent the power of the pulse transmitted through the waveguide without and

with the metamaterial, respectively, for $V = -0.4\text{ V}$. Compared with the original pulse, a fraction of the transmitted pulse is delayed by 3 to 4 ns, which corresponds to the transit time for some components of the input pulse within the transparent window. (The component outside of the transparent window is blocked by the metamaterial.) In other words, the power in the gray region is temporally stored in the trapped modes. The energy in the gray region can be captured in the trapped modes by switching the metamaterial from the EIT on state to the EIT off state when the input pulse is turned off.

To demonstrate the storage and retrieval of EM waves, we modulated the bias voltage with a width of $\tau = 10\text{ ns}$ in the same way as in Fig. 6.8 for an input microwave pulse represented by the dotted line in Fig. 6.10(a), which is redisplayed as a dotted line in Fig. 6.10(b). In order to hold the energy corresponding to the gray region in Fig. 6.10(a), we adjusted the timing so that the original pulse is turned off at $t = 0$. Figure 6.10(b) shows the transmitted power as a solid line. In comparison with the unmodulated case shown in Fig. 6.10(a), the delayed component (the gray region) is not observed because the energy is captured in the trapped modes, which are decoupled from the radiative modes in the EIT off state. The stored energy starts to be radiated from the radiative mode, when the coupling

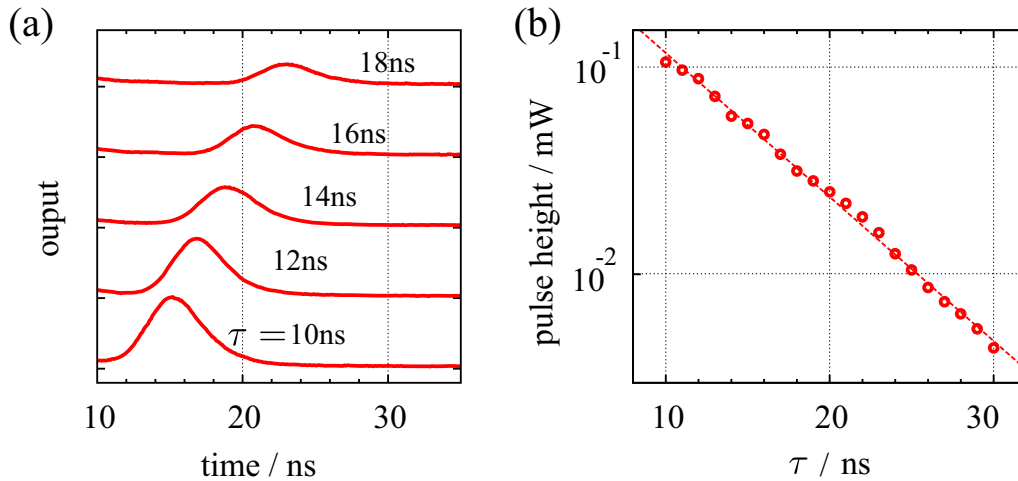


Figure 6.11: (a) Retrieved pulses for various τ . (b) Pulse heights of the retrieved pulses as a function of storage time τ .

between the trapped modes and the radiative modes is restored and the transparent window begins to open. By comparing the height of the retrieved pulse at $t = 15$ ns with the height of the original pulse, the efficiency of retrieval is estimated to be about 10%.

Figure 6.11(a) shows the magnified waveforms of retrieved pulses for various τ . The magnitudes of the retrieved pulses are reduced with increasing τ , because the stored energy decays in the trapped mode during the EIT off state. Figure 6.11(b) shows the heights of the retrieved pulses as a function of the storage time τ . The height of the retrieved pulses decays exponentially with a time constant of 6.3 ns, which corresponds to the lifetime of the trapped mode.

Coherence of retrieved waves

We compare retrieved pulses propagating in the backward and forward directions for n -layered metamaterials ($n = 1, 2, 3$) by measuring the waveforms of the reflected and transmitted waves. Figure 6.12 shows retrieved pulses for forward (backward) waves on the left (right) side. For $n = 1$, we observe almost the same amplitudes of

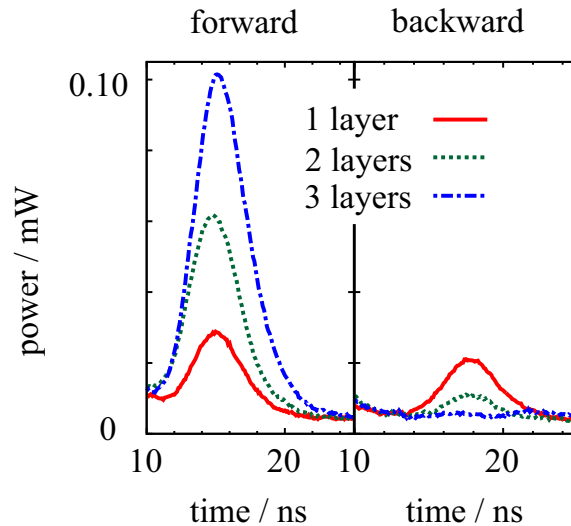


Figure 6.12: Retrieved pulses propagating forward (left) and backward (right) for various n .

retrieved signals propagating in opposite directions because the energy is radiated from a single emitter. With increasing n , the retrieved pulses become stronger for forward propagation but diminish for backward propagation. This indicates that the oscillation in each trapped mode during the storage process “inherits” the relative phase of the oscillating electric field of the incident waves at each location, and the retrieved pulse reproduces the phase distributions of the incident waves.

6.3.5 Discussions

In this chapter, we have presented a method of dynamically modulating the properties of a varactor-loaded EIT metamaterial, whose characteristics can be controlled by an external voltage source. We have achieved the storage and retrieval of electromagnetic waves. In our experiment, even though we used only three elements of the metamaterial to avoid technical problems such as transmission reduction caused by Ohmic loss in the varactor diodes, we still retrieved 10% of the original pulse height after a storage time of 10 ns. Decay in the trapped mode limits the storage time. The metamaterials with high-Q structures proposed recently using toroidal resonators [123] or low-loss dielectric resonators [124] would be candidates to extend the storage time. Loss compensation by an amplification process would be an alternative solution, which is discussed in Sec. 8.2 [82].

We introduced a varactor diode on one side of the element, and the resonant frequency of the trapped mode varied, depending on the bias voltage. Therefore, the oscillation frequency of the trapped mode during the storage period was different from that of the incident waves. The retrieved pulse is frequency chirped because energy is released from the frequency-shifting trapped mode through the radiative mode during the transition time t_T . In order to avoid this frequency chirp, we must reduce t_T by improving the bias circuitry or change both capacitances simultaneously, as was done in the simulation.

We have also shown that the traveling pulses can be stored and recovered without losing their phase information. These results suggest that if we increase the number of layers, we could potentially store the whole of an input pulse with arbitrary temporal shape. It is also possible to store waves with arbitrary transverse modes

and any polarizations by appropriately distributing the elements. We believe that the present approach can be applied even to optical regions by replacing the varactor diodes by other nonlinear elements such as a nonlinear optical crystal substrate, whose refractive index can be changed by auxiliary light.

Chapter 7

Nonlinearity enhancement using doubly resonant metamaterial

Numerous studies on metamaterials have focused on the linear response characteristics of metamaterials. Recent studies have also reported the development of nonlinear media and the control of the nonlinear properties of the metamaterials through the introduction of nonlinear elements into the constituents of metamaterial [98, 125]. High nonlinearity can be achieved in resonant-type metamaterials such as split ring resonators (SRRs) by placing nonlinear elements at locations where the electric (or magnetic) field is concentrated due to the resonance effect [5]. Nonlinear metamaterials have been studied for property tuning, frequency mixing [126–128], imaging beyond diffraction limit [129], modulation instability [130], and developing bistable media [101, 131–133]. Several kinds of nonlinear metamaterials for generating second harmonic (SH) waves have been reported. Most of the metamaterials are designed such that they resonate with the incident waves or the fundamental waves [100, 134–138]. These are called singly resonant metamaterials. If the structure has resonant modes not only for the fundamental frequency but also for the SH frequency, SH radiation could be enhanced [139, 140]. In this chapter, we propose a method to implement metamaterials satisfying the doubly resonant condition, or a doubly resonant metamaterial, using coupled split ring resonators (CSRRs) loaded with two varactor diodes, which generate SH waves due to nonlinearity [141]. There are two resonant modes in the CSRR structure: one for the fundamental waves; the

other for the SH waves. They are coupled owing to the nonlinearity of the diodes. The SH oscillation excited in the varactors directly excites the SH resonance mode through the nonlinearity-assisted coupling. Second harmonic generation (SHG) through the CSRRs is more efficient than that through the previously proposed metamaterial with two resonant modes, where SH oscillation indirectly excites the resonant mode designed for the SH waves through magnetic coupling. [140] We demonstrate experiments in the microwave region to estimate the SHG efficiency of the CSRRs, comparing the singly resonant metamaterial.

7.1 Structure and circuit model

7.1.1 Singly resonant metamaterial

The varactor-loaded split ring resonator (SRR) shown in Fig. 7.1(a) is a typical example of singly resonant nonlinear metamaterials. It can be modeled as a series resonant circuit composed of an inductor, varactor, and resistor, as shown in Fig. 7.1(b). The electromotive force induced by the external magnetic field B is represented by the voltage source $V(t) = V_0 \cos \omega t$ in the circuit model. If we consider the varactor as a normal capacitor without nonlinearity, the circuit is a simple harmonic oscillator driven by the external force, and the voltage across the capacitor, v_C , reaches a maximum at the resonant angular frequency $\omega_0 = 1/\sqrt{LC}$. However, the varactor has nonlinearity in the capacitance and its voltage v_C with respect to the charge q can be represented as $v_C = q/C(q) = q/C + \alpha q^2$. The equation of motion for q is written as

$$L \frac{d^2 q}{dt^2} + R \frac{dq}{dt} + \frac{q}{C} + \alpha q^2 = V_0 \cos \omega t. \quad (7.1)$$

An anharmonic term αq^2 contributes to the generation of second- or higher-order harmonic waves. Using the perturbation method under a weak nonlinearity condition [122], the complex amplitude of the SH oscillation is obtained as

$$\tilde{q}(2\omega) = \frac{\alpha V_0^2}{\omega^3 Z(2\omega) Z(\omega)^2}, \quad (7.2)$$

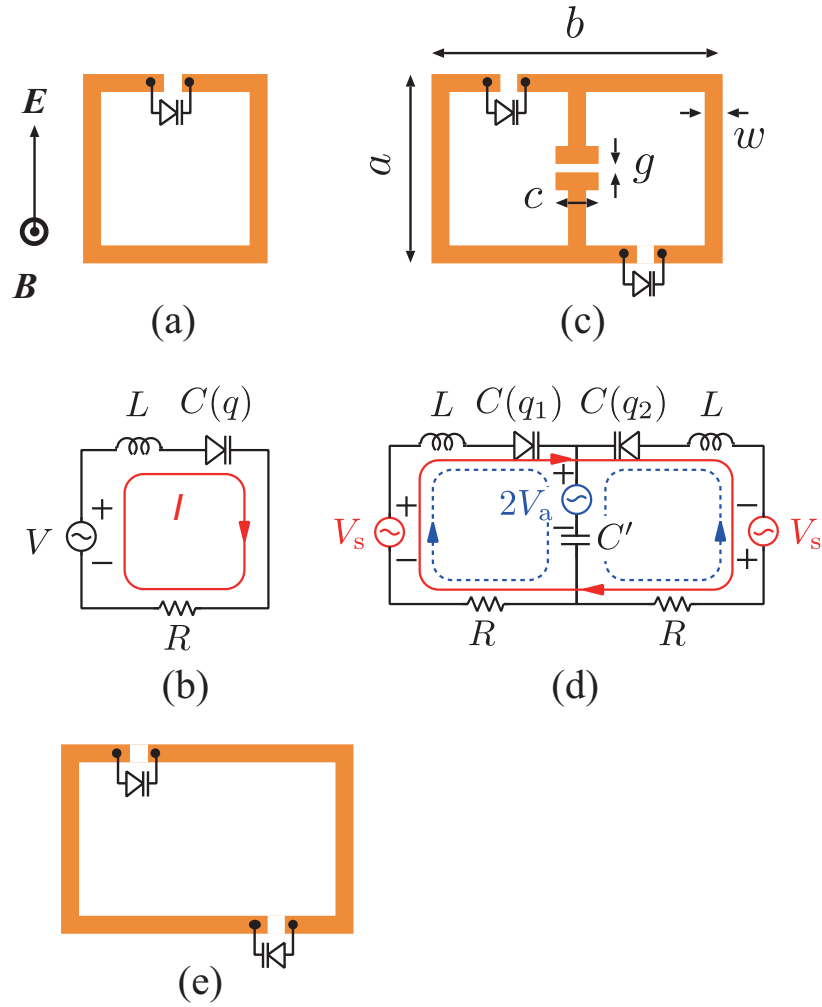


Figure 7.1: (a) Varactor-loaded split ring resonator and (b) its circuit model. (c) Coupled split ring resonator and (d) its circuit model. (e) Split ring resonator as the reference metamaterial.

where $Z(\omega) = R - i[\omega L - 1/(\omega C)]$ is the impedance of the circuit. When the circuit resonates at $\omega = \omega_0$, $|Z(\omega)|$ takes a minimum value and $|\tilde{q}(2\omega)|$ is maximized. As a result, the enhanced SH signal is radiated from the singly resonant metamaterial. Here, we can expect that $|\tilde{q}(2\omega)|$ is further enhanced by also reducing the impedance at 2ω , i.e. $|Z(2\omega)|$. This implies that more efficient SHG can be achieved when the metamaterial resonates for both the fundamental and SH frequencies.

7.1.2 Doubly resonant metamaterial

For further enhancement of the SH radiation, we introduce the CSRR shown in Fig. 7.1(c). Two ring structures share a gap with a capacitance C' at the center of the structure. Figure 7.1(d) represents the circuit model of the CSRR. It should be noted that there are two diodes oppositely directed on the outer ring. We denote the charges of the varactors as q_1 and q_2 . The equations of motions are expressed as

$$L \frac{d^2 q_1}{dt^2} + R \frac{dq_1}{dt} + \frac{q_1}{C} + \frac{q_1 - q_2}{C'} + \alpha q_1^2 = V \cos \omega t, \quad (7.3)$$

$$L \frac{d^2 q_2}{dt^2} + R \frac{dq_2}{dt} + \frac{q_2}{C} + \frac{q_2 - q_1}{C'} - \alpha q_2^2 = V \cos \omega t. \quad (7.4)$$

These equations are rewritten in different variables, $q_s = q_1 + q_2$ and $q_a = q_1 - q_2$, as follows:

$$L \frac{d^2 q_s}{dt^2} + R \frac{dq_s}{dt} + \frac{q_s}{C} + \alpha q_s q_a = 2V_s \cos \omega t, \quad (7.5)$$

$$L \frac{d^2 q_a}{dt^2} + R \frac{dq_a}{dt} + \frac{q_a}{C_a} + \frac{\alpha}{2} q_s^2 + \frac{\alpha}{2} q_a^2 = 2V_a \cos \omega t, \quad (7.6)$$

where $1/C_a = 1/C + 2/C'$. The excitation voltage V_s is induced by the magnetic flux through the rings and voltage V_a is induced by the electric field at the central gap of the structure. Equations (7.5) and (7.6) represent that the symmetric current (solid line) and anti-symmetric current (dashed line) form two resonant modes with resonant angular frequencies of $\omega_s = 1/\sqrt{LC}$ and $\omega_a = 1/\sqrt{LC_a}$, respectively; these modes are coupled through the nonlinearity α . We set the gap capacitance $C' = 2C/3$, so that the doubly resonant condition $\omega_a = 2\omega_s$ is satisfied.

We will solve q_s and q_a in the presence of a small nonlinearity α , using a perturbative approach. We assume that the solution for $\alpha = 0$ is given by $q_i^{(0)} = \tilde{q}_i^{(0)}(\omega) e^{-i\omega t} + \text{c.c.}$ ($i = s, a$). From Eqs. (7.5) and (7.6), the amplitudes of $q_s^{(0)}$ and $q_a^{(0)}$ oscillating at ω are written as $\tilde{q}_i^{(0)}(\omega) = \frac{V_i}{\omega Z_i(\omega)}$ ($i = s, a$), where $Z_s(\omega) = R - i[\omega L - 1/(\omega C)]$ and $Z_a(\omega) = R - i[\omega L - 1/(\omega C_a)]$ are the impedances for the symmetric and anti-symmetric modes, respectively. When the excitation angular frequency ω is tuned close to ω_s , $|\tilde{q}_s^{(0)}|$ becomes large due to resonance. On the other hand, the anti-symmetric mode is hardly excited; $\tilde{q}_a^{(0)} \sim 0$.

The first-order solution of q_a with respect to α satisfies

$$L \frac{d^2 q_a^{(1)}}{dt^2} + R \frac{dq_a^{(1)}}{dt} + \frac{q_a^{(1)}}{C_a} + \frac{\alpha}{2} \{q_s^{(0)}\}^2 = 0. \quad (7.7)$$

It is found that the resonant oscillation $q_s^{(0)}$ in the symmetric mode induces the SH current in the anti-symmetric mode through the last term $\frac{\alpha}{2} \{q_s^{(0)}\}^2$. The nonlinearity of the varactor results in a coupling between the two resonant modes. It should be noted that if the diodes are arranged in the same direction on the outer ring, the fundamental current and the induced SH current flow in the symmetric mode, which resonates only for the fundamental wave. From Eq. (7.7), the amplitude of the SH oscillation is obtained as

$$\tilde{q}_a(2\omega) = \frac{\alpha V_s^2}{2\omega^3 Z_a(2\omega) Z_s(\omega)^2}. \quad (7.8)$$

It is easily deduced from Eq. (7.5) that there are no SH waves in the symmetric mode. This is because the induced SH electromotive voltages in the two diodes cancel each other due to the anti-symmetric arrangements of the diodes for the symmetric mode. The SH oscillation excited only in the anti-symmetric mode forms an electric dipole with magnitude $\tilde{p} = \tilde{q}_a(2\omega)\bar{g}$, where \bar{g} is an effective dipole length and is determined by the current or charge distributions. The electric dipole oscillation contributes to efficient SH radiation. Both $|Z_s(\omega)|$ and $|Z_a(2\omega)|$ in Eq. (7.8) are small, because of the doubly resonant condition, $\omega = \omega_s = \omega_a/2$. Consequently, the amplitude of the SH oscillation can be significantly enhanced in comparison to the singly resonant metamaterial, where the SH current has to flow through the high impedance $|Z(2\omega)|$ in Eq. (7.2).

7.2 Quantum-system interpretation

In this section, we consider quantum system as shown in Fig. 7.2, which corresponds to the nonlinear metamaterial discussed in the previous section. A ladder transition, $|1\rangle \rightarrow |2\rangle \rightarrow |3\rangle$, with the separation of ω_1 is driven at the rate of Ω by two photons with the frequency of ω , which gives the detuning $\Delta_1 = \omega_1 - \omega$. We assume that the ground state $|1\rangle$ is not coupled with the excited state $|3\rangle$, but

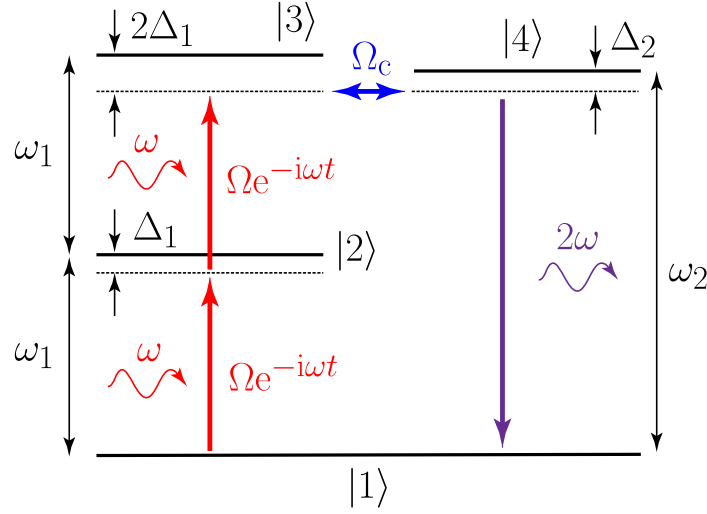


Figure 7.2: Quantum system corresponding to nonlinear metamaterial.

with another excited state $|4\rangle$, which is coupled to $|3\rangle$ with the coupling strength Ω_c . In other words, the non-radiative state $|3\rangle$ is converted into the radiative state $|4\rangle$ through the coupling Ω_c , and the quantum system radiates second harmonics into free space. The detuning between the $|4\rangle \rightarrow |1\rangle$ transition and the second harmonics is defined as $\Delta_2 = \omega_2 - 2\omega$. The Hamiltonian of the interacting quantum system is given as

$$\begin{aligned} \hat{H} = & -\frac{\hbar\Omega}{2}e^{-i\omega t}|2\rangle\langle 1| - \frac{\hbar\Omega}{2}e^{-i\omega t}|3\rangle\langle 2| - \frac{\hbar\Omega_c}{2}|4\rangle\langle 3| + \text{H.c.} \\ & + \hbar\omega_1|2\rangle\langle 2| + 2\hbar\omega_1|3\rangle\langle 3| + \hbar\omega_2|4\rangle\langle 4|. \end{aligned} \quad (7.9)$$

If the state is given by $|\psi\rangle = C_1(t)|1\rangle + C_2(t)|2\rangle + C_3(t)|3\rangle + C_4(t)|4\rangle$, quantum states evolve as follows:

$$\frac{d}{dt} \begin{pmatrix} C_1 \\ C_2 \\ C_3 \\ C_4 \end{pmatrix} = -i \begin{pmatrix} 0 & -\frac{\Omega^*}{2}e^{i\omega t} & 0 & 0 \\ -\frac{\Omega}{2}e^{-i\omega t} & \omega_1 - i\frac{\gamma_1}{2} & -\frac{\Omega^*}{2}e^{i\omega t} & 0 \\ 0 & -\frac{\Omega}{2}e^{-i\omega t} & 2\left(\omega_1 - i\frac{\gamma_1}{2}\right) & -\frac{\Omega_c^*}{2} \\ 0 & 0 & -\frac{\Omega_c}{2} & \omega_2 - i\frac{\gamma_2}{2} \end{pmatrix} \begin{pmatrix} C_1 \\ C_2 \\ C_3 \\ C_4 \end{pmatrix}. \quad (7.10)$$

In the derivation, we have already consider the relaxation effects by assuming that the decay rates of the states $|2\rangle$, $|3\rangle$, and $|4\rangle$ are given by γ_1 , $2\gamma_1$, and γ_2 , respectively.

In weak-coupling limit, we fairly assume $|C_1| (\sim 1) \gg |C_2| \gg |C_3| \gg |C_4|$, and the perturbative approach is applicable [142].

With the solution $C_1 = 1$ derived from 0-th order approximation, the motion of C_2 is written as

$$\frac{dC_2^{(1)}}{dt} = -i \left(\omega_1 - i \frac{\gamma_1}{2} \right) C_2^{(1)} + \frac{i\Omega^*}{2} e^{-i\omega t}, \quad (7.11)$$

where the superscript of C_2 represents the order of the approximation. The steady state solution can be easily obtained as

$$C_2^{(1)} = \frac{i\Omega}{2} \frac{1}{i\Delta_1 + \frac{\gamma_1}{2}} e^{-i\omega t}. \quad (7.12)$$

Using this solution, the next-order approximation yields,

$$\frac{dC_3^{(2)}}{dt} = -2i \left(\omega_1 - i \frac{\gamma_1}{2} \right) C_3^{(2)} - \left(\frac{\Omega}{2} \right)^2 \frac{1}{i\Delta_1 + \frac{\gamma_1}{2}} e^{-2i\omega t}, \quad (7.13)$$

and the steady-state solution becomes

$$C_3^{(2)} = - \left(\frac{\Omega}{2} \right)^2 \frac{1}{2 \left(i\Delta_1 + \frac{\gamma_1}{2} \right)^2} e^{-2i\omega t}. \quad (7.14)$$

With this solution, we finally obtain

$$\frac{dC_4^{(3)}}{dt} = -i \left(\omega_2 - i \frac{\gamma_2}{2} \right) C_4^{(3)} + \frac{\Omega_c}{2} \left(\frac{\Omega}{2} \right)^2 \frac{i}{2 \left(i\Delta_1 + \frac{\gamma_1}{2} \right)^2} e^{-2i\omega t}, \quad (7.15)$$

and its steady state as

$$C_4^{(3)} = \frac{\Omega_c}{2} \left(\frac{\Omega}{2} \right)^2 \frac{i}{2 \left(i\Delta_1 + \frac{\gamma_1}{2} \right)^2 \left(i\Delta_2 + \frac{\gamma_2}{2} \right)} e^{-2i\omega t}. \quad (7.16)$$

Consequently, the dipole moment d_{SHG} for SH radiation is proportional to the coherent oscillation between $|4\rangle$ and $|1\rangle$ as follows:

$$d_{\text{SHG}} \propto \frac{1}{2 \left(i\Delta_1 + \frac{\gamma_1}{2} \right)^2 \left(i\Delta_2 + \frac{\gamma_2}{2} \right)}. \quad (7.17)$$

It is quite reasonable that the SH intensity is maximized for $\omega_1 = 2\omega_2$ and $\omega = \omega_1$ ($\omega_2 = 2\omega$), i.e. $\Delta_1 = \Delta_2 = 0$, owing to double resonance.

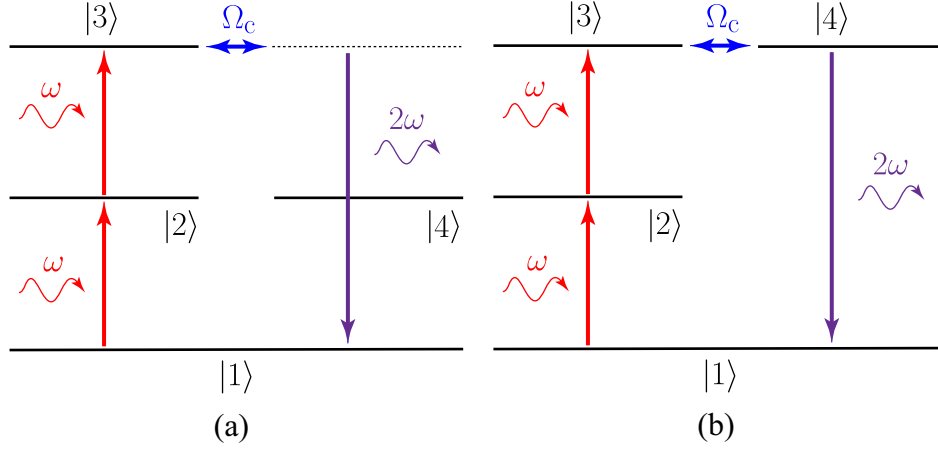


Figure 7.3: Quantum-system counterparts (a) for singly resonant metamaterial and (d) doubly resonant metamaterial.

Comparison between circuit models and quantum system In the circuit models discussed in the previous section, Eq. (7.2) under the near-resonant condition $\omega_0 \sim \omega$ for fundamental waves becomes

$$\tilde{q}(2\omega) = \frac{\alpha V_0^2}{6\omega^3 L^3} \frac{1}{\left\{i(\omega_0 - \omega) + \frac{R}{2L}\right\}^2 \left\{i(\omega_0 - 2\omega) + \frac{2R}{3L}\right\}}, \quad (7.18)$$

and Eq. (7.8) under doubly resonant condition $\omega_s \sim \omega$ and $\omega_a \sim 2\omega$ becomes

$$\tilde{q}_a(2\omega) = \frac{\alpha V_0^2}{8\omega^3 L^3} \frac{1}{\left\{i(\omega_s - \omega) + \frac{R}{2L}\right\}^2 \left\{i(\omega_a - 2\omega) + \frac{R}{2L}\right\}}. \quad (7.19)$$

It is obvious that Eq. (7.17) derived from the quantum system is written in the same form as Eq. (7.18) or Eq. (7.19) derived from the circuit models of the singly or doubly resonant metamaterials.

From Eq. (7.18), the circuit model for the singly resonant metamaterial can be identified with a quantum system as shown in Fig. 7.3(a) by assuming $\omega_2 = \omega_1 = \omega_0$, $\gamma_1 = R/(2L)$, and $\gamma_2 = 2R/(3L)$. In this case, the SH wave is emitted from a virtual level (dashed line), which is far off-resonance from the actual level $|4\rangle$, the radiation is relatively small. On the other hand, the doubly resonant metamaterial described

by Eq. (7.19) can be regarded as an analogy to another quantum system as shown in Fig. 7.3(b) for $\omega_s = \omega_1$, $\omega_a (= 2\omega_s) = \omega_2$, and $\gamma_1 = \gamma_2 = R/(2L)$. The SH radiation is enhanced owing to the resonant emission from the actual level $|4\rangle$.

It is difficult or impossible to find natural atoms with doubly resonant configuration as shown in Fig. 7.3(b), while we can freely design the doubly resonant metamaterial at any frequencies due to the scalability of the metamaterial.

7.3 Linear response

We fabricated the CSRR illustrated in Fig. 7.1(c) with $35\ \mu\text{m}$ -thick copper film on a polyphenylene ether (PPE) substrate with a thickness of $0.8\ \text{mm}$. The dimensions are $a = 14\ \text{mm}$, $b = 24\ \text{mm}$, $c = 4\ \text{mm}$, $g = 0.5\ \text{mm}$, and $w = 1\ \text{mm}$.

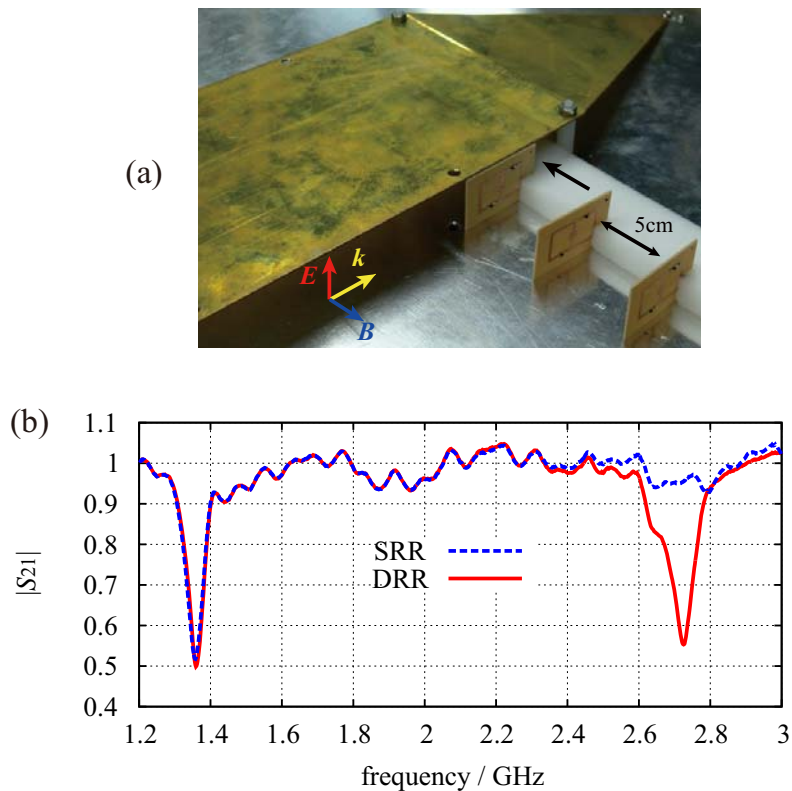


Figure 7.4: (a) Photograph of waveguide and metamaterial. (b) Transmission spectra of SRRs and CSRRs.

For comparison, we also prepared a reference metamaterial shown in Fig. 7.1(e), which has the same structure, except for the absence of the central structure and the direction of the diodes. The loop current in this structure also resonates at the same fundamental frequency as that of the CSRR, and the SH electromotive voltages generated in the two varactors contribute to the loop current, which does not resonate. Therefore, the ratio of SHG efficiency between CSRRs and SRRs can be interpreted as the enhancement factor owing to the resonance effect for the SH waves.

Before SHG demonstration, we conducted transmission measurements by a network analyzer (Advantest, R3765BG) to identify the resonant modes and resonant frequency of the metamaterials. We used the waveguide we introduced in the previous chapter as shown in Fig. 6.4(c). We placed three SRRs or CSRRs inside the waveguide at intervals of 5 cm, which is long enough to avoid the layer-to-layer coupling. Each sample was aligned as shown in Fig. 7.4(a) so that the magnetic field threads the loop and the central gap coincides with the direction of electric field. With the network analyzer, we measured the transmission amplitude S_{21} for -3 dBm input power, which is low enough to avoid resonant frequency shift induced by nonlinearity in the varactor diodes. The transmission spectra are shown in Fig. 7.4(b). There are two resonant dips at 1.36 GHz and 2.72 GHz for the CSRRs and a dip at 1.36 GHz for the SRRs. Thus, it is found that the common dips at 1.36 GHz correspond to resonance in the symmetric (or loop-current) mode and the higher resonant mode at 2.72 GHz for the CSRRs is the anti-symmetric mode. This CSRR structure satisfies the doubly resonant condition, $2\omega_s = \omega_a$.

7.4 Enhancement of second harmonic generation

Figure 7.5 shows the experimental setup to measure the SH power generated in the metamaterials. The arrangement of samples in the waveguide was same as that for the transmission measurement. A low pass filter (LPF) was used to suppress residual harmonics from the signal generator (Agilent N5183A). Two isolators were inserted at the input and output of the waveguide to suppress multiple reflections in the waveguide. The output signal containing the SH wave passes through a

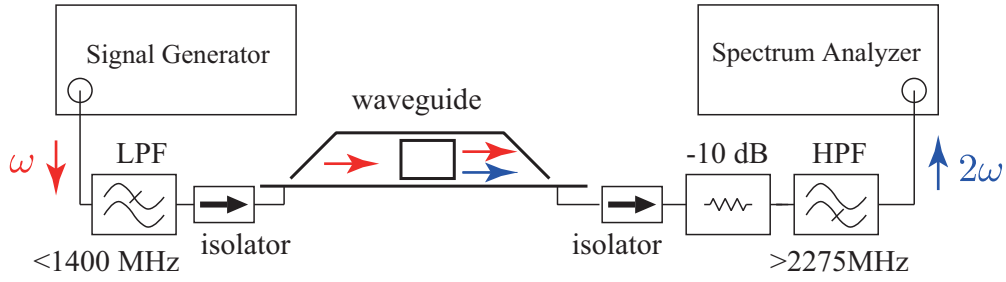


Figure 7.5: experimental setup.

high pass filter (HPF) to reject the fundamental wave and is sent to the spectrum analyzer (ADVANTEST U3751). In order to supplement the incompleteness of the isolator at the output port, we used a 10 dB attenuator, which suppresses the reflected fundamental wave from the HPF. The power spectrum of the signal after the HPF was acquired by the spectrum analyzer. While sweeping the frequency of the input signal, the power density at the SH frequency, or SHG power, was observed. Figure 7.6(a) shows the SHG power obtained for the CSRR (open circles) and SRR (filled circles) metamaterials for an input power of -3 dBm. The peaks are found around 2.7 GHz for both cases, and the peak value for the CSRRs is higher than that of the SRRs by about 20 dB. This is clear evidence that SHG in the CSRR metamaterial is significantly enhanced by the resonance at the SH frequency. As shown in Fig. 7.6(a), we fit experimental data with theoretical curves (a solid line for the CSRR and dashed line for the SRR), which can be derived from the fact that the SHG power is quadratically proportional to Eq. (7.2) for the SRR and Eq. (7.8) for the CSRR. The fitting curves reproduce the experimental results well.

Figure 7.6(b) shows the peak values of the SHG spectra for various input power levels. The open circles and filled circles correspond to the data for the CSRR and SRR, respectively. For weak input power, both SHG spectra exhibit quadratic dependence, which is represented by the solid line for the CSRRs and the dashed line for the SRRs. In this region, the second order perturbation is valid, whereas for greater input power, third-order nonlinearity should be taken into consideration. In fact, in the higher input power region, where the SHG spectra are below the solid

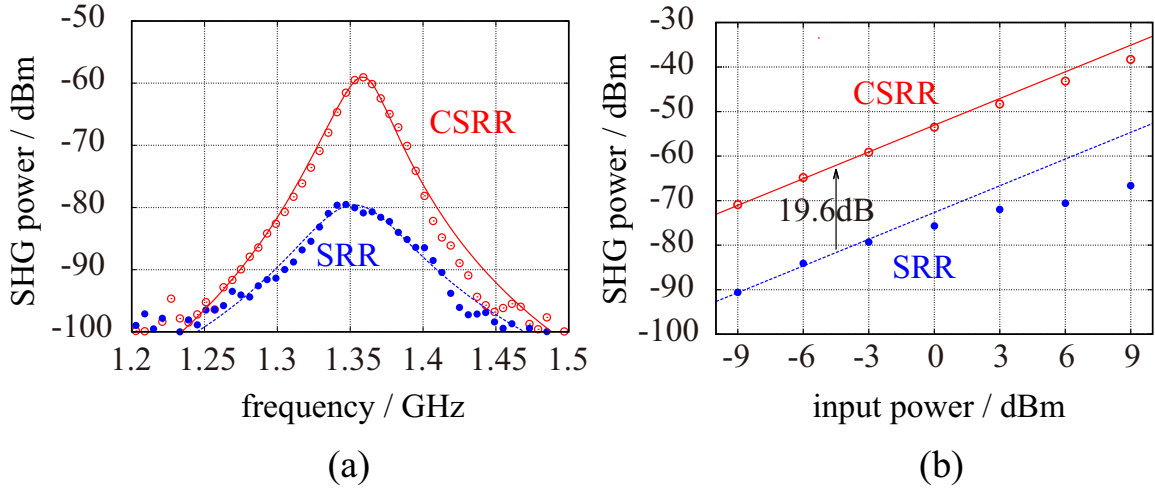


Figure 7.6: (a) SHG power for -3 dBm input. (b) SHG peak power as a function of input power.

or dashed lines, the resonance linewidth broadens and a small resonant frequency shift is observed due to the self-phase modulation. From the above reasons, it is appropriate to estimate the SHG enhancement of the CSRR for weak input power without third- or higher-order nonlinearities. The difference between the solid line and dashed line is 19.6 dB, which corresponds to the enhancement factor owing to the resonance effect for the SH wave.

As for other types of doubly resonant metamaterials, magnetically coupled split ring resonators have been theoretically analyzed [139]. Magnetically coupled cut-wire resonators has been studied and 6.6 dB enhancement of SHG has been achieved [140]. Both of the metamaterials are composite metamaterial composed of two resonant structures, a primary resonator and secondary resonator, which are magnetically coupled. The SH waves generated in the primary resonator indirectly excite the secondary resonator through magnetic coupling. Roughly speaking, the efficiency of the SHG for these metamaterials in the strong coupling limit could approach that of the CSRR metamaterial, where the SH oscillation directly excites the resonant mode owing to the arrangement of the nonlinear elements. However, it is actually difficult to attain strong magnetic coupling with finite element dimen-

sions and also difficult to optimize the parameters of the metamaterials, considering the resonant frequency shifts induced by strong coupling. The CSRR metamaterial attains a much higher enhancement factor, just by designing the structures to satisfy $\omega_a = 2\omega_s$.

7.5 Summary and discussion

In this chapter, we proposed a method to enhance SHG with CSRR metamaterial. The arrangement of the nonlinear elements induces coupling between the two resonant modes, which satisfy the doubly resonant condition. Owing to the direct excitation in the resonant mode for SH waves, we attained significant enhancement of up to two orders of magnitude.

We have not considered the phase matching condition for the SHG process because the thickness of the metamaterial is much smaller than the wavelength. We could control the linear dispersion for the fundamental wave and SH wave independently by designing the dimension of the CSRR structures and the phase matching condition would be satisfied.

Chapter 8

Summary and discussion

8.1 Summary

In this thesis, we have introduced various types of coupled-resonator-based metamaterials. All the subjects have been intensively investigated in the field of quantum or atomic physics.

In Chap. 2, we have dealt with closed quantum system, where total population is conserved, and we introduced the circuit model composed of resonators arranged in a chain as a classical model of the Schrödinger equation. It is also possible to simulate the motion of a charged particle in the presence of vector potential by using nonreciprocal elements called gyrators. There are definite relations between the quantum system and the circuit model, and quantum effects such as tunneling effect and Aharonov-Bohm effect have been demonstrated by the help of the circuit simulator.

The subject of Chaps. 3 and 4 are the control of the group velocity, i. e. superluminal and subluminal propagations, which are originally investigated in atomic systems using anomalous dispersion in a gain doublet and extremely high dispersion in an EIT window, respectively. We have proposed circuit models for baseband signals, shifting the operating frequency to zero. In Chap. 3, we have demonstrated negative delays by using the circuit model with negative slope in phase response, which corresponds to the anomalously dispersive medium. In Chap. 4, we have used cascaded all-pass filters as a normal dispersion medium, and demonstrated

slow propagation and storage of baseband signals. In both cases, the circuit models precisely reproduce the same effects as the corresponding atomic media, and conditions for superluminal propagation or the storage of the signals are also the same.

In Chaps. 5 and 6, we have focused on metamaterials that mimic EIT effects in three-level atomic system. In Chap. 5, we have introduced the metamaterial implementations from the circuit models for emulating a two-level atom with an absorption line and a three-level atom with EIT property. We have confirmed that the metamaterials respond to EM waves in exactly the same way as the corresponding atomic media, showing that electric susceptibilities are identical to each other. In Chap. 6, we have proposed a novel EIT metamaterial whose property can be dynamically controlled in order to realize the storage of EM waves. The experiment has shown that the metamaterial coherently stores and retrieves the EM waves.

Chapter 7 has introduced the doubly resonant metamaterial for the enhancement of SHG process. From the analysis of the circuit models, the doubly resonant metamaterial can be regarded as artificial four-level atoms that are designed so as to resonate for both of fundamental and second harmonic waves. The fabricated doubly resonant metamaterial loaded with varactor diodes has shown 19.6 dB enhancement in the SHG signal compared with the conventional metamaterial with a single resonant mode.

8.2 Discussion and future works

Recently more attentions have been focused on electromagnetic-wave analogy with motion of a charged particle in magnetic fields. Effective magnetic field or effective vector potential induces Lorentz force, Aharonov-Bohm effect, and one-way edge mode for electromagnetic waves with no charge [143]. In Chap. 2, we have also demonstrated Aharonov-Bohm effect in coupled LC resonators arranged in one dimension. If the network is extended to two dimensions, circular motions of a wavepacket by the effective Lorentz force could be realized. In the circuit model, the effective vector potential is represented by the gyrators, which induce unusual coupling among the resonators. The straightforward way to implement the gyrators

is to use active elements, or transistors, but operation at high frequency is difficult or impossible. Recent studies have proposed that gyrator-like coupling can be realized by magneto-optical effect [144] or three-wave mixing [143, 145], which could be realized in much higher frequency regions including optical regions. Especially the method using three-wave mixing is interesting and promising because it does not require magnetic field.* Aharonov-Bohm effect for electromagnetic waves has been demonstrated in wide spectral regions from microwave [146] to optical regions [147, 148].

We have illustrated two examples of metamaterials in analogy with multi-level atomic systems: the EIT metamaterial and doubly resonant metamaterial. The EIT metamaterial shows completely the same response to EM waves as the atomic EIT system, but they still have the advantage of scalability against the atomic EIT system whose operating frequency is uniquely determined by the atomic species. This is why various types of EIT metamaterials have been proposed and demonstrated in various frequency regions. On the other hand, the doubly resonant conditions can be hardly realized in actual four-level systems, because the transition frequency of the natural atoms cannot be freely adjusted. In that sense, the doubly resonant metamaterial can be regarded as truly artificial four-level atoms.

Finally, we consider the combination of the EIT metamaterial and doubly resonant metamaterial. Parametric amplification is one of the applications utilizing second order nonlinearity enhanced by the double resonance. In our experiment for EM storage, the storage time is limited by the decay rate in the trapped mode. Our latest study has shown that the storage time can be freely extended by parametric amplification in the presence of intense second harmonic waves, incorporating doubly resonant structures into the EIT metamaterial [149]. In addition, the parametric process, where three frequencies are mixed, implies the possibility to realize the control of EIT effects by alternating EM waves, not by applying DC bias to each element.† In fact, it can be shown from the circuit model introduced in Fig. 6.1

*It should be noted that in the method with magneto-optical effect magnetic fields affect electromagnetic waves in a quite different way from that for charged particles.

†It should be reminded that the bias voltage is applied to each element through the bias lines as shown in Fig. 6.4 (a) by feeding a DC pulse to the coaxial cable connected to the bias lines

(d) that the radiative mode and the trapped mode for our EIT metamaterial are coupled through parametric process by modulating the capacitances. We assume that it is beyond the scope of this thesis, because further investigation is required. We however believe that it would open as new way to implement *truly artificial EIT atoms*, whose properties can be controlled by auxiliary EM waves, as a complete analogy of atomic EIT effects.

Appendix A

Spice simulation for circuit models for Schrödinger equation

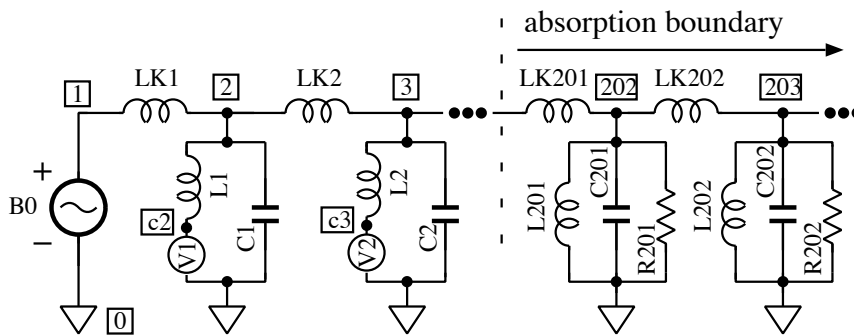


Figure A.1: Element names and node names (in boxes).

Here we present some practical tips for circuit simulation with SPICE. SPICE is the most popular circuit simulator, developed at the University of California at Berkeley. We performed all the simulations with the help of Ngspice, which is an open source software package based on Berkley's SPICE. The code we show here can work in other SPICE-based simulators with slight modifications.

In the SPICE simulation, each node should be labeled with a unique number or letters and the ground node must be numbered zero. Each element should have a unique name, whose initial letter indicates the type of element; for example, R1,

Ri, and Rout are valid for a resistor name. The circuit element beginning with letter B is a versatile voltage source whose output can be expressed as any function of voltages and currents in the circuit. Figure A.1 shows the circuit model with element names and node numbers (in boxes) for the simulation for free propagation of quantum wavepackets, which is described in section 2.4.2. The model contains a voltage source B0 for excitation of the waves, 200 lossless resonators, and 10 damped resonators, where each element is connected with a coupling inductor. We insert a dummy voltage source Vn (n= 1, 2, ... 200) into the inductor in each resonator to detect the current flowing through the inductor. The SPICE code for the simulation is shown in Fig. A.2. We give a description of SPICE usage we use in the simulation, some tricks to generate a Gaussian wavepacket, and how to print out the stored energy in each resonator as below.

In the parameter setting part, we determine six parameters: the delay time of the Gaussian pulse, $\tau = 0.02$ s; excitation frequency, $\omega = 11000$ Hz; bandwidth of the pulse, $\Delta\omega = 100$ Hz; capacitance and inductance in each resonator, $C = 10^{-6}$ μ F and $L = 10 \times 10^{-3}$ H; and coupling inductance, $K = 25 \times 10^{-3}$ H.

In the excitation part, tricks are used to generate a Gaussian wavepacket. The voltage source V0 provides a ramp signal increasing with time t between the ground (node 0) and node T, and the voltage at node T, $V(T)$, can be regarded as the time. The nonlinear voltage source B0 generates the pulse with a Gaussian function of $V(T)$, or time t .

The circuit description part expresses the elements of the Schrödinger circuit. The first five lines correspond to the circuit elements in the first resonator. For example, the first line represents the coupling inductor LK1 connecting node 1 and node 2 with a value of $K = 25$ mH with no initial current (IC=0). The voltage source V1 connecting node c2 and the ground with no voltage is placed to monitor the current flowing through the inductor L1 as $I(V1)$. The nonlinear voltage source B1 produces a voltage at node P1 expressed as $C \cdot V(2)^2/2 + L \cdot I(V1)^2/2$. Thus, we can estimate the energy stored in the first LC resonator by monitoring the output of voltage source B1 at node P1. It is easy to duplicate the same element with different numbering with the help of a scripting language like Perl.

In the analysis, we calculate the transient behaviour until 150 ms and record

```

* Schrodinger circuit / Free propagation + absorption boundary

*** parameter setting part
.PARAM tau=0.02 omega=11000 Domega=100 C=1e-6 L=10e-3 K=25e-3

*** excitation part (generation of Gaussinal wavepacket)
V0 T 0 PULSE(0 1 0 1s 0 0 1)
B0 1 0 V=exp(-((V(T)-{tau})*{Domega})^2))*sin({omega}*V(T))

*** circuit description part
* propagation domain
LK1 1 2 {K} IC=0
L1 2 c2 {L} IC=0
V1 c2 0 0C1 2 0 {C} IC=0
B1 P1 0 V={C}/2*V(2)^2 + {L}/2*I(V1)^2

LK2 2 3 {K} IC=0
L2 3 c3 {L} IC=0
V2 c3 0 0
C2 3 0 {C} IC=0
B2 P2 0 V={C}/2*V(3)^2 + {L}/2*I(V2)^2

... ( lines for n=3 ... 200 are omitted ) ...

* absorption boundary
LK201 201 202 {K} IC=0
L201 202 0 {L} IC=0
C201 202 0 {C} IC=0
R201 202 0 5000

LK202 202 203 {K} IC=0
L202 203 0 {L} IC=0
C202 203 0 {C} IC=0
R202 203 0 2500

... ( lines for n=202 ... 210 are omitted ) ...

*** analysis part
.TRAN 10u 150m UIC
.Print tran V(P1),V(P2) ... , V(P200)
.END

```

Figure A.2: Spice code for simulation of free propagation.

the voltages at P1, P2, \dots P200, which can be interpreted as the probability distribution $|u_n|^2$. We take averages of the raw data $|u_n|^2$ over a period much longer than the carrier period $2\pi/\omega_0$ as post-process to suppress the rapid oscillations.

Appendix B

Polarization in a linear dispersive medium

In this appendix we derive the relation (3.9) between the envelopes $\mathcal{E}(t)$ and $\mathcal{P}(t)$. For brevity, we omit the explicit dependence on x . For linear media, the polarization $P(t)$ induced by the electric field $E(t)$ is given by

$$P(t) = \epsilon_0 \int_{-\infty}^{\infty} \hat{\chi}(t - \tau) E(\tau) d\tau, \quad (\text{B.1})$$

where $\hat{\chi}(t)$ is a response function. The dielectric susceptibility $\chi(\omega)$ and response function $\hat{\chi}(t)$ are related through a Fourier transform:

$$\hat{\chi}(t) = \frac{1}{2\pi} \int_{-\infty}^{\infty} \chi(\omega) e^{i\omega t} d\omega. \quad (\text{B.2})$$

The realness of $\hat{\chi}(t)$ implies $\chi(-\omega) = \chi^*(\omega)$. Equation (B.1) can be Fourier-transformed as

$$\hat{P}(\omega) = \epsilon_0 \chi(\omega) \hat{E}(\omega). \quad (\text{B.3})$$

The Fourier transform of $E(t) = \mathcal{E}(t) e^{i\omega_0 t} + \text{c.c.}$ can be expressed as

$$\begin{aligned} \hat{E}(\omega) &= \int_{-\infty}^{\infty} \mathcal{E}(t) e^{i\omega_0 t} e^{-i\omega t} dt + \int_{-\infty}^{\infty} \mathcal{E}^*(t) e^{-i\omega_0 t} e^{-i\omega t} dt \\ &= \hat{\mathcal{E}}(\omega - \omega_0) + \hat{\mathcal{E}}^*(-\omega - \omega_0), \end{aligned} \quad (\text{B.4})$$

in terms of the Fourier transform of the envelope:

$$\hat{\mathcal{E}}(\Omega) = \int_{-\infty}^{\infty} \mathcal{E}(t) e^{-i\Omega t} dt. \quad (\text{B.5})$$

Assuming that the spectrum of the electric field is restricted around $\pm\omega_0$, we can use the Taylor expansion of the susceptibility $\chi(\omega)$:

$$\chi(\omega) \simeq \chi_0 + \chi_1(|\omega| - \omega_0), \quad (\text{B.6})$$

where $\chi_0 \equiv \chi(\omega_0)$, $\chi_1 \equiv d\chi/d\omega(\omega_0)$. When the losses in the medium are negligible, the susceptibility is real and must be symmetric; $\chi(-\omega) = \chi(\omega)$. From Eqs. (B.3), (B.4), and (B.6), we have

$$\begin{aligned} \hat{P}(\omega) &\simeq \epsilon_0 \chi_0 \hat{\mathcal{E}}(\omega - \omega_0) + \epsilon_0 \chi_1 (\omega - \omega_0) \hat{\mathcal{E}}(\omega - \omega_0) \\ &\quad + \epsilon_0 \chi_0 \hat{\mathcal{E}}^*(-\omega - \omega_0) + \epsilon_0 \chi_1 (-\omega - \omega_0) \hat{\mathcal{E}}^*(-\omega - \omega_0). \end{aligned} \quad (\text{B.7})$$

The inverse Fourier transform yields

$$\begin{aligned} P(t) &= \epsilon_0 \left(\chi_0 \mathcal{E}(t) e^{i\omega_0 t} - i\chi_1 \frac{d\mathcal{E}}{dt} e^{i\omega_0 t} \right) + \text{c.c.} \\ &= \mathcal{P}(t) e^{i\omega_0 t} + \text{c.c.}, \end{aligned} \quad (\text{B.8})$$

where we used,

$$\mathcal{E}(t) = \frac{1}{2\pi} \int_{-\infty}^{\infty} \hat{\mathcal{E}}(\Omega) e^{i\Omega t} d\Omega, \quad \frac{d}{dt} \mathcal{E}(t) = \frac{1}{2\pi} \int_{-\infty}^{\infty} (i\Omega) \hat{\mathcal{E}}(\Omega) e^{i\Omega t} d\Omega. \quad (\text{B.9})$$

Now we have Eq. (3.9):

$$\mathcal{P}(t) = \epsilon_0 \left(\chi_0 - i\chi_1 \frac{d}{dt} \right) \mathcal{E}(t). \quad (\text{B.10})$$

Note that only the second term contributes to the group velocity in the derivation of Eq. (3.12).

Acknowledgments

I wish to express sincere gratitude to Professor Masao Kitano for his continuous guidance and encouragement with patience as my supervisor, since I joined the Kitano laboratory in the department of Electronic Science and Engineering at Kyoto University. I also would like to appreciate Associate Professor Kazuhiko Sugiyama at Kyoto University for his supports and helpful comments.

I would like to thank to all the current and former members of the Kitano laboratory. Most of the ideas in this dissertation were brought up through the discussions with them. I wish to give special thanks to Dr. Keisaku Yamane for his kind instructions on the basic techniques of optical experiments. I would like to appreciate Dr. Hirokazu Kobayashi, Dr. Suhei Tamate, and Dr. Kazuhisa Ogawa for helpful comments and discussions in the field of quantum optics. I wish to thank to Dr. Yasuhiro Tamayama, Dr. Yosuke Nakata, and Mr. Yoshiro Urade for the collaborations in metamaterial research. Some essential ideas were inspired through the discussions with them. I am especially grateful for the official assistance given by Ms. Hisako Sekiguchi, Ms. Keiko Yamada, and Ms. Reiko Nakanishi.

The works in this dissertation were financially supported by JSPS KAKENHI (Grants No. 22560041, No. 22109004, No. 25790065, and No. 25287101) and The Murata Science Foundation.

Finally, I would like to express deepest gratitude to my parents and my sister for their support and encouragement.

References

- [1] W. Rotman, "Plasma simulation by artificial dielectrics and parallel-plate media," *IRE Trans. Antennas. Propag.* **10**, 82 (1962).
- [2] M. O. Oktel and O. E. Müstecaplıoğlu, "Electromagnetically induced left-handedness in a dense gas of three-level atoms," *Phys. Rev. A* **70**, 053806 (2004).
- [3] Q. Thommen and P. Mandel, "Electromagnetically Induced Left Handedness in Optically Excited Four-Level Atomic Media," *Phys. Rev. Lett.* **96**, 053601 (2006).
- [4] C. M. Krowne and J. Q. Shen, "Dressed-state mixed-parity transitions for realizing negative refractive index," *Phys. Rev. A* **79**, 023818 (2009).
- [5] J. B. Pendry, A. J. Holden, D. J. Robbins, and W. J. Stewart, "Magnetism from conductors and enhanced nonlinear phenomena," *IEEE Trans. Microwave Theory Tech.* **47**, 2075 (1999).
- [6] B.-I. Popa and S. A. Cummer, "Compact dielectric particles as a building block for low-loss magnetic metamaterials," *Phys. Rev. Lett.* **100**, 207401 (2008).
- [7] Q. Zhao, L. Kang, B. Du, H. Zhao, Q. Xie, X. Huang, B. Li, J. Zhou, and L. Li, "Experimental demonstration of isotropic negative permeability in a three-dimensional dielectric composite," *Phys. Rev. Lett.* **101**, 027402 (2008).
- [8] W. J. Padilla, A. J. Taylor, and R. D. Averitt, "Dynamical Electric and Magnetic Metamaterial Response at Terahertz Frequencies," *Phys. Rev. Lett.* **96**, 107401 (2006).
- [9] S. Tretyakov, F. Mariotte, C. Simovski, T. Kharina, and J.-P. Heliot, "Analytical antenna model for chiral scatterers: comparison with numerical and experimental data," *IEEE Trans. Antennas. Propag.* **44**, 1006 (1996).
- [10] M. Kuwata-Gonokami, N. Saito, Y. Ino, M. Kauranen, K. Jefimovs, T. Vallius, J. Turunen, and Y. Svirko, "Giant optical activity in quasi-two-dimensional planar nanostructures," *Phys. Rev. Lett.* **95**, 227401 (2005).
- [11] Y. Tamayama, T. Nakanishi, K. Sugiyama, and M. Kitano, "Observation of Brewster's effect for transverse-electric electromagnetic waves in metamaterials: Experiment and theory," *Phys. Rev. B* **73**, 193104 (2006).
- [12] Y. Tamayama, T. Nakanishi, K. Sugiyama, and M. Kitano, "An invisible medium for circularly polarized electromagnetic waves," *Opt. Express* **16**, 20869 (2008).
- [13] V. Veselago, "The Electrodynamics of Substances with Simultaneously Negative Values of ϵ and μ ," *Sov. Phys. Usp.* **10**, 509 (1968).
- [14] <http://www.povray.org/>.
- [15] G. Dolling, M. Wegener, S. Linden, and C. Hormann, "Photorealistic images of objects in effective negative-index materials," *Opt. Express* **14**, 1842 (2006).
- [16] R. A. Shelby, D. R. Smith, and S. Schultz, "Experimental verification of a negative index of refraction," *Science* **292**, 77 (2001).
- [17] J. Valentine, S. Zhang, T. Zentgraf, E. Ulin-Avila, D. A. Genov, G. Bartal, and X. Zhang, "Three-dimensional optical metamaterial with a negative refractive index," *Nature* **455**, 376 (2008).
- [18] J. B. Pendry, "Negative Refraction Makes a Perfect Lens," *Phys. Rev. Lett.* **85**, 3966 (2000).

- [19] L. Solymar and E. Shamonina, *Waves in Metamaterials* (Oxford Press, New York, 2009).
- [20] A. Lagarkov and V. Kissel, "Near-Perfect Imaging in a Focusing System Based on a Left-Handed-Material Plate," *Phys. Rev. Lett.* **92**, 077401 (2004).
- [21] D. O. S. Melville and R. J. Blaikie, "Super-resolution imaging through a planar silver layer," *Opt. Express* **13**, 2127 (2005).
- [22] N. Fang, H. Lee, C. Sun, and X. Zhang, "Sub-diffraction-limited optical imaging with a silver superlens," *Science* **308**, 534 (2005).
- [23] J. B. Pendry, D. Schurig, and D. R. Smith, "Controlling electromagnetic fields," *Science* **312**, 1780 (2006).
- [24] U. Leonhardt, "Optical conformal mapping," *Science* **312**, 1777 (2006).
- [25] L. Zhang, M. Yan, and M. Qiu, "The effect of transformation order on the invisibility performance of a practical cylindrical cloak," *J. Opt. A* **10**, 095001 (2008).
- [26] D. Schurig, J. J. Mock, B. J. Justice, S. A. Cummer, J. B. Pendry, A. F. Starr, and D. R. Smith, "Metamaterial electromagnetic cloak at microwave frequencies," *Science* **314**, 977 (2006).
- [27] J. Li and J. B. Pendry, "Hiding under the Carpet: A New Strategy for Cloaking," *Phys. Rev. Lett.* **101**, 203901 (2008).
- [28] N. Liu, L. Langguth, T. Weiss, J. Kästel, M. Fleischhauer, T. Pfau, and H. Giessen, "Plasmonic analogue of electromagnetically induced transparency at the Drude damping limit," *Nat. Mater.* **8**, 758 (2009).
- [29] J. Valentine, J. Li, T. Zentgraf, G. Bartal, and X. Zhang, "An optical cloak made of dielectrics," *Nat. Mater.* **8**, 568 (2009).
- [30] U. Leonhardt and T. Philbin, *Geometry of Light: The Science of INVISIBILITY* (Dover Publications, New York, 2010).
- [31] H. Chen, C. T. Chan, and P. Sheng, "Transformation optics and metamaterials," *Nat. Mater.* **9**, 387 (2010).
- [32] G. Eleftheriades, A. Iyer, and P. Kremer, "Planar negative refractive index media using periodically L-C loaded transmission lines," *IEEE Trans. Microw. Theory Tech.* **50**, 2702 (2002).
- [33] A. Sanada, C. Caloz, and T. Itoh, "Characteristics of the composite right/left-handed transmission lines," *IEEE Microw. Wirel. Components Lett.* **14**, 68 (2004).
- [34] A. Sanada, C. Caloz, and T. Itoh, "Planar Distributed Structures With Negative Refractive Index," *IEEE Trans. Microw. Theory Tech.* **52**, 1252 (2004).
- [35] A. Lai, T. Itoh, and C. Caloz, "Composite right/left-handed transmission line metamaterials," *IEEE Microwave Magazine* **5**, 34 (2004).
- [36] A. Grbic and G. Eleftheriades, "Overcoming the Diffraction Limit with a Planar Left-Handed Transmission-Line Lens," *Phys. Rev. Lett.* **92**, 117403 (2004).
- [37] E. Prodan, C. Radloff, N. J. Halas, and P. Nordlander, "A hybridization model for the plasmon response of complex nanostructures," *Science* **302**, 419 (2003).
- [38] N. Liu, H. Liu, S. Zhu, and H. Giessen, "Stereometamaterials," *Nat. Photonics* **3**, 157 (2009).

-
- [39] C.-W. Chang, M. Liu, S. Nam, S. Zhang, Y. Liu, G. Bartal, and X. Zhang, “Optical Möbius symmetry in metamaterials,” *Phys. Rev. Lett.* **105**, 235501 (2010).
- [40] Y. Tamayama, K. Yasui, T. Nakanishi, and M. Kitano, “Electromagnetically induced transparency like transmission in a metamaterial composed of cut-wire pairs with indirect coupling,” *Phys. Rev. B* **89**, 075120 (2014).
- [41] E. Shamonina, V. Kalinin, K. Ringhofer, and L. Solymar, “Magneto-inductive waveguide,” *Electron. Lett.* **38**, 371 (2002).
- [42] H. Liu, D. Genov, D. Wu, Y. Liu, J. Steele, C. Sun, S. Zhu, and X. Zhang, “Magnetic Plasmon Propagation Along a Chain of Connected Subwavelength Resonators at Infrared Frequencies,” *Phys. Rev. Lett.* **97**, 243902 (2006).
- [43] C. Zhu, H. Liu, S. M. Wang, T. Li, J. X. Cao, Y. J. Zheng, L. Li, Y. Wang, S. N. Zhu, and X. Zhang, “Electric and magnetic excitation of coherent magnetic plasmon waves in a one-dimensional meta-chain,” *Opt. Express* **18**, 26268 (2010).
- [44] T. Li, R. X. Ye, C. Li, H. Liu, S. M. Wang, J. X. Cao, S. N. Zhu, and X. Zhang, “Structural-configured magnetic plasmon bands in connected ring chains,” *Opt. Express* **17**, 11486 (2009).
- [45] Y. Nakata, T. Okada, T. Nakanishi, and M. Kitano, “Observation of flat band for terahertz spoof plasmons in a metallic kagomé lattice,” *Phys. Rev. B* **85**, 205128 (2012).
- [46] Y. Nakata, T. Okada, T. Nakanishi, and M. Kitano, “Circuit model for hybridization modes in metamaterials and its analogy to the quantum tight-binding model,” *Phys. Status Solidi* **249**, 2293 (2012).
- [47] K. Sakoda, “Dirac cone in two- and three-dimensional metamaterials,” *Opt. Express* **20**, 3898 (2012).
- [48] M. Kitano, Y. Tamayama, and T. Nakanishi, “Coupled-resonator-based metamaterials,” *IEICE Electron. Express* **9**, 51 (2012).
- [49] W. Frank and P. Brentano, “Classical analogy to quantum mechanical level repulsion,” *Am. J. Phys.* **62**, 706 (1994).
- [50] P. R. Hemmer and M. G. Prentiss, “Coupled-pendulum model of the stimulated resonance Raman effect,” *J. Opt. Soc. Am. B* **5**, 1613 (1988).
- [51] M. Frimmer and L. Novotny, “The classical Bloch equations,” *Am. J. Phys.* **82**, 947 (2014).
- [52] B. D. H. Tellegen, “The gyrator, a new electric network element,” *Philips Res. Rept.* **3**, 388 (1948).
- [53] U. Tietze and C. Schenk, *Electronic circuits, Design and applications* (Springer-Verlag, Berlin, 1991).
- [54] A. Figotin and I. Vitebsky, “Spectra of periodic nonreciprocal electric circuits,” *SIAM J. Appl. Math.* **61**, 2008 (2001).
- [55] H. J. Cardin and A. B. Giordano, *Network theory, An introduction to reciprocal and nonreciprocal circuits* (Prentice-Hall, New Jersey, 1964).
- [56] A. Yariv, *Optical electronics in modern communications* (Oxford University Press, New York, 1997).
- [57] J. L. Rosner, “Tabletop time-reversal violation,” *Am. J. Phys.* **64**, 982 (1996).

- [58] L. E. Ballentine, *Quantum mechanics - A modern development* (World Scientific, Singapore, 1998).
- [59] <http://ngspice.sourceforge.net/>.
- [60] M. L. Bellac, *Quantum physics* (Cambridge University Press, Cambridge, 2006).
- [61] N. Marinescu, "The use of quantum mechanics in the treatment of waveguides," *Prog. Quant. Electr.* **16**, 183 (1992).
- [62] W. Greiner, *Relativistic quantum mechanics - Wave equations* (Springer-Verlag, Berlin, 2000).
- [63] L. Brillouin, *Wave Propagation and Group Velocity* (Academic Press, New York, 1960).
- [64] S. Chu and S. Wong, "Linear pulse propagation in an absorbing medium," *Phys. Rev. Lett.* **48**, 738 (1982).
- [65] L. Wang, A. Kuzmich, and A. Dogariu, "Gain-assisted superluminal light propagation," *Nature* **406**, 277 (2000).
- [66] A. Dogariu, A. Kuzmich, and L. J. Wang, "Transparent anomalous dispersion and superluminal light-pulse propagation at a negative group velocity," *Phys. Rev. A* **63**, 053806 (2001).
- [67] T. Nakanishi, K. Sugiyama, and M. Kitano, "Demonstration of negative group delays in a simple electronic circuit," *Am. J. Phys.* **70**, 1117 (2002).
- [68] M. Kitano, T. Nakanishi, and K. Sugiyama, "Negative group delay and superluminal propagation: an electronic circuit approach," *IEEE J. Sel. Top. Quantum Electron.* **9**, 43 (2003).
- [69] M. Scully and M. Zubairy, *Quantum optics* (Cambridge University Press, Cambridge, 1997).
- [70] M. Tanaka, M. Fujiwara, and H. Ikegami, "Propagation of a gaussian wave packet in an absorbing medium," *Phys. Rev. A* **34**, 4851 (1986).
- [71] S. Harris, "Electromagnetically Induced Transparency," *Phys. Today* **50**, 36 (1997).
- [72] L. V. Hau, S. E. Harris, Z. Dutton, and C. H. Behroozi, "Light speed reduction to 17 metres per second in an ultracold atomic gas," *Nature* **397**, 594 (1999).
- [73] M. Fleischhauer and M. Lukin, "Dark-state polaritons in electromagnetically induced transparency," *Phys. Rev. Lett.* **84**, 5094 (2000).
- [74] M. Fleischhauer and M. Lukin, "Quantum memory for photons: Dark-state polaritons," *Phys. Rev. A* **65**, 022314 (2002).
- [75] M. D. Lukin, "Colloquium: Trapping and manipulating photon states in atomic ensembles," *Rev. Mod. Phys.* **75**, 457 (2003).
- [76] U. Leonhardt, "A laboratory analogue of the event horizon using slow light in an atomic medium," *Nature* **415**, 406 (2002).
- [77] C. L. Garrido Alzar, M. A. G. Martinez, and P. Nussenzveig, "Classical analog of electromagnetically induced transparency," *Am. J. Phys.* **70**, 37 (2002).
- [78] V. A. Fedotov, M. Rose, S. L. Prosvirnin, N. Papasimakis, and N. I. Zheludev, "Sharp trapped-mode resonances in planar metamaterials with a broken structural symmetry," *Phys. Rev. Lett.* **99**, 147401 (2007).

-
- [79] S. Zhang, D. A. Genov, Y. Wang, M. Liu, and X. Zhang, "Plasmon-induced transparency in metamaterials," *Phys. Rev. Lett.* **101**, 47401 (2008).
- [80] N. Papasimakis, V. A. Fedotov, N. I. Zheludev, and S. L. Prosvirnin, "Metamaterial analog of electromagnetically induced transparency," *Phys. Rev. Lett.* **101**, 253903 (2008).
- [81] S.-Y. Chiam, R. Singh, C. Rockstuhl, F. Lederer, W. Zhang, and A. Bettiol, "Analogue of electromagnetically induced transparency in a terahertz metamaterial," *Phys. Rev. B* **80**, 153103 (2009).
- [82] Z.-G. Dong, H. Liu, J.-X. Cao, T. Li, S.-M. Wang, S.-N. Zhu, and X. Zhang, "Enhanced sensing performance by the plasmonic analog of electromagnetically induced transparency in active metamaterials," *Appl. Phys. Lett.* **97**, 114101 (2010).
- [83] J. Zhang, S. Xiao, C. Jeppesen, A. Kristensen, and N. A. Mortensen, "Electromagnetically induced transparency in metamaterials at near-infrared frequency," *Opt. Express* **18**, 17187 (2010).
- [84] B. Luk'yanchuk, N. I. Zheludev, S. A. Maier, N. J. Halas, P. Nordlander, H. Giessen, and C. T. Chong, "The Fano resonance in plasmonic nanostructures and metamaterials," *Nat. Mater.* **9**, 707 (2010).
- [85] Y. Tamayama, T. Nakanishi, Y. Wakasa, T. Kanazawa, K. Sugiyama, and M. Kitano, "Electromagnetic response of a metamaterial with field-gradient-induced transparency," *Phys. Rev. B* **82**, 165130 (2010).
- [86] C. Kurter, P. Tassin, L. Zhang, T. Koschny, A. Zhuravel, A. Ustinov, S. Anlage, and C. Soukoulis, "Classical Analogue of Electromagnetically Induced Transparency with a Metal-Superconductor Hybrid Metamaterial," *Phys. Rev. Lett.* **107**, 043901 (2011).
- [87] W. Huang, Q. Wang, X. Yin, C. Huang, H. Huang, Y. Wang, and Y. Zhu, "Optical resonances in a composite asymmetric plasmonic nanostructure," *J. Appl. Phys.* **109**, 114310 (2011).
- [88] M. Kang, H.-X. Cui, Y. Li, B. Gu, J. Chen, and H.-T. Wang, "Fano-Feshbach resonance in structural symmetry broken metamaterials," *J. Appl. Phys.* **109**, 014901 (2011).
- [89] Z. Li, Y. Ma, R. Huang, R. Singh, J. Gu, J. Han, and W. Zhang, "Manipulating the plasmon-induced transparency in terahertz metamaterials," *Opt. Express* **19**, 37 (2011).
- [90] R. Singh, I. A. I. Al-Naib, Y. Yang, D. Roy Chowdhury, W. Cao, C. Rockstuhl, T. Ozaki, R. Morandotti, and W. Zhang, "Observing metamaterial induced transparency in individual Fano resonators with broken symmetry," *Appl. Phys. Lett.* **99**, 201107 (2011).
- [91] X. Liu, J. Gu, R. Singh, Y. Ma, J. Zhu, Z. Tian, M. He, J. Han, and W. Zhang, "Electromagnetically induced transparency in terahertz plasmonic metamaterials via dual excitation pathways of the dark mode," *Appl. Phys. Lett.* **100**, 131101 (2012).
- [92] S. Zhang, Z. Ye, Y. Wang, Y. Park, G. Bartal, M. Mrejen, X. Yin, and X. Zhang, "Anti-Hermitian Plasmon Coupling of an Array of Gold Thin-Film Antennas for Controlling Light at the Nanoscale," *Phys. Rev. Lett.* **109**, 193902 (2012).
- [93] X.-R. Jin, Y. Lu, J. Park, H. Zheng, F. Gao, Y. Lee, J. Yull Rhee, K. Won Kim, H. Cheong, and W. H. Jang, "Manipulation of electromagnetically-induced trans-

- parency in planar metamaterials based on phase coupling,” *J. Appl. Phys.* **111**, 073101 (2012).
- [94] Y. Tamayama, T. Nakanishi, and M. Kitano, “Variable group delay in a metamaterial with field-gradient-induced transparency,” *Phys. Rev. B* **85**, 073102 (2012).
- [95] J. Gu, R. Singh, X. Liu, X. Zhang, Y. Ma, S. Zhang, S. A. Maier, Z. Tian, A. K. Azad, H.-T. Chen, et al., “Active control of electromagnetically induced transparency analogue in terahertz metamaterials,” *Nat. Commun.* **3**, 1151 (2012).
- [96] Y. Sun, Y.-w. Tong, C.-h. Xue, Y.-q. Ding, Y.-h. Li, H. Jiang, and H. Chen, “Electromagnetic diode based on nonlinear electromagnetically induced transparency in metamaterials,” *Appl. Phys. Lett.* **103**, 091904 (2013).
- [97] F. Miyamaru, H. Morita, Y. Nishiyama, T. Nishida, T. Nakanishi, M. Kitano, and M. W. Takeda, “Ultrafast optical control of group delay of narrow-band terahertz waves,” *Sci. Rep.* **4**, 4346 (2014).
- [98] M. Lapine, I. V. Shadrivov, and Y. S. Kivshar, “Colloquium: Nonlinear metamaterials,” *Rev. Mod. Phys.* **86**, 1093 (2014).
- [99] I. V. Shadrivov, S. K. Morrison, and Y. S. Kivshar, “Tunable split-ring resonators for nonlinear negative-index metamaterials,” *Opt. Express* **14**, 9344 (2006).
- [100] I. V. Shadrivov, A. B. Kozyrev, D. W. van der Weide, and Y. S. Kivshar, “Tunable transmission and harmonic generation in nonlinear metamaterials,” *Appl. Phys. Lett.* **93**, 161903 (2008).
- [101] B. Wang, J. Zhou, T. Koschny, and C. M. Soukoulis, “Nonlinear properties of split-ring resonators,” *Opt. Express* **16**, 16058 (2008).
- [102] D. A. Powell, I. V. Shadrivov, and Y. S. Kivshar, “Nonlinear electric metamaterials,” *Appl. Phys. Lett.* **95**, 084102 (2009).
- [103] A. R. Katko, J. P. Barrett, and S. A. Cummer, “Time-varying transistor-based metamaterial for tunability, mixing, and efficient phase conjugation,” *J. Appl. Phys.* **115**, 144501 (2014).
- [104] A. M. Zagoskin, *Quantum Engineering* (Cambridge University Press, New York, 2011).
- [105] M. Trepanier, D. Zhang, O. Mukhanov, and S. Anlage, “Realization and Modeling of Metamaterials Made of rf Superconducting Quantum-Interference Devices,” *Phys. Rev. X* **3**, 041029 (2013).
- [106] I. V. Shadrivov, P. V. Kapitanova, S. I. Maslovski, and Y. S. Kivshar, “Metamaterials Controlled with Light,” *Phys. Rev. Lett.* **109**, 083902 (2012).
- [107] A. P. Slobozhanyuk, P. V. Kapitanova, D. S. Filonov, D. A. Powell, I. V. Shadrivov, M. Lapine, P. A. Belov, R. C. McPhedran, and Y. S. Kivshar, “Nonlinear interaction of meta-atoms through optical coupling,” *Appl. Phys. Lett.* **104**, 014104 (2014).
- [108] D. Roy Chowdhury, R. Singh, J. F. O’Hara, H.-T. Chen, A. J. Taylor, and A. K. Azad, “Dynamically reconfigurable terahertz metamaterial through photo-doped semiconductor,” *Appl. Phys. Lett.* **99**, 231101 (2011).
- [109] M. Liu, H. Y. Hwang, H. Tao, A. C. Strikwerda, K. Fan, G. R. Keiser, A. J. Sternbach, K. G. West, S. Kittiwatanakul, J. Lu, et al., “Terahertz-field-induced insulator-to-metal transition in vanadium dioxide metamaterial,” *Nature* **487**, 345 (2012).

-
- [110] A. E. Nikolaenko, F. De Angelis, S. a. Boden, N. Papasimakis, P. Ashburn, E. Di Fabrizio, and N. I. Zheludev, “Carbon Nanotubes in a Photonic Metamaterial,” *Phys. Rev. Lett.* **104**, 153902 (2010).
- [111] A. E. Nikolaenko, N. Papasimakis, E. Atmatzakis, Z. Luo, Z. X. Shen, F. De Angelis, S. a. Boden, E. Di Fabrizio, and N. I. Zheludev, “Nonlinear graphene metamaterial,” *Appl. Phys. Lett.* **100**, 181109 (2012).
- [112] A. Minovich, J. Farnell, D. N. Neshev, I. McKerracher, F. Karouta, J. Tian, D. A. Powell, I. V. Shadrivov, H. Hoe Tan, C. Jagadish, et al., “Liquid crystal based nonlinear fishnet metamaterials,” *Appl. Phys. Lett.* **100**, 121113 (2012).
- [113] M. Lapine, I. V. Shadrivov, D. A. Powell, and Y. S. Kivshar, “Magnetoelastic metamaterials,” *Nat. Mater.* **11**, 30 (2012).
- [114] M. Liu, D. A. Powell, I. V. Shadrivov, M. Lapine, and Y. S. Kivshar, “Spontaneous chiral symmetry breaking in metamaterials,” *Nat. Commun.* **5**, 4441 (2014).
- [115] O. Sakai, “Transition between positive and negative permittivity in field-dependent metamaterial,” *J. Appl. Phys.* **109**, 084914 (2011).
- [116] O. Sakai and K. Tachibana, “Plasmas as metamaterials: a review,” *Plasma Sources Sci. Technol.* **21**, 013001 (2012).
- [117] H. Tao, A. Strikwerda, K. Fan, W. Padilla, X. Zhang, and R. Averitt, “Reconfigurable Terahertz Metamaterials,” *Phys. Rev. Lett.* **103**, 147401 (2009).
- [118] W. M. Zhu, A. Q. Liu, X. M. Zhang, D. P. Tsai, T. Bourouina, J. H. Teng, X. H. Zhang, H. C. Guo, H. Tanoto, T. Mei, et al., “Switchable magnetic metamaterials using micromachining processes,” *Adv. Mater.* **23**, 1792 (2011).
- [119] Y. H. Fu, A. Q. Liu, W. M. Zhu, X. M. Zhang, D. P. Tsai, J. B. Zhang, T. Mei, J. F. Tao, H. C. Guo, X. H. Zhang, et al., “A Micromachined Reconfigurable Metamaterial via Reconfiguration of Asymmetric Split-Ring Resonators,” *Adv. Funct. Mater.* **21**, 3589 (2011).
- [120] T. Nakanishi, T. Otani, Y. Tamayama, and M. Kitano, “Storage of electromagnetic waves in a metamaterial that mimics electromagnetically induced transparency,” *Phys. Rev. B* **87**, 161110 (2013).
- [121] R. E. Collin, *Field theory of guided waves* (IEEE Press, New York, 1991).
- [122] E. Poutrina, D. Huang, and D. R. Smith, “Analysis of nonlinear electromagnetic metamaterials,” *New J. Phys.* **12**, 093010 (2010).
- [123] V. A. Fedotov, A. V. Rogacheva, V. Savinov, D. P. Tsai, and N. I. Zheludev, “Resonant transparency and non-trivial non-radiating excitations in toroidal metamaterials,” *Sci. Rep.* **3**, 2967 (2013).
- [124] Y. Yang, I. I. Kravchenko, D. P. Briggs, and J. Valentine, “All-dielectric metasurface analogue of electromagnetically induced transparency,” *Nat. Commun.* **5**, 5753 (2014).
- [125] I. V. Shadrivov, M. Lapine, and Y. S. Kivshar, *Nonlinear, Tunable and Active Metamaterials* (Springer-Verlag, Berlin, 2014).
- [126] D. Huang, A. Rose, E. Poutrina, S. Larouche, and D. R. Smith, “Wave mixing in nonlinear magnetic metacrystal,” *Appl. Phys. Lett.* **98**, 204102 (2011).
- [127] A. R. Katko, G. Shvets, and S. A. Cummer, “Phase conjugation metamaterials: particle design and imaging experiments,” *J. Opt.* **14**, 114003 (2012).

- [128] H. Suchowski, K. O'Brien, Z. J. Wong, A. Salandrino, X. Yin, and X. Zhang, "Phase mismatch-free nonlinear propagation in optical zero-index materials," *Science* **342**, 1223 (2013).
- [129] Z. Wang, Y. Luo, T. Jiang, Z. Wang, J. Huangfu, and L. Ran, "Harmonic Image Reconstruction Assisted by a Nonlinear Metmaterial Surface," *Phys. Rev. Lett.* **106**, 047402 (2011).
- [130] Y. Tamayama, T. Nakanishi, and M. Kitano, "Observation of modulation instability in a nonlinear magnetoinductive waveguide," *Phys. Rev. B* **87**, 195123 (2013).
- [131] R. Yang and I. V. Shadrivov, "Double-nonlinear metamaterials," *Appl. Phys. Lett.* **97**, 231114 (2010).
- [132] P.-Y. Chen, M. Farhat, and A. Alù, "Bistable and Self-Tunable Negative-Index Metamaterial at Optical Frequencies," *Phys. Rev. Lett.* **106**, 105503 (2011).
- [133] M. Liu, D. A. Powell, I. V. Shadrivov, M. Lapine, and Y. S. Kivshar, "Spontaneous chiral symmetry breaking in metamaterials," *Nat. Commun.* **5**, 4441 (2014).
- [134] M. W. Klein, C. Enkrich, M. Wegener, and S. Linden, "Second-harmonic generation from magnetic metamaterials," *Science* **313**, 502 (2006).
- [135] M. W. Klein, M. Wegener, N. Feth, and S. Linden, "Experiments on second- and third-harmonic generation from magnetic metamaterials," *Opt. Express* **15**, 5238 (2007).
- [136] E. Kim, F. Wang, W. Wu, Z. Yu, and Y. Shen, "Nonlinear optical spectroscopy of photonic metamaterials," *Phys. Rev. B* **78**, 113102 (2008).
- [137] Z. Wang, Y. Luo, L. Peng, J. Huangfu, T. Jiang, D. Wang, H. Chen, and L. Ran, "Second-harmonic generation and spectrum modulation by an active nonlinear metamaterial," *Appl. Phys. Lett.* **94**, 134102 (2009).
- [138] A. Rose, D. Huang, and D. R. Smith, "Controlling the second-harmonic in a phase matched negative-index metamaterial," *Phys. Rev. Lett.* **107**, 063902 (2011).
- [139] M. V. Gorkunov, I. V. Shadrivov, and Y. S. Kivshar, "Enhanced parametric processes in binary metamaterials," *Appl. Phys. Lett.* **88**, 071912 (2006).
- [140] T. Kanazawa, Y. Tamayama, T. Nakanishi, and M. Kitano, "Enhancement of second harmonic generation in a doubly resonant metamaterial," *Appl. Phys. Lett.* **99**, 024101 (2011).
- [141] T. Nakanishi, Y. Tamayama, and M. Kitano, "Efficient second harmonic generation in a metamaterial with two resonant modes coupled through two varactor diodes," *Appl. Phys. Lett.* **100**, 044103 (2012).
- [142] R. W. Boyd, *Nonlinear Optics* (Academic Press, Oxford, UK, 2008).
- [143] K. Fang, Z. Yu, and S. Fan, "Realizing effective magnetic field for photons by controlling the phase of dynamic modulation," *Nat. Photonics* **6**, 782 (2012).
- [144] K. Fang and S. Fan, "Effective magnetic field for photons based on the magneto-optical effect," *Phys. Rev. A* **88**, 043847 (2013).
- [145] K. Fang, Z. Yu, and S. Fan, "Photonic Aharonov-Bohm Effect Based on Dynamic Modulation," *Phys. Rev. Lett.* **108**, 153901 (2012).
- [146] K. Fang, Z. Yu, and S. Fan, "Experimental demonstration of a photonic Aharonov-Bohm effect at radio frequencies," *Phys. Rev. B* **87**, 060301 (2013).

- [147] L. D. Tzuan, K. Fang, P. Nussenzeig, S. Fan, and M. Lipson, "Non-reciprocal phase shift induced by an effective magnetic flux for light," *Nat. Photonics* **8**, 701 (2014).
- [148] E. Li, B. J. Eggleton, K. Fang, and S. Fan, "Photonic Aharonov-Bohm effect in photon-phonon interactions," *Nat. Commun.* **5**, 3225 (2014).
- [149] T. Nakanishi and M. Kitano, "Parametric Amplification in Double-EIT Metamaterial: Application to Storage of Electromagnetic Waves," in *8th Int. Congr. Adv. Electromagn. Mater. Microw. Opt.* (Technical University of Denmark, Copenhagen, Denmark, 2014).

List of publications

Journal papers

- [1] Y. Urade, Y. Nakata, T. Nakanishi, and M. Kitano, “Frequency-Independent Response of Self-Complementary Checkerboard Screens,” *Phys. Rev. Lett.* **114**, 237401 (2015).
- [2] K. Ogawa, S. Tamate, T. Nakanishi, H. Kobayashi, and M. Kitano, “Classical realization of dispersion cancellation by time-reversal method,” *Phys. Rev. A*, **91**, 013846 (2015).
- [3] F. Miyamaru, H. Morita, Y. Nishiyama, T. Nishida, T. Nakanishi, M. Kitano, and M. W. Takeda, “Ultrafast optical control of group delay of narrow-band terahertz waves,” *Sci. Rep.* **4**, 4346 (2014).
- [4] Y. Tamayama, K. Yasui, T. Nakanishi, and M. Kitano, “A linear-to-circular polarization converter with half transmission and half reflection using a single-layered metamaterial,” *Appl. Phys. Lett.* **105**, 021110 (2014).
- [5] Y. Nakata, Y. Urade, T. Nakanishi, and M. Kitano, “Plane-wave scattering by self-complementary metasurfaces in terms of electromagnetic duality and Babinet’s principle,” *Phys. Rev. B*, **88**, 205138 (2013).
- [6] K. Ogawa, S. Tamate, H. Kobayashi, T. Nakanishi, and M. Kitano, “Time-reversed two-photon interferometry for phase superresolution,” *Phys. Rev. A*, **88**, 063813 (2013).
- [7] T. Nakanishi, T. Otani, Y. Tamayama, and M. Kitano, “Storage of electromagnetic waves in a metamaterial that mimics electromagnetically induced transparency,” *Phys. Rev. B*, **87**, 161110 (2013).
- [8] Y. Tamayama, T. Nakanishi, and M. Kitano, “Observation of modulation instability in a nonlinear magnetoinductive waveguide,” *Phys. Rev. B*, **87**, 195123 (2013).
- [9] Y. Nakata, T. Okada, T. Nakanishi, and M. Kitano, “Observation of flat band for terahertz spoof plasmons in a metallic kagomé lattice,” *Phys. Rev. B*, **85**, 205128 (2012).
- [10] F. Miyamaru, S. Kubota, T. Nakanishi, S. Kawashima, N. Sato, M. Kitano, and M. Takeda, “Transmission properties of double-gap asymmetric split ring resonators in terahertz region,” *Appl. Phys. Lett.* **101**, 051112 (2012).
- [11] M. Kitano, Y. Tamayama, and T. Nakanishi, “Coupled-resonator-based metamaterials,” *IEICE Electron. Express*, **9**, 51–64 (2012).
- [12] T. Nakanishi, Y. Tamayama, and M. Kitano, “Efficient second harmonic generation in a metamaterial with two resonant modes coupled through two varactor diodes,” *Appl. Phys. Lett.* **100**, 044103 (2012).

- [13] Y. Nakata, T. Okada, T. Nakanishi, and M. Kitano, “Circuit model for hybridization modes in metamaterials and its analogy to the quantum tight-binding model,” *Phys. Status Solidi*, **249**, 2293–2302 (2012).
- [14] Y. Tamayama, T. Nakanishi, and M. Kitano, “Variable group delay in a metamaterial with field-gradient-induced transparency,” *Phys. Rev. B*, **85**, 073102 (2012).
- [15] H. Kobayashi, Y. Ikeda, S. Tamate, T. Nakanishi, and M. Kitano, “Nonlinear behavior of geometric phases induced by photon pairs,” *Phys. Rev. A*, **83**, 063808 (2011).
- [16] T. Kanazawa, Y. Tamayama, T. Nakanishi, and M. Kitano, “Enhancement of second harmonic generation in a doubly resonant metamaterial,” *Appl. Phys. Lett.* **99**, 024101 (2011).
- [17] H. Kobayashi, S. Tamate, T. Nakanishi, K. Sugiyama, and M. Kitano, “Observation of Geometric Phases in Quantum Erasers,” *J. Phys. Soc. Japan*, **80**, 034401 (2011).
- [18] H. Kobayashi, S. Tamate, T. Nakanishi, K. Sugiyama, and M. Kitano, “Direct observation of geometric phases using a three-pinhole interferometer,” *Phys. Rev. A*, **81**, 012104 (2010).
- [19] Y. Tamayama, T. Nakanishi, Y. Wakasa, T. Kanazawa, K. Sugiyama, and M. Kitano, “Electromagnetic response of a metamaterial with field-gradient-induced transparency,” *Phys. Rev. B*, **82**, 165130 (2010).
- [20] T. Nakanishi, K. Sakemi, H. Kobayashi, K. Sugiyama, and M. Kitano, “Two-Photon Interference of Photon Pairs Created in Photonic Crystal Fibers,” *J. Phys. Soc. Japan*, **78**, 024402 (2009).
- [21] S. Tamate, H. Kobayashi, T. Nakanishi, K. Sugiyama, and M. Kitano, “Geometrical aspects of weak measurements and quantum erasers,” *New J. Phys.* **11**, 093025 (2009).
- [22] T. Nakanishi, H. Kobayashi, K. Sugiyama, and M. Kitano, “Full Quantum Analysis of Two-Photon Absorption Using Two-Photon Wave Function: Comparison of Two-Photon Absorption with One-Photon Absorption,” *J. Phys. Soc. Japan*, **78**, 104401 (2009).
- [23] Y. Tamayama, T. Nakanishi, K. Sugiyama, and M. Kitano, “An invisible medium for circularly polarized electromagnetic waves,” *Opt. Express*, **16**, 20869–20875 (2008).
- [24] Y. Tamayama, T. Nakanishi, K. Sugiyama, and M. Kitano, “Observation of Brewster’s effect for transverse-electric electromagnetic waves in metamaterials: Experiment and theory,” *Phys. Rev. B*, **73**, 193104 (2006).
- [25] T. Nakanishi, K. Sugiyama, and M. Kitano, “Simulation of slow light with electronic circuits,” *Am. J. Phys.* **73**, 323–329 (2005).
- [26] T. Nakanishi, K. Sugiyama, and M. Kitano, “Generation of photon pairs using polarization-dependent two-photon absorption,” *Phys. Rev. A*, **67**, 043809 (2003).
- [27] M. Kitano, T. Nakanishi, and K. Sugiyama, “Negative group delay and superluminal propagation: An electronic circuit approach,” *IEEE J. Sel. Top. Quantum Electron.* **9**, 43–51 (2003).
- [28] T. Nakanishi, K. Sugiyama, and M. Kitano, “Demonstration of negative group delays in a simple electronic circuit,” *Am. J. Phys.* **70**, 1117–1121 (2002).
- [29] T. Nakanishi, K. Yamane, and M. Kitano, “Absorption-free optical control of spin systems: The quantum Zeno effect in optical pumping,” *Phys. Rev. A*, **65**, 013404 (2001).

International conference

- [1] T. Nakanishi, “Storage and manipulation of electromagnetic waves in metamaterials,” *EMN Fall Meet.*, Orland, FL, USA (2014).
- [2] K. Ogawa, S. Tamate, T. Nakanishi, H. Kobayashi, and M. Kitano, “Classical Realization of Dispersion Cancellation by Using Transform-limited Pulses,” *CLEO 2014*, San Jose, California, USA (2014).
- [3] T. Nakanishi and M. Kitano, “Parametric Amplification in Double-EIT Metamaterial: Application to Storage of Electromagnetic Waves,” *8th Int. Congr. Adv. Electromagn. Mater. Microw. Opt.*, Technical University of Denmark, Copenhagen, Denmark (2014).
- [4] T. Nishida, H. Morita, T. Nakanishi, M. Kitano, F. Miyamaru, and M. W. Takeda, “Analyze Of Dependence On Q Factor In Coupled Split-ring Resonator In Terahertz Region,” *8th Int. Congr. Adv. Electromagn. Mater. Microw. Opt.*, Technical University of Denmark, Copenhagen, Denmark (2014).
- [5] K. Sho, Y. Urade, Y. Nakata, T. Nakanishi, and M. Kitano, “Excitation of flat band for spoof surface plasmons in a metallic Lieb lattice by evanescent wave,” *Int. Symp. Front. Terahertz Sci. 2014*, OIST, Okinawa, Japan (2014).
- [6] Y. Urade, Y. Nakata, T. Nakanishi, and M. Kitano, “Self-complementary Metasurface Loaded with ELC-resonators,” *Int. Symp. Front. Terahertz Sci. 2014*, OIST, Okinawa, Japan (2014).
- [7] Y. Urade, Y. Nakata, T. Nakanishi, and M. Kitano, “Experimental Study on Frequency-independent Response of Self-complementary Metasurfaces in Terahertz Regime,” *8th Int. Congr. Adv. Electromagn. Mater. Microw. Opt.*, Technical University of Denmark, Copenhagen, Denmark (2014).
- [8] T. Nakanishi, “Coherent trap of electromagnetic waves in a metamaterial,” *3rd Korea-Japan Metamaterials Forum*, Ewha Womans University, Seoul, Korea (2013).
- [9] T. Nakanishi, T. Otani, Y. Tamayama, and M. Kitano, “Storing and Retrieving Electromagnetic Waves in a Metamaterial by Dynamic Control of Structural Symmetry,” *7th Int. Congr. Adv. Electromagn. Mater. Microw. Opt.*, Bordeaux, France (2013).
- [10] Y. Nakata, Y. Urade, T. Nakanishi, and M. Kitano, “Classification of self-dual metasurfaces,” *3rd Korea-Japan Metamaterials Forum*, Ewha Womans University, Seoul, Korea (2013).
- [11] Y. Urade, Y. Nakata, T. Nakanishi, and M. Kitano, “Photoinduced Structural Transition in a Checkerboard-like Metasurface,” *7th Int. Congr. Adv. Electromagn. Mater. Microw. Opt.*, Bordeaux, France (2013).
- [12] Y. Urade, Y. Nakata, T. Nakanishi, and M. Kitano, “Metamaterial analogue of self-dual electrical circuit,” *3rd Korea-Japan Metamaterials Forum*, Ewha Womans University, Seoul, Korea (2013).

- [13] K. Wada, T. Nakanishi, Y. Tamayama, and M. Kitano, "Enhancement of Four-wave Mixing in a Multi-layered EIT Metamaterial," *7th Int. Congr. Adv. Electromagn. Mater. Microw. Opt.*, Bordeaux, France (2013).
- [14] H. Morita, F. Miyamaru, Y. Nishiyama, T. Nakanishi, M. Kitano, and M. Takeda, "Electromagnetically induced transparency in a terahertz metamaterial," *Int. Symp. Front. THz Technol.*, Nara, Japan (2012).
- [15] T. Nakanishi, Y. Nakata, Y. Tamayama, and M. Kitano, "Progress in coupled-resonator-based metamaterial," *Int. Symp. Front. THz Technol.*, Nara, Japan (2012).
- [16] Y. Nakata, T. Okada, T. Nakanishi, and M. Kitano, "Comprehensive circuit-theoretical method for analyzing hybridization modes in metamaterials," *3rd Int. Conf. Metamaterials, Photonic Cryst. Plasmon.*, Paris, France (2012).
- [17] Y. Nakata, T. Okada, T. Nakanishi, and M. Kitano, "Demonstration of flat band for terahertz coupled plasmon in metamaterials with kagome symmetry," *6th Int. Congr. Adv. Electromagn. Mater. Microwaves Opt.*, St. Petersburg, Russia (2012).
- [18] Y. Nishiyama, F. Miyamaru, H. Morita, T. Nakanishi, M. Kitano, and M. Takeda, "Electromagnetically induced transparency in terahertz metamaterial and reduction of group velocity," *Int. Symp. Front. THz Technol.*, Nara, Japan (2012).
- [19] Y. Tamayama, T. Nakanishi, and M. Kitano, "Variable control of group velocity in a metamaterial with field-gradient-induced transparency," *3rd Int. Conf. Metamaterials, Photonic Cryst. Plasmon.*, Paris, France (2012).
- [20] M. Kitano, Y. Tamayama, K. Chola, and T. Nakanishi, "The chiral vacuum in metamaterials," *1st Korea-Japan Metamaterials Forum*, Ewha Womans University, Seoul, Korea (2011).
- [21] T. Nakanishi and M. Kitano, "Metamaterial Analogue of Electromagnetically Induced Transparency," *GCOE CK Proj. Jt. Int. Symp. At. Fundam. Phys. Its Appl. 2011*, Katsura Hall, Kyoto University, Kyoto, Japan (2011).
- [22] Y. Nakata, T. Okada, T. Nakanishi, and M. Kitano, "A circuit-theoretical method for analyzing coupled modes in metamaterials," *1st Korea-Japan Metamaterials Forum*, Ewha Womans University, Seoul, Korea (2011).
- [23] Y. Tamayama, T. Nakanishi, and M. Kitano, "Slow group velocity in a metamaterial with field-gradient-induced transparency," *1st Korea-Japan Metamaterials Forum*, Ewha Womans University, Seoul, Korea (2011).
- [24] M. Kitano, Y. Tamayama, and T. Nakanishi, "No-reflection No-refraction Metamaterial for Circularly Polarized Light," *Asia-Pacific Radio Sci. Conf. (AP-RASC '10)*, Toyama International Conference Center, Toyama, Japan (2010).
- [25] S. Tamate, H. Kobayashi, T. Nakanishi, K. Sugiyama, and M. Kitano, "Geometric phase in quantum eraser and weak measurement," *10th Int. Conf. Quantum Commun. Meas. Comput.*, University of Queensland, Brisbane, Australia (2010).
- [26] Y. Tamayama, T. Nakanishi, Y. Wakasa, T. Kanazawa, K. Sugiyama, and M. Kitano, "Field-gradient-induced-transparency metamaterial," *4th Int. Congr. Adv. Electromagn. Mater. Microw. Opt.*, Karlsruhe, Germany (2010).
- [27] M. Kitano, Y. Tamayama, and T. Nakanishi, "An Invisible Medium for Circularly Polarized Electromagnetic Waves," *Glob. COE 2nd Int. Symp. Photonics Electron. Sci. Eng.*, Katsura Hall, Kyoto University, Kyoto, Japan (2009).

-
- [28] H. Kobayashi, S. Tamate, T. Nakanishi, K. Sugiyama, and M. Kitano, “Geometrical aspects of weak measurement,” *ONR Work. Entanglement beyond Opt. regime*, Anaheim, USA (2009).
- [29] T. Nakanishi, Y. Wakasa, Y. Tamayama, T. Kanazawa, K. Sugiyama, and M. Kitano, “Electromagnetically-induced-transparency-like metamaterial with magnetic quadrupole resonance,” *third Int. Congr. Adv. Electromagn. Mater. Microw. Opt.*, Queen Mary University of London, UK (2009).
- [30] Y. Tamayama, T. Nakanishi, K. Sugiyama, and M. Kitano, “No-reflection conditions for chiral media,” *third Int. Congr. Adv. Electromagn. Mater. Microw. Opt.*, Queen Mary University of London, UK (2009).
- [31] T. Nakanishi, K. Sakemi, H. Kobayashi, K. Sugiyama, and M. Kitano, “Two-photon interference with photon pairs created in photonic crystal fiber,” *Ninth Int. Conf. Quantum Commun. Meas. Comput.*, University of Calgary, Canada (2008).
- [32] H. Kobayashi, T. Nakanishi, K. Sugiyama, and M. Kitano, “Photon-pair detection using two-photon absorption in photomultiplier tubes,” *Ninth Int. Conf. Quantum Commun. Meas. Comput.*, University of Calgary, Canada (2008).
- [33] H. Kobayashi, T. Nakanishi, K. Sugiyama, and M. Kitano, “Observation of two-photon correlation using nonlinear optical phenomena,” *GCOE Photonics Electron. Sci. Eng. - 1st Young Res. Int. Symp. -*, Katsura Hall, Kyoto University, Kyoto, Japan (2008).
- [34] H. Kobayashi, T. Nakanishi, K. Sugiyama, and M. Kitano, “Development of photon-pair detector using two-photon absorption,” *Int. Symp. Phys. Quantum Technol.*, Nara Prefectural New Public Hall, Nara, Japan (2008).
- [35] T. Nakanishi, K. Sakemi, H. Kobayashi, N. Tung, K. Sugiyama, and M. Kitano, “Measurement of photonic de Broglie wavelength of biphotons created in photonic crystal fiber,” *Int. Symp. Phys. Quantum Technol.*, Nara Prefectural New Public Hall, Nara, Japan (2008).
- [36] T. Nakanishi, “Slow light,” *Japan Soc. Promot. Sci. U.S. Natl. Acad. Sci.*, Arnold and Mabel Beckman Center, Irvine, CA, USA (2006).
- [37] T. Nakanishi, “Detection of photon pairs using two-photon photocurrent in photomultipliers,” *Kochi Summer Sch. - Quantum Inf. Sci.*, Kochi University of Technology, Kochi, Japan (2005).